eman ta zabal zazu

Universidad del País Vasco

Euskal Herriko Unibertsitatea

Development of new high anisotropy phases for permanent magnet applications

BCMATERIALS

BASQUE CENTER FOR MATERIALS, APPLICATIONS & NANOSTRUCTURES

ehugroup

Andrés Martín Cid

-PhD Thesis-

Supervisors:

Prof. José Manuel Barandiarán García

Dr. Daniel Salazar Jaramillo

2018

Resumen

La función esencial de los materiales llamados imanes permanentes (PM) es crear un campo magnético H en un espacio libre de aire. Este campo es proporcional al volumen del imán V_m y la densidad del producto de energía almacenada (B_mH_m), por lo tanto, los imanes con alta $(BH)_{max}$ son altamente deseables. Además del producto energético, la remanencia M_r, relacionada con la magnetización intrínseca del material, y la coercitividad H_c, relacionada con la anisotropía magnética del material, son necesarias para caracterizar un imán permanente, siendo importante también la temperatura de Curie T_C para su uso en entornos industriales. La remanencia M_r determina el campo máximo H dentro del espacio libre de aire, mientras que la coercitividad H_c determina la "dureza" contra la demagnetización por campos magnéticos externos. Los valores altos de H_c requieren una alta anisotropía magnética cuyo origen puede ser magnetocristalino o de forma.

El último informe europeo sobre materias primas críticas (CRM) identificó 20 CRM y los clasificó en relación a su riesgo de provisión e importancia económica para Europa. La mayoría de ellos son tierras raras (RE). Por otra parte, el mercado global de imanes permanentes (PM) tiene una proyección de consumo de $18,800 miles de millones para el año 2018. El riesgo número uno para la industria de los imanes permanentes es su dependencia de elementos de RE y, por tanto, debe reducirse o eliminarse mediante la búsqueda de nuevos materiales. En relación a los PM, el ejemplo más crítico de un mercado que está dominado y restringido por China es el encontrado en los PM más poderosos que hay disponibles; mediante la adición de Dy los clásicos imanes de Nd-Fe-B presentaron alta remanencia y coercividad ($\mu_0 Hc > 2$ T) hasta 200 ºC. Dependiendo de la aplicación los PM utilizan un nivel de dopaje de Dy, que va desde el 4% para aplicaciones en turbinas (PM de 1 tonelada) hasta el 12 % para motores de vehículos eléctricos (PM de 2 kg). Esta demanda hace que se agote rápidamente las RE poniendo en peligro el límite de suministro para las necesidades existentes, en particular el disprosio que subió siete veces su valor entre 2011-2012.

Para todas las aplicaciones basadas en PM el aumento en la densidad de energía magnética del imán ($(BH)_{max}$) incrementa inmediatamente la eficiencia de todo el dispositivo (por ejemplo la relación volumen/potencia

de un motor eléctrico). En otras aplicaciones (como instrumentos de imagen por resonancia magnética (IRM)) el alto $(BH)_{max}$ permite evitar el uso de electroimanes robustos y de alto consumo energético.

Considerando que un PM debe tener alto $(BH)_{max}$ y que el consumo de RE eleva sus costes de producción, se ha iniciado recientemente una campaña internacional para el desarrollo de PM libres/reducidas de RE. En imanes con reducción de RE los esfuerzos se han centrado en nanocompositos *spring magnets* que consisten en una mezcla fina de una fase magnéticamente dura (Sm-Co, Nd-Fe-B) y otra fase blanda o semidura (Fe, Co, Fe_3B) con interacciones acopladas a la fase dura. Sin embargo el único resultado se ha reportado en multicapas epitaxiales pero no en partículas o en polvos los cuales pueden ser usados para hacer PM masivos. En el caso de los PM libres de RE, los trabajos se han enfocado en MnBi pero el mejor (BH)max reportado (65 kJ/m^3) es mucho más bajo que el limite teórico de 130 kJ/m^3.

El objetivo general de esta tesis es la mejora en el rendimiento de fases existentes o de imanes comerciales con una cantidad reducida de RE y el desarrollo de nuevas fases sin RE con las propiedades magnéticas requeridas para ser utilizadas en aplicaciones de PM, como la remanencia, coercividad y densidad de energía magnética del imán ($(BH)_{max}$), además de temperaturas de Curie suficientemente altas para su utilización en entornos industriales. Con este objetivo, los resultados obtenidos se han dividido en tres secciones: i) la reducción del uso de RE, principalmente RE pesadas, en aleaciones basadas en Nd-Fe-B, ii) la búsqueda de nuevas aleaciones que cristalizan en la estructura de tipo ThMn12 (1:12) y iii) la búsqueda de nuevas fases sin RE con anisotropía magnética uniaxial en el sistema de Fe-Co-Ta.

Las aleaciones utilizadas en esta tesis se han producido mediante la técnica de horno de arco para el estudio de las propiedades intrínsecas y una selección de las muestras con las mejores propiedades se han utilizado para desarrollar coercitividad obteniendo cintas microcristalinas o con alto desorden cristalográfico mediante la técnica de *melt-spinning*. Las muestras obtenidas han sido caracterizadas por diversas técnicas para obtener sus propiedades térmicas, cristalográficas, estructurales y magnéticas. Estas técnicas incluyen análisis térmico diferencial (DTA), análisis termogravimétrico (TGA), difracción de rayos X y de neutrones, micros-

copía electrónica de barrido y de transmisión (SEM y STEM), espectroscopia Mössbauer, magnetometría de muestra vibrante (VSM) y dispositivo superconductor de interferencia cuántica (SQUID).

En relación a los estudios sobre la reducción del uso de RE en aleaciones basadas en Nd-Fe-B, estos han sido basados en el uso de elementos dopantes para controlar la microestructura durante la cristalización de aleaciones de Nd-Fe-B con una disminución del contenido de Nd y en el proceso de infiltración de una aleación eutéctica de RE ligera así como su efecto en las aleaciones de Nd-Fe-B microestructuradas con diferentes cantidades de Nd en su composición.

Respecto al proceso de cristalización de las aleaciones de Nd-Fe-B, se muestra como la microestructura de cintas producidas por *melt-spinning* puede controlarse por la velocidad de rotación de la rueda, permitiendo la obtención de cintas muy desordenadas (a velocidades altas) o nanocristalinas (a velocidades bajas), lo que permite una reducción en la temperatura de recocido para obtener las propiedades deseadas. En el proceso de cristalización durante tratamientos térmicos, las aleaciones mostraron la formación de dos fases magnéticas, la fase dura 2:14:1 a temperaturas del orden de 280-400 ºC, y la fase blanda α-Fe alrededor de los 600 ºC. En estas aleaciones se han utilizado dos elementos dopantes para controlar el crecimiento de granos durante los tratamientos térmicos, el Nb y el Cu. El dopaje con Nb muestra un aumento de las temperaturas de cristalización, lo que sugiere la inhibición del crecimiento de granos en presencia de este elemento. Por otro lado, el dopaje con Cu reduce la temperatura a la cual comienza el proceso de cristalización de la fase dura, lo que sugiere la ayuda en el proceso de nucleación en presencia de este elemento. De todas formas, la pronta formación de la fase 2:14:1 con tratamientos térmicos ayuda a la cristalización de la fase secundaria de α-Fe. Se puede concluir que la formación de esta segunda fase también es promovida por el dopaje de elementos y, además, es perjudicial para el acoplamiento de intercambio en los imanes nanoestructurados estudiados.

En relación al proceso de difusión en frontera de grano (GBDP), la infiltración de $Pr_3(Co,Cu)$ en aleaciones de Nd-Fe-B mejora la coercitividad en casi cinco veces de su valor inicial en cintas microestructuradas, alcanzando un valor de 2.5 T, comparable con los mejores valores alcanzados en aleaciones con Dy. Previa infiltración, las cintas estaban compuestas de dos fases, granos nanocristalinos de la fase dura $Nd_2Fe_{14}B$ y

precipitados de la fase blanda α-Fe. El análisis de difracción de rayos X (XRD) y de espectroscopia Mössbauer muestra que la cantidad de α-Fe es ampliamente reducida tras la infiltración. Este hecho, junto con la falta de mejora de coercitividad en la muestra estequiométrica, sugiere un rol importante la presencia de esta fase blanda durante el proceso de infiltración. Pero este efecto no explica el aumento de la coercitividad en la muestra con exceso de Nd, cuya cantidad de α-Fe en un principio era incluso menor.

Una de las muestras infiltradas con reducción de contenido de Nd fue analizada con un microscopio electrónico de transmisión (TEM) de alta resolución para obtener mayor información del efecto de la infiltración en la microestructura de la muestra. Las imágenes obtenidas a partir de rayos X característicos (EDS) muestran una fase intergranular de Pr(Nd)-Fe rica en Pr y un gradiente de composición en los granos, lo que puede describirse como una estructura *core-shell*, con un núcleo de $Nd_2Fe_{14}B$ puro y una capa externa de gradiente de $(Pr,Nd)_2Fe_{14}B$. Estos granos están desacoplados por la fase no magnética de Pr(Nd)-Fe localizada en las fronteras. Esta fase intergranular puede fijar las paredes de dominio ralentizando su movimiento, lo que, junto a los nanogranos de $Nd_2Fe_{14}B$ con pocos defectos, ayuda a incrementar la coercitividad de las muestras.

En la búsqueda de nuevas aleaciones con la estructura 1:12 y propiedades magnéticas útiles para su uso en aplicaciones de imanes permanentes, varias aleaciones han sido estudiadas utilizando Ti y Si como elementos estabilizantes de la estructura.

En la primera aleación se ha estudiado el efecto de la sustitución de Sm por Ce en $Ce_{1-x}Sm_xFe_9Co_2Ti$. El campo de anisotropía de la aleación $CeFe_9Co_2Ti$ es muy bajo para obtener una coercitividad útil, habiendo alcanzado un máximo de μ_0H_c = 0.08 T en las cintas con mejor tratamiento térmico. La sustitución de Ce por Sm mejora el campo de anisotropía magnético de 2.6 T a 8.7 T para la aleación de $SmFe_9Co_2Ti$. Este aumento de la anisotropía muestra un salto entre x = 0.25 y x = 0.5. El análisis de los espectros Mössbauer indica una redistribución del Co en los sitios 8*f* y 8*j* cuando aumenta la concentración de Sm. Esta va de 50/50 en los sitios 8*j* y 8*f* respectivamente a 70/30 para concentraciones de Sm por encima de x = 0.25. Esto coincide con el aumento del campo hiperfino en el sitio 8*j* mientras que este disminuye en el sitio 8*f*. El desplazamiento isomérico también sufre cambios para concentraciones de Sm superiores a x = 0.25. La redistribución de Co podría ser responsable

del comportamiento de la anisotropía. Debido a la mejora del campo de anisotropía con la sustitución de Sm, la coercitividad desarrollada en cintas tras un tratamiento térmico también aumenta, logrando 0.44 T para la aleación de $SmFe_9Co_2Ti$. Este es un valor prometedor para el desarrollo de imanes de grado medio, aunque la formación de α-Fe durante el tratamiento térmico restringe la coercitividad a un valor relativamente muy bajo comparado con su campo de anisotropía.

Como previamente fue teoréticamente predicho, la aleación de $Nd_{0.5}Y_{0.5}Fe_{11}Ti$ muestra un mayor campo de anisotropía (1.75 T) que su homólogo $NdFe_{11}Ti$ (1 T). Los parámetros de la mejor nitrogenación obtenida en este compuesto fueron 420 ºC durante 4 horas. Este proceso resultó en el aumento de los parámetros de red de la estructura cristalina así como de la temperatura de Curie, de 270 ºC hasta 390 ºC, y del campo de anisotropía, del mencionado 1.75 T hasta más de 5 T. Se ha realizado un estudio preliminar en la nitrogenación de cintas de esta aleación. Estas cintas necesitaron un recocido de 4 horas a 1100 ºC para estabilizar la estructura 1:12 y presentaban una coercitividad de 0.055 T. Tras varios intentos de nitrogenación, la mejor muestra fue obtenida tras un proceso de 4 horas a 380 ºC, y presentaba una coercitividad de 0.1 T, pero se incrementó considerablemente la cantidad de α-Fe. Es necesario continuar el estudio de nitrogenación en cintas para lograr encontrar la temperatura y tiempo idóneos para evitar la formación de α-Fe y aumentar más aún la coercitividad.

Se ha realizado un estudio en el efecto de la sustitución de Zr por Ce en $Zr_{1-x}Ce_xFe_{10}Si_2$. Se ha encontrado un aumento de la anisotropía magnética al aumentar la concentración de Ce (de $\mu_0 H_a$ = 2.0 T para x = 0 hasta 2.5 T para x = 0.6) que se correlaciona con el aumento del volumen de la celda cristalina y la distorsión tetragonal (*a/c*) al incrementar el Ce. Sin embargo, no se aprecia ningún cambio en la magnetización. La espectroscopia Mössbauer muestra que el Ce desplaza los átomos de Fe del sitio 8*i* al 8*j* e incrementa el gradiente del campo cristalino en el sitio 8*f*, dejando el campo hiperfino sin variación en todos los sitios del Fe. El llenado completo por Fe de los sitios 8*j*, para x ligeramente por debajo de 0.6, lleva a la inestabilidad de la fase 1:12 al aumentar más aún la concentración de Ce, como en x = 0.6, llevando a la formación de la fase 2:17. El análisis de la expansión térmica muestra una anomalía en el parámetro *c* por debajo de la temperatura de Curie, la cual se puede asignar a una magnetostricción gigante de alrededor de 1500 ppm a temperatura

ambiente en todos los compuestos. La dependencia de esta magnetostricción con M^3 revela un origen puro de ión sinple (o de campo cristalino) tanto de la magnetostricción como de la anisotropía. Estos resultados indican un origen puramente geométrico de la anisotropía magnética.

Finalmente, se presenta la nitrogenación de la aleación de $Zr_{0.4}Nd_{0.6}Fe_{10}Si_2$. Se logró la nitrogenación parcial de una muestra al someterla a un proceso de nitrogenación a 550 ºC durante 18 horas con una presión de nitrógeno de 20 bares. Esta muestra presentaba dos fases muy diferenciadas con la estructura 1:12, una con los mismo parámetros de red que la original y otra con una expansión de la celda. La gran definición de las reflexiones en XRD de ambas fases sugiere que la nitrogenación incompleta se debe a un efecto superficial, como la oxidación, que evita el comienzo de la nitrogenación en parte de los granos, y no una falta de tiempo para completar el proceso. Las propiedades magnéticas de la muestra nitrogenada aumentaron considerablemente, incrementando al temperatura de Curie de 295 ºC hasta 380 ºC y el campo de anisotropía de 2.85 T hasta 5.31 T. La imanación de saturación se mantiene constante con un valor de 131 Am^2kg^{-1}. El comportamiento a alta temperatura de esta muestra, sin mostrar signos de degradación por debajo de 550 ºC, abre una vía al desarrollo de imanes sinterizados basados en la fase 1:12 nitrogenada por medio de procesos alternativos como la técnica de *spark plasma sintering*.

Por último, se muestra el intento por conseguir una aleación sin RE y anisotropía magnética uniaxial en el sistema de Fe-Co-Ta. Este estudio está motivado por los resultados obtenidos por otros participantes del proyecto NOVAMAG, que mostraron la existencia de potenciales fases en el sistema de Fe-Co-Ta por predicciones teóricas y por métodos de *high throughput synthesis* (HTS) como la síntesis combinatorial en película delgada y el crisol reactivo de fusión.

Las aleaciones fueron preparadas por horno de arco y recocidas a 1175 ºC durante 15 horas. La única fase presente en el sistema $(Fe,Co)_{70}Ta_{30,}$ con diferentes ratios de Fe/Co, es la fase de Laves C14. Esta fase es estable a temperatura ambiente pero muestra una magnetización muy baja, de 6 Am^2kg^{-1}, y ninguna anisotropía útil. Reduciendo la cantidad de Ta en las aleaciones, y cerca del compuesto predicho: $Co_{0.25}Fe_{0.5}Ta_{0.25}$, se logra aumentar la temperatura de Curie en casi 100 K y se encuentra un indicio de una tercera fase, a parte de la C14 y el α-Fe(Co), que es ferromagnética a temperatura ambiente y tiene algo de anisotropía. De todas

formas, la baja magnetización que muestran estas muestras las descartan para su uso como imanes permanentes.

Las conclusiones generales obtenidas en esta tesis son las siguientes:

i) Reducción del uso de RE, principalmente RE pesadas, en aleaciones basadas en Nd-Fe-B:

- La microestructura de las cintas de aleaciones de NdFeB puede controlarse mediante la adición de dopantes, teniendo el Nb un efecto de inhibición en el crecimiento de granos, aumentando la temperatura de cristalización, y el Cu promueve la nucleación temprana de granos, reduciendo la temperatura de cristalización.

- La infiltración de una aleación eutéctica de Pr(Co,Cu) produce un aumento de la coercitividad llegando a un valor de 2.5 T, hasta cinco veces el inicial, el cuál es comparable con imanes comerciales que contienen Dy en su composición.

- La fase de α-Fe se reduce considerablemente tras el proceso de infiltración, formándose una estructura *core-shell*, con $Nd_2Fe_{14}B$ en el núcleo y una capa superficial con un gradiente de $(Pr,Nd)_2Fe_{14}B$ con un campo de anisotropía ligeramente superior.

- Estos granos *core-shell* están desacoplados por una fase no magnética de Pr(Nd)-Fe localizada en la frontera de los granos. Esta fase puede tener un efecto de retardo sobre el movimiento de las paredes de dominio. Junto con el alto campo de nucleación de los nanogranos de $Nd_2Fe_{14}B$, los cuales tienen pocos defectos, estos dos mecanismos ayudan a un aumento de la coercitividad de las muestras.

ii) Nuevas aleaciones que cristalizan en la estructura de tipo ThMn12 (1:12):

- La sustitución de Ce por Sm en el sistema $Ce_{1-x}Sm_xFe_{10}Co_2Ti$ mejora el campo de anisotropía, de 2.6 T hasta 8.7 T, y la temperatura de Curie, de 382 ºC hasta 489 ºC, con un salto cuando la concentración de Sm es superior al 25%. El campo hiperfino sufre una evolución similar en el sitio del Fe 8*j*, probablemente debido a la redistribución del Co en la estructura.

- Las cintas de $SmFe_{10}Co_2Ti$ alcanzan una coercitividad de 0.44 T tras un tratamiento térmico óptimo, un valor prometedor para imanes permanentes de grado medio.
- La nitrogenación de aleaciones de $Nd_{0.5}Y_{0.5}Fe_{11}Ti$ aumenta su anisotropía magnética de 1.75 T hasta más de 5 T y la temperatura de Curie de 270 ºC hasta 390 ºC. En el caso de cintas microcristalinas de la misma composición, la coercitividad aumenta de 0.055 T hasta 0.1 T, un valor bajo debido al efecto perjudicial sobre la coercitividad de la gran cantidad de α-Fe en la muestra.
- El campo de anisotropía del sistema $Zr_{1-x}Ce_xFe_{10}Si_2$ aumenta de 2.0 T hasta 2.5 T cuando el Zr es susttuido por Ce. Este aumento se relaciona con el aumento del tamaño de celda y de la distorsión tetragonal (*a/c*) de la red cristalina.
- La espectroscopia Mössbauer muestra un desplazamiento de los átomos de Fe del sitio 8*i* al 8*j*, saturándose este último sitio con x = 0.6, lo que explica la formación de la fase 2:17 para mayores concentraciones de Ce.
- Estas aleaciones muestran una magnetostricción de unos 1500 ppm a temperatura ambiente.
- Se ha logrado nitrogenar por primera vez la aleación $Zr_{0.4}Nd_{0.6}Fe_{10}Si_2$ utilizando una presión de N_2 de 20 bares a una temperatura de 550 ºC durante 18 horas.
- La muestra nitrogenada en un 63% muestra una mejora del campo de anisotropía de 2.8 T hasta 5.3 T, y de la temperatura de Curie de 295 ºC hasta 380 ºC.
- La presencia de dos fases bien diferenciadas, una nitrogenada y otra sin nitrogenar, sugiere que algunos granos no lograron nitrogenarse. Esto puede ser debido a una anomalía superficial en algunos granos, como la oxidación.
- Estas muestras no muestran signos de degradación por debajo de 550 ºC, lo que da pie a un posible desarrollo de imanes sinterizados por técnicas como el *spark plasma sintering*.

iii) Nuevas fases sin RE con anisotropía magnética uniaxial en el sistema de Fe-Co-Ta

– No se ha logrado encontrar nuevas fases con anisotropía uniaxial en el sistema Fe-Co-Ta. La fase de Laves C14 no presenta las propiedades necesarias para su uso en aplicaciones de imanes permanentes.

Content

1 Introduction

1.1 Permanent magnets fundamentals

The magnetic properties of permanent magnets are mainly described by two different concepts; i) those that are related to the intrinsic material and its crystalline structure and ii) the extrinsic properties developed by a specific microstructural modification of the material

1.1.1 Definitions, intrinsic magnetic properties.

Intrinsic magnetic properties refer to those inherent to a specific material that emanates from the atomic origin of magnetism. In this section, three key intrinsic properties of ferromagnetic materials are explained; the magnetic moment, the magnetic anisotropy and the Curie temperature (T_c).

The nearly exclusive responsible of the moment in magnetic solids is the partially filled inner electron shells of transition-metal atoms. The two most important series of elements to produce magnetic materials with a large magnetic moment are the 3d iron-series transition-metals elements Fe, Co and Ni and the rare-earth, or 4f elements, as Nd, Sm and Dy. The magnetic moment *m* of a material is produced by the inner-shell electrons of the magnetic elements and is usually measured in Bohr magnetons per formula unit ($\mu_B = 9.2740 \cdot 10^{-24}$ Am^2). Another widely used way to characterise a material's net moment is the spontaneous magnetisation, defined as the magnetic moment per unit volume or mass of the material and it is measured in Am^{-1} or Am^2kg^{-1}, respectively.

The atomic magnetic moment *m* comes from two different sources; i) the currents associated to the orbital motion of the electrons (orbital moment l) and ii) the electron spin (spin moment s), and for free atoms or ions it is governed by Hund's rules, but in a solid, the ions of the different elements are affected by the electric field of the neighbour ions. For rare-earths, as the 4f shell is much smaller than the atomic radius (0.5 Å against 1.8 Å), the electrons are shielded by the external electron shells as the 5d, and the magnetic moment is well defined by the Hund's rules as shown in Figure 1.1. For the 3d transition-metals (Fe, Co and Ni), as the partially filled shell is more external, it is greatly affected by the crystal field and there is a quenching of the orbital moment, and only the spin

contributes to the magnetic moment as can be seen in Figure 1.1. In addition, when the material is a conductor, the magnetism is itinerant, and it is caused by delocalised electrons. This kind of magnetism is characterised by non-integer moments, for example, the magnetic moments of Fe, Co and Ni at 0 K, which by Hund's rules would be 4 μ_B, 3 μ_B and 2 μ_B; are 2.2 μ_B, 1.7 μ_B and 0.6 μ_B per atom. The reason for these non-integer values is the band-structure character of the itinerant magnetism.

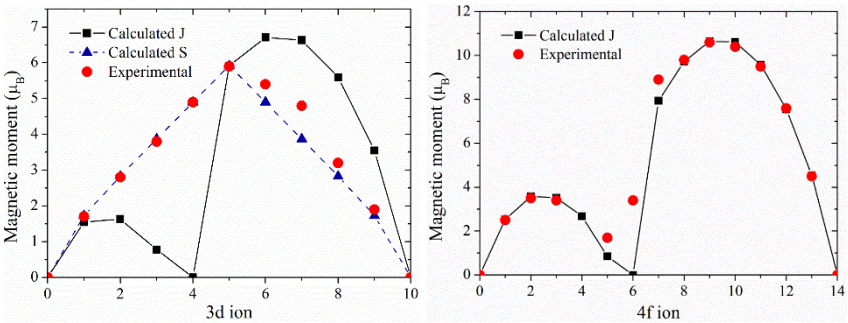

Figure 1.1- Calculated (lines) and experimental (dots) values of the paramagnetic effective moment of the 3d (top) and 4f (bottom) ions. Magnetic moment: $m_{eff} = g\sqrt{J(J+1)}$ *or* $m_{eff} = g\sqrt{S(S+1)}$. Values from J.M.D. Coey, "Magnetism and Magnetic Materials", Cambridge University Press, 2009.

Three magnitudes are derived from the magnetic moments of the atoms: The spontaneous magnetisation (M_s), defined as the magnetisation within each magnetic domain of a ferromagnetic material in the absence of magnetic field and has a dependence on the temperature; the saturation magnetisation (M_0), defined as the maximum magnetisation of a ferromagnetic material, equal to the sum of the magnetic moment of all the atoms present in the material; and the technical saturation magnetisation (M_s), defined as the maximum magnetisation reached applying an external magnetic field, getting the magnetic moments almost completely align but for the thermal agitation effects, so it equals the spontaneous magnetization. Both M_s are used indistinctly as the same quantity.

When the magnetic properties of a material depend on the direction in which they are measured it can be said that magnetic anisotropy exists. This property can be intrinsic to the material (*magnetocrystalline anisotropy*) or induced; like the shape anisotropy.

Magnetocrystalline anisotropy is the tendency of the magnetisation to align itself along a preferred crystallographic direction, called the "easy" axis, since it is easiest to magnetise a demagnetised sample to saturation

if the external field is applied along a preferred direction. The crystal energy is higher when the magnetisation points along the hard direction than along the easy direction, and the energy difference per unit volume between samples magnetised along easy and hard directions is called the magnetocrystalline anisotropy energy.

Phenomenologically, the anisotropy energy, E_{an}, in a material with uniaxial symmetry (i.e. hexagonal and tetragonal) can be described by a series expansion. For instance, for a tetragonal symmetry, the lower order terms are given by [1]:

$$E_{an}(\theta,\varphi) = K_1 \sin^2\theta + K_2 \sin^4\theta + K_3 \sin^4\theta \cos 4\varphi \qquad \textbf{(1.1)}$$

where K_1, K_2 and K_3 are the anisotropy constants and where the direction of the spontaneous magnetisation relative to the single uniaxial (c-axis) direction and the a-axis is given by the polar and azimuthal angles θ and φ respectively. In most cases, it is enough to consider the first two terms. In tetragonal and hexagonal structures, the easy axis will be along the c-axis when K_1 is predominant and positive, while it will be perpendicular to the c-axis when it is negative, and it will point in other directions if it is not the predominant term, being conic when $K_1 < 0$ and $K_2 > |K_1/2|$.

For materials containing rare-earth elements, the anisotropy is mainly driven by the sublattice of these elements. The anisotropy constants K_i have a relation with the crystal-field parameters A_n^m in this rare-earth-based compounds [1]

$$K_1 = -\frac{3}{2}\alpha_J\langle r^2\rangle N_R A_2^0\langle O_2^0\rangle - 5\beta_J\langle r^4\rangle N_R A_4^0\langle O_4^0\rangle \qquad \textbf{(1.2)}$$

$$K_2 = -\frac{35}{8}\beta_J\langle r^4\rangle N_R A_4^0\langle O_4^0\rangle \qquad \textbf{(1.3)}$$

the terms $\langle O_n^m\rangle$ are the thermal averages of the Stevens operators O_n^m (angular momentum operators) [2], α_J and β_J are the Stevens coefficients (which describe the shape of the 4f shell), r is the 4f shell radius and $N_R = (3J_z^2 - J(J+1))$.

At room temperature is possible to consider only the terms up to second-order as the strong temperature dependence makes the higher order terms negligibly low. With this consideration, the value of A_2^0 will define the sign of the K_1 anisotropy parameter, and thus, the type of anisotropy that a material will present.

The Curie temperature (T_c) of a ferromagnetic material is defined as the temperature at which this material loses the ferromagnetic order and begins to behave like a paramagnetic material. This temperature can be derived from the Weiss model of ferromagnetism [3] and is defined as

$$T_C = \frac{g_J \mu_B (J+1) \lambda M_s}{3 k_B} \qquad (1.4)$$

where g_J is the Landé g-value, J the orbital angular moment, k_B the Boltzmann constant, M_s is the saturation magnetisation and λ is a constant which parametrises the strength of the molecular field as a function of the magnetisation (the Weiss constant).

1.1.2 Extrinsic properties

The extrinsic properties of a ferromagnetic material are those resulting from the hysteresis loop and their value can be tuned by changing the microstructure. The two main properties that are explained in this section are the remanent magnetisation, or remanence (M_r) and the coercive field, or coercivity (H_c). Hysteresis loops can be represented in two ways, the M-H loops where the evolution of the volume-averaged magnetisation M with the applied external field H is represented, and the B-H loops, where the magnitude represented is the flux density $B = \mu_0 H + \mu_0 M$.

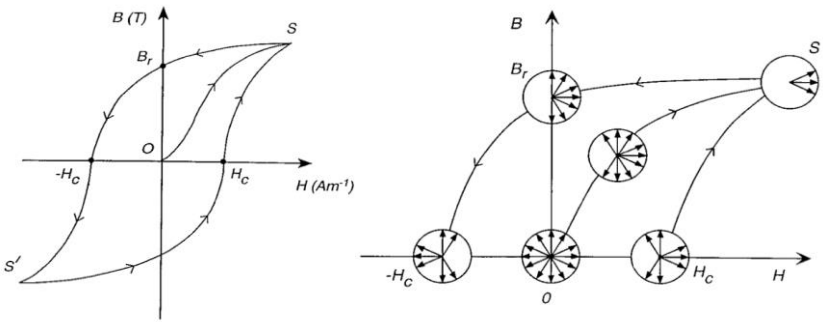

Figure 1.2- Typical hysteresis loop (left) and the magnetic moments orientation along the process of magnetisation (right). [Chikazumi, S. and Charap, S. (1964). Physics of Magnetism, New York: John Wiley and Sons].

The remanence is defined as the magnetisation remaining in a ferromagnetic material when the applied field is removed after a saturation magnetisation state, and will depend on the geometry and the microstructure of the material. For a material with uniaxial anisotropy with an isotropic distribution of easy axes, in the demagnetised the distribution of

domains is isotropic. When an external field is applied, all domains tend to move towards the direction of the field, ending nearly aligned with it at the saturation. Once the field is removed, the domains align with the nearest easy axis of magnetisation, with a net distribution in the direction of the previously applied field. In this way, the remanence of the aforementioned isotropic material can be estimated as

$$M_r = \int_0^{\pi/2} M_s cos\theta sen\theta d\theta = \frac{M_s}{2} \qquad (1.5)$$

A higher remanence can be obtained when the grains constituting the material are single domain and are aligned. Thus, for a perfect alignment, the remanence would have a value equal to the saturation magnetisation.

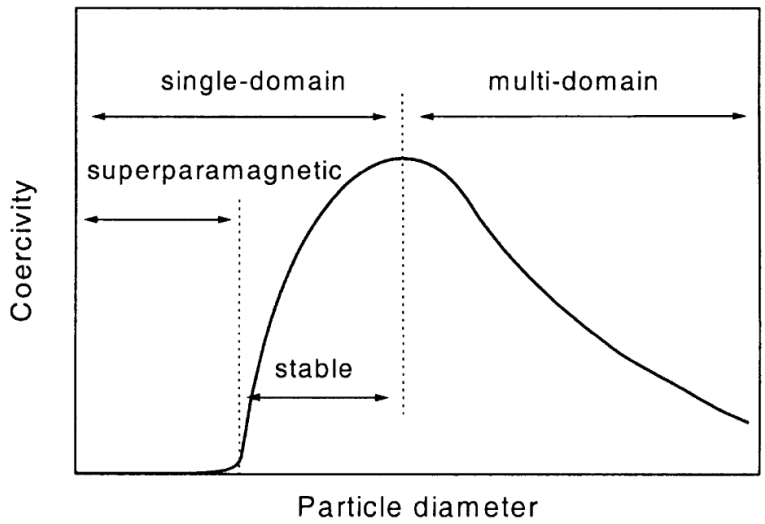

Figure 1.3- Size dependence of the coercivity [G.C. Hadjipanayis, J. Magn. Magn. Mater. 200 (1999) 373–391].

The coercivity is defined as the external magnetic field at which the sum of the magnetic domains of a material that has been previously magnetised is zero. The value of the coercivity is used to classify materials in hard magnetic materials (permanent magnets), semi-hard materials (storage media) and soft magnetic materials (flux multipliers) [4]. This property of ferromagnetic materials is significantly dependent on the imperfections of the material, as the metallurgical inhomogeneity, grain boundaries and surface irregularities, as well as the size of the crystalline grains. The coercivity is defined by two types of mechanisms; nucleation and pinning.

When a region of a single crystal presents a less perfect magnetic-moment arrangement or a higher demagnetisation factor (as in sharp edges of a crystallite), a Bloch wall can be nucleated in such a point. This Bloch wall can freely spread across all the crystal until it fully reverses its magnetisation. As the motion of the walls within the grains is relatively easy, in order to get higher coercivities the wall motion has to be obstructed by grain boundaries. Materials which coercivity is nucleation-driven present two properties measurable from the demagnetised state; a very large low-field susceptibility, and a magnetic saturation state reached in relatively low fields.

The presence of inhomogeneities in the grains can act as pinning sites for the propagation of the domain walls, and thus, prevent further magnetisation reversal. In this case, the coercivity is determined by the pinning field strength. A homogeneous distribution of this pinning sites produces very weak low-field susceptibility, requiring a high field applied in order to reach the saturation magnetisation state. This process of magnetisation is irreversible and dominates over other reversible processes as the nucleation and movement of domain

The coercivity is also grain size dependent. The coercivity of powdered hard magnetic phases increases with the reduction of particle size up to a maximum, at the single domain size limit, followed by a decrease due to thermal effects for lower sizes, ultimately reaching zero at the superparamagnetic particle size as shown in Figure 1.3 [5]

1.1.3 What makes a good permanent magnet? $(BH)_{max}$, the key figure of merit

A permanent magnet is a ferromagnetic material with a coercivity big enough to overcome the demagnetizing fields produced inside the material when this is magnetised, once the externally applied field is removed. Some ferromagnetic materials, as some steels and AlNiCo alloys, need to have a shape (as the classical horseshoe-type magnets) that minimise the internal demagnetisation fields to maintain their remanent magnetisation, while others, as rare earth-based magnets, can have any shape due to their very high coercivity.

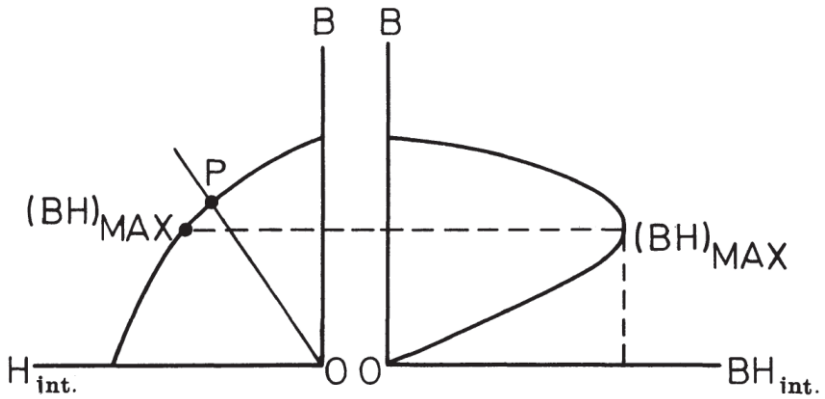

Figure 1.4- The demagnetisation and B versus BH curves for a magnet [G.J. Long and F. Grandjean, Supermagnets, Hard Magnetic Materials].

The usability of a magnet is defined by its capacity to provide a magnetic field in a particular volume of space, as in the air gap of volume V_g that is shown in Figure 1.5. The area of the B-H hysteresis loop is proportional to the amount of energy stored in the magnet, and the BH product at any point of the demagnetisation curve is called the energy product of the magnet. This energy product changes with B over the demagnetisation curve, going through a maximum value, $(BH)_{max}$, as it is shown in Figure 1.4.

Taking as a reference the toroidal magnet of Figure 1.5, the application of Ampere's law along the closed magnetic induction lines gives,

$$H_g V_g = H_m V_m \qquad (1.6)$$

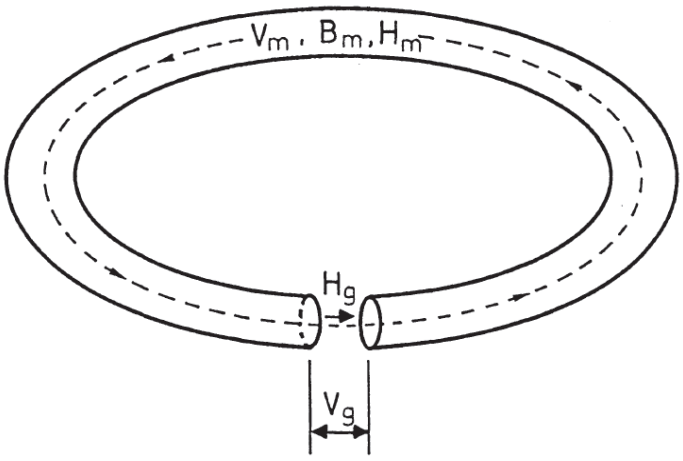

Figure 1.5- An open magnetic circuit [G.J. Long and F. Grandjean, Supermagnets, Hard Magnetic Materials].

If Gauss' law is applied to the same magnetic induction line,

$$\mu_0 H_g = B_m \qquad (1.7)$$

If both equations are combined

$$\mu_0 H_g^2 V_g = (B_m H_m) V_m \qquad (1.8)$$

where H_g is the magnetic field strength in the air gap of the magnet, B_m and H_m are the magnetic induction and the magnetic field strength in the magnet, and V_m is the volume of the magnet. Thus, for a given magnetic field in the working air gap, the volume of the magnet needed is inversely proportional to the $B_m H_m$ product, which is the previously defined energy product.

Due to this property of the energy product, $(BH)_{max}$ has become a figure of merit of great importance for the permanent magnet industry, as it is directly related to the amount of material that is needed for a specific application. A comparison of the size and shape needed for different materials to generate a 1000 G field at 5 mm from the pole surface is illustrated in Figure 1.6.

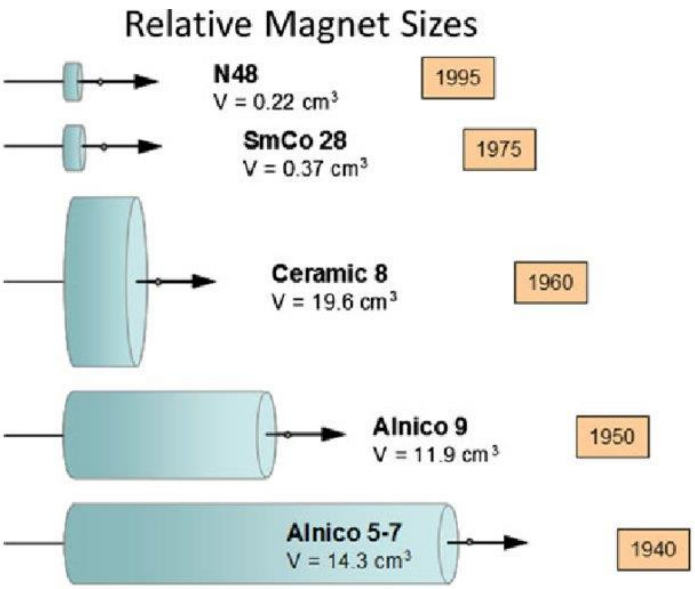

Figure 1.6- Relative magnet size and shape of various permanent magnet materials to generate 1000 G at 5 mm from the pole face of the magnet [L.H. Lewis and F. Jiménez-Villacorta, Metall. Mater. Trans.A, (2013), Vol. 44, Supp. 1].

Over the last century, the maximum energy product has increased by a factor of 100 as is shown in Figure 1.7. There are two improvement steps that are worth mentioning. The first step was at the 60s with the development of the first rare earth permanent magnet based on SmCo and later with the SmTM magnets, reaching maximum energy product up to 255 kJ/m^3 (≈32 MGOe). The second big step happened in the 80s with the development of the NdFeB magnets, reaching maximum energy product close to 477 kJ/m^3 (≈60 MGOe) with the addition of some Dysprosium.

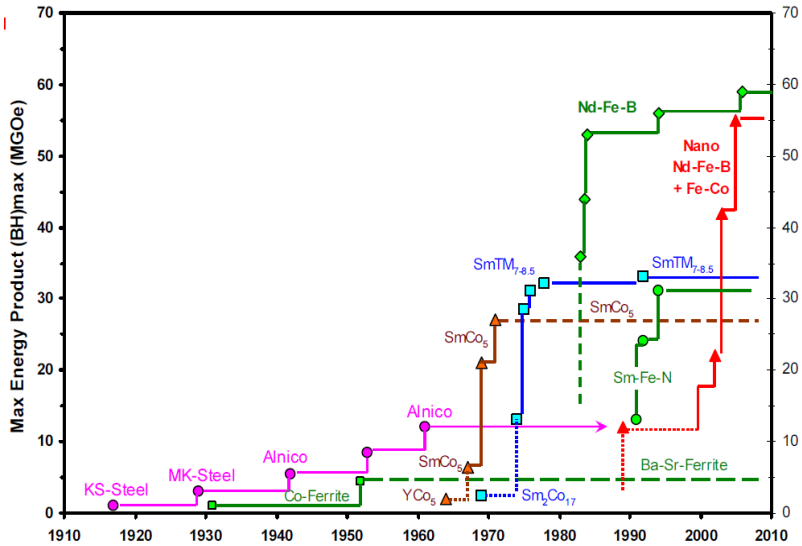

Figure 1.7- Development of the maximum energy product over the last century [A. Yan, "R&D Trends of Rare Earth Permanent Magnets", 2013].

1.2 Motivation

1.2.1 Permanent magnets market: Nowadays and a future perspective

The global permanent magnet market size was estimated at USD 19.35 billion in 2016, and the compound annual growth rate for the 2018-2024 period is of a 9% [6], with a forecast size of USD 30.4 billion by 2024 [7]. This huge market is dominated by NdFeB magnets, whose production has been steadily increasing since 1996 from 6000 tons to about 63000 tons by 2008 and has around the 63% share of the sales market (Figure 1.8) [8].

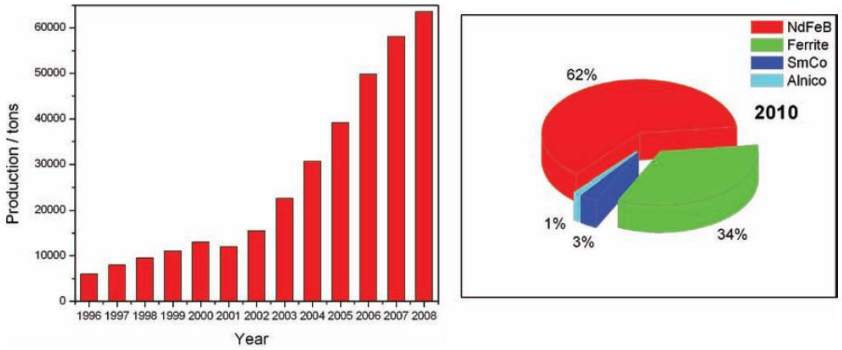

Figure 1.8- Output of NdFeB permanent magnets during the past ten years (left) and predicted percentage sales (USD) for 2010 of the major permanent magnets in the world (right).[O. Gutfleich et al., Adv. Mater. 2011, 23, 821–842]

Permanent magnets applications are widely spread across several areas as medical applications, e.g. surgical drills, saws and other medical tools and in a higher amount on magnetic resonance imaging systems (MRI); consumer appliances, e.g. air conditioning, refrigerators, hard disk drives (HDD) and acoustic transducers; and electric motors and generators. These last two are of great importance due to the environmental importance of wind power generation and electrical vehicles.

Between the years 2000 and 2011, the wind power industry experienced a growth rate of 27% per year, doubling the wind power capacity every three years on average. By the end of 2011, the total (in and offshore) wind power capacity installed worldwide reached 238 GW, by 2013 it reached 318 GW and it is estimated to reach 700 GW by 2020. On a global basis, a 15% of the power installed is produced with permanent magnet type generators, a value that is estimated to grow up to 20% by 2020. Each of these permanent magnet type generators uses around 500 kg of permanent magnets per MW summing up to 8000 tons of permanent magnets in 2015 destined to wind power generation and predicted to grow over 11000 tons by 2020 [9–11]

Regarding the electrical vehicles (EVs), after reaching the mark of 1 million electric cars in 2015, in 2016, after a sales record of 750 thousand worldwide, the threshold of 2 million electric cars has been surpassed [12]. The EVs market is expected to grow in the forthcoming years thanks to the governments initiatives to substitute internal combustion vehicles by EVs, e.g. by 2025 Norway wants to have 100% of its new car sales to be battery EVs while California, France, and the United King-

dom have proclaimed that they will end sales of internal combustion vehicles by 2040 [13]. This increment of the EVs demand will be corresponded with the consequent increase of the car manufacturers' offer, with a similar compromise to increase the EVs sales share, e.g. 15-25% of BMW group sales by 2025, 13 new EV models by 2020 from Ford and 2-3 million annual electric car sales by 2025 from Volkswagen. Unlike wind power generators, the predominant traction motor used in EVs makes use of permanent magnets [14] against the counterpart induction motors. Recently, one of the most known electric cars manufacturer, Tesla Motors, decided to change the motor for their accessible model, the Tesla Model 3, and use a permanent magnet based motor instead of an AC induction motor as in their previous models. This change was "because for the specification of the performance and efficiency, the permanent magnet machine better solved their cost minimisation function, and it was optimal for the range and performance target of the car" [15].

1.2.2 Dominance of rare earth-based permanent magnets and its criticality

As it has been shown previously, rare earth permanent magnets (REPMs) dominates the PM market due to their better properties compared with Alnico and ferrite based magnets. The rapidly growing behaviour of the PM market has arisen concerns about the availability of the raw materials needed for the production of REPMs.

While the reserves of rare earths (REs) are distributed around the world, with China having around 50% [16], the production of REs is dominated

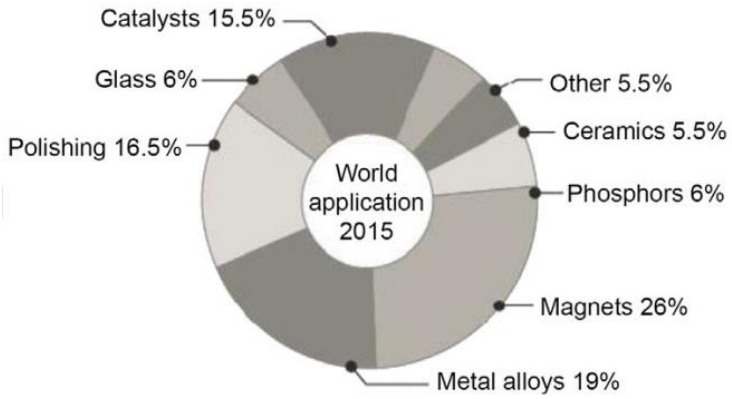

Figure 1.9- 2015 REE demand estimate by application in the world [Z. Weng, Wind Energy Engineering, Chapter 24].

by this country, with over 75% [17]. This production dominance by one country and the increasing use of REs has led to an unstable market, in 2011, rare earth metal prices increased by a factor of 15-25, followed by a later reduction of the price staying at a relative value of between 2-17 times the price of 2001 [18].

Due to the behaviour of the RE market and the importance of these elements, the government of the U.S. as well as the European Union have classified the REs, especially heavy rare earths, as critical raw materials [19,20], and are encouraging research based on the reduction or elimination of these elements in the different applications in which they are used (Figure 1.9).

This thesis has been developed in the framework of the European project named NOVel, critical materials free, high Anisotropy phases for permanent MAGnets, by design (NOVAMAG). This project is coordinated by the Basque Center for Materials, Applications & Nanostructures (BCMaterials), and involves 14 other partners around the world: the Uppsala University in Sweden; the Danube University Krems in Austria; the International Research Center in Critical Raw Materials for Advanced Industrial Technologies (ICCRAM) of the University of Burgos in Spain; the Tohoku University in Japan; the Technische Universität Darmstadt, the Fraunhofer project Group IWKS and Vacuumschmelze GmbH & Co KG in Germany; the University of Delaware in the USA; the National Center of Scientific Research "Demokritos" in Greece; Technion in Israel; Cea-leti and ARELEC Magnets and Magnetic Systems in France, and MBN nanomateralia and the Fiat research centre in Italy.

The objective of this project is to develop an automated large computational screening followed by an experimental screening of new and novel intermetallic compounds with uniaxial structures (with high saturation magnetisation, magnetocrystalline anisotropy and Curie temperature), which can be used for the rapid development of high-performance permanent magnets without the use of critical raw materials.

1.3 Objectives and structure of the thesis

The general objective of this thesis is the improvement of the performance on existing phases or commercial magnets with reduced RE content and the development of new RE-free phases with the magnetic properties required for permanent magnet applications.

This thesis is structured in 6 chapters. After this introduction (chapter 1), Chapter 2 will be focused on the fabrication and characterisation techniques that have been used during the work.

The next three chapters will move towards the reduction of the rare earth used in the candidate alloys for permanent magnets, from the removal of heavy rare earths, passing through a reduction of the overall use of rare earths to the attempt of complete removal of rare earths.

Chapter 3 will be focused on the reduction of heavy rare earths in the common Nd-Fe-B alloys with an enhanced coercivity. With this purpose, two different procedures will be shown; the control of the crystal growth on melt-spun ribbons a well as the nanostructure with the addition of dopants, and the enhancement of the coercivity by means of a grain boundary diffusion process of a eutectic alloy. These two processes are done in Nd-lean alloys.

Chapter 4 will focus on the alloys with the ThMn12-type structure. This kind of alloys have been known since the 1980s but recently the had an increased interest due to their promising magnetic properties with a reduced amount of rare earths (7.7%) compared with typical Nd-Fe-B magnets (11.8%). The properties reported for this kind of compounds makes them capable of filling the gap on performance between high-performance REPMs and the low-performance Alnico and ferrites. Here are studied two series of alloys, one of them is stabilised in the ThMn12-type structure by substitution of Fe by Ti, while in the other Si is used as stabilising element. As a procedure to develop coercivity in the alloys, amorphous melt-spun ribbons were heat treated to tune the microstructure. In some of the alloys, a nitrogenation process was done to improve the intrinsic magnetic properties.

Chapter 5 will focus on the screening of the Fe-Co-Ta system looking for a new structure with uniaxial anisotropy. This screening is based in theoretical calculations performed in collaboration by several groups of the NOVAMAG project.

Finally, in Chapter 6, the conclusions resulted from this work will be presented and open perspectives will be pointed out.

1.4 References

[1] K.H.J. Buschow, F.R. de Boer, Physics of Magnetism and Magnetic Materials, Springer US, 2003. doi:10.1007/b100503.

[2] K.W.H. Stevens, Matrix Elements and Operator Equivalents Connected with the Magnetic Properties of Rare Earth Ions, Proc. Phys. Soc. Sect. A. 65 (1952) 209–215. doi:10.1088/0370-1298/65/3/308.

[3] S. Blundell, Magnetism in condensed matter, Oxford University Press, 2001.

[4] Y. Liu, D.J. Sellmyer, Daisuke Shindo, Handbook of advanced magnetic materials, 2008. doi:10.1007/b115335.

[5] G.C. Hadjipanayis, Nanophase hard magnets, J. Magn. Magn. Mater. 200 (1999) 373–391. doi:10.1016/S0304-8853(99)00430-8.

[6] Global Permanent Magnet Market Share | Industry Report, 2018-2024, (n.d.). https://www.grandviewresearch.com/industry-analysis/permanent-magnets-industry (accessed October 2, 2018).

[7] W. Benecki, More Than You Ever Wanted to Know About the Permanent Magnet Industry!, n.d. https://www.waltbenecki.com/uploads/more_than_you_ever_wanted_to_know.pdf (accessed October 2, 2018).

[8] O. Gutfleisch, M.A. Willard, E. Brück, C.H. Chen, S.G. Sankar, J.P. Liu, Magnetic materials and devices for the 21st century: Stronger, lighter, and more energy efficient, Adv. Mater. 23 (2011) 821–842. doi:10.1002/adma.201002180.

[9] S. Constantinides, Electricity, Magnetism and… Survival, 2015. http://www.arnoldmagnetics.com/wp-content/uploads/2017/10/Energy_-Magnetism-and-Survival-Constantinides-APS-GERA-2015-psn-lo-res.pdf (accessed October 2, 2018).

[10] IRENA, Renewable Energy Technologies: Cost Analysis Series Volume 1: Power Sector, 2012.

https://www.irena.org/DocumentDownloads/Publications/RE_Technologies_Cost_Analysis-WIND_POWER.pdf (accessed October 2, 2018).

[11] S. Constantinides, Market Outlook for Ferrite, Rare Earth and other Permanent Magnets, 2016. http://www.arnoldmagnetics.com/wp-content/uploads/2017/10/Magnetics-2016-Market-Outlook-Constantinides-160119-opt8.pdf (accessed October 2, 2018).

[12] I. - International Energy Agency, Global EV Outlook 2017 Two million and counting, n.d. www.iea.org/t&c/ (accessed October 3, 2018).

[13] The global electric-vehicle market is amped up and on the rise | McKinsey, (n.d.). https://www.mckinsey.com/industries/automotive-and-assembly/our-insights/the-global-electric-vehicle-market-is-amped-up-and-on-the-rise (accessed October 3, 2018).

[14] T. Huynh, M.-F. Hsieh, Performance Analysis of Permanent Magnet Motors for Electric Vehicles (EV) Traction Considering Driving Cycles, Energies. 11 (2018) 1385. doi:10.3390/en11061385.

[15] Tesla motor designer explains Model 3's transition to permanent magnet motor - Electrek, (n.d.). https://electrek.co/2018/02/27/tesla-model-3-motor-designer-permanent-magnet-motor/ (accessed October 3, 2018).

[16] Top Rare Earth Mining Reserves by Country | Investing News Network, (n.d.). https://investingnews.com/daily/resource-investing/critical-metals-investing/rare-earth-investing/rare-earth-reserves-country/ (accessed October 3, 2018).

[17] Rare Earths Production: 8 Top Countries | Investing News Network, (n.d.). https://investingnews.com/daily/resource-investing/critical-metals-investing/rare-earth-investing/rare-earth-producing-countries/ (accessed October 3, 2018).

[18] S. Constantinides, Balancing Material Supply Demand within the Magnet Industry, 2015. http://www.arnoldmagnetics.com/wp-

content/uploads/2017/10/Balancing-Material-Supply-and-Demand-within-the-Magnet-Industry-Constantinides-Magnetics-2015-psn-lo-res.pdf (accessed October 3, 2018).

[19] S. Constantinides, The Important Role of Dysprosium in Modern Permanent Magnets, Arnold Magn. Technol. (2012) 1–8. http://www.arnoldmagnetics.com/wp-content/uploads/2017/10/Important-Role-of-Dysprosium-in-Modern-Permanent-Magnets-150906.pdf (accessed October 3, 2018).

[20] Report on Critical Raw Materials for the EU Report of the Ad hoc Working Group on defining critical raw materials, 2014. http://www.catalysiscluster.eu/wp/wp-content/uploads/2015/05/2014_Critical-raw-materials-for-the-EU-2014.pdf (accessed October 3, 2018).

2 Experimental techniques

In this section we describe the methodology used to produce the alloys (synthesis), to improve their magnetic properties and to develop coercivity (processing) and to characterize their magnetic and structural properties in the different steps of the production.

2.1 Sample preparation

Figure 2.1 shows a flowchart of the different paths followed to prepare samples in this thesis. With any new alloy, the first step is to measure its intrinsic properties and check if it is good enough to try to develop coercivity. In the case of 1:12 alloys with RE different from Sm, a nitrogenation process must be made in order to improve their intrinsic properties.

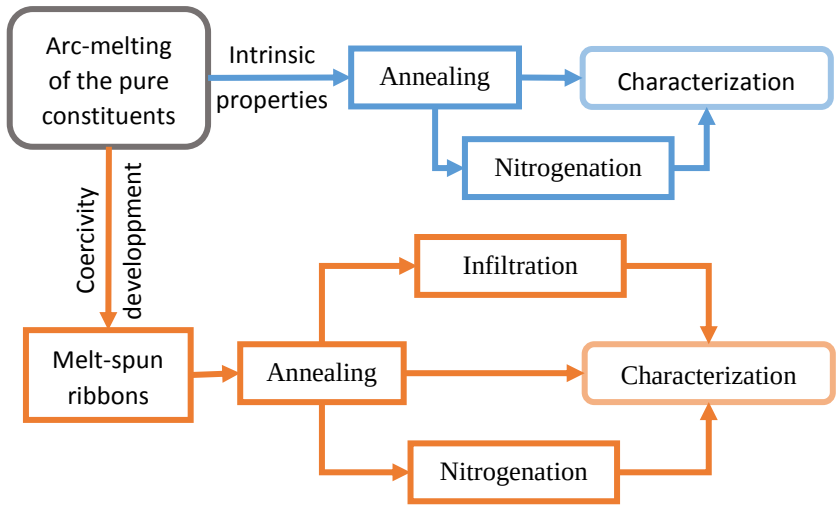

Figure 2.1- Flowchart of the sample preparation paths followed.

Selected alloys, with good intrinsic properties, are used to develop coercivity by a bottom-up approach. To optimise coercivity, highly disordered ribbons are produced by the melt-spinning technique and subsequently annealed to obtain a microstructure with crystallite sizes in the order of 50-200 nm, i.e. in the range of single domain size. In the case of 2:14:1 alloys, an infiltration process is made to further improve the coercivity. In non-Sm 1:12 alloys, nitrogenation of microcrystalline powder is used again.

2.1.1 Arc furnace melting

Three different arc furnaces have been used during this work; two homemade at the NCSR Demokritos and at the University of Delaware, and a MAM-1 (Johanna Otto GmbH) at the University of Cantabria.

Arc furnaces operate by applying a high DC-voltage between the electrode and the crucible, being able reach temperature as high as 3500K. With this technique, polycrystalline ingots of up to 10g can be produced.

Starting pure constituents (99.7-99.99%) are melted in the proportions of the alloy wanted. As Sm boiling point and vapour pressure are low compared with the other constituents, a charge of 120 weight-% of the nominally required amount of this element is usually employed to compensate the mass loss during the melting and posterior treatments.

Due to the inhomogeneous cooling rate of the ingot, spurious phases and composition gradients can appear after the melting process and a consequent annealing is required to overcome this issue and obtain homogenous single-phase alloys.

2.1.2 Melt-spinning

The production of ribbons was performed in the homemade melt-spinner at the University of Delaware and a scheme of it is shown in Figure 2.2. For this technique, the as-cast alloy obtained by arc-melting is located into a quartz crucible previously handmade prepared with an ejection orifice of the wanted diameter, around 0.3-0.6 mm. This crucible is placed in the cavity of the induction coil that is used to melt the alloy. All above described is under controlled atmosphere inside the chamber of the melt

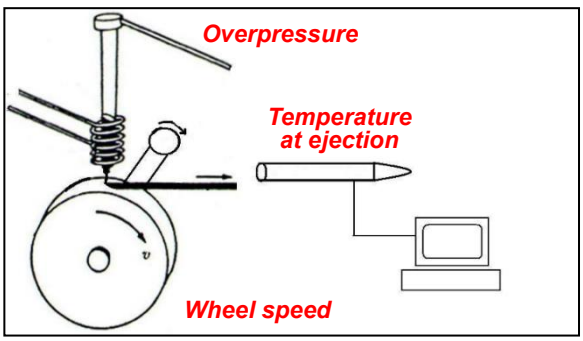

Figure 2.2- Schematic representation of a melt-spinner with the controlled parameters.

spinner. The chamber is purged three times and filled with Ar gas once the sample has been located inside of it.

After setting the desired linear wheel speed on the system, an overpressure of Ar, previously set up, is applied to the top of the molten sample to eject it. To avoid problems of the sample getting stuck in the crucible, the molten state is checked either by measuring the temperature with a pyrometer or by visual confirmation, i.e. when the characteristic molten meniscus is formed. As the heating method used in this system is an induction furnace, it is important to use big chunks of the sample to get an optimal heating. With this kind of system, cooling rates in the order of 10^4-10^7 K/s can be reached, allowing the production of amorphous/highly disordered ribbons.

2.2 Characterization techniques

2.2.1 Differential thermal analysis (DTA)

DTA is a thermo-analytic technique in which identical thermal cycles are applied to the material under study and an inert reference, while recording any temperature difference between sample and reference. Exothermic and endothermic processes can be detected. The enthalpy change of these processes can be obtained with the area under the DTA peak, and it is not affected by the lattice contributions on the heat capacity. Therefore DTA provides information on the transformations that have occurred on the sample during heating/cooling such as glass transitions, crystallization, melting and sublimation. In our case we can identify the crystallization of the desired phases as well as other processes like phase separation, helping to select a range of temperatures to anneal melt spun ribbons in order to crystallize them in the desire phase and other heat treatments. The instrument used is a SETARAM 92-16.18 located at BCMaterials. The experiments were done under Ar atmosphere with a heating rate of 10K/min and using alumina crucibles.

2.2.2 Thermogravimetric analysis (TGA)

TGA is a technique in which the mass of a sample is measured as a function of time while it is subjected to a defined temperature profile and in a controlled atmosphere. Under the influence of an external magnetic field, by a magnet located outside the TGA furnace, the microbalance of the system can measure the effect of the magnetic force experimented in

the sample, and its influence on the thermogravimetric balance. By this way, if the mass of the system is tared at room temperature, the loss of magnetisation with temperature will be seen as a gain on the mass detected by the TGA instrument, having a huge change at the Curie temperature of the sample that can be easily seen in the derivative of the mass curve. As the displacement of the microbalance arm is very small, the applied magnetic field on the sample can be considered continuous over all the measurement.

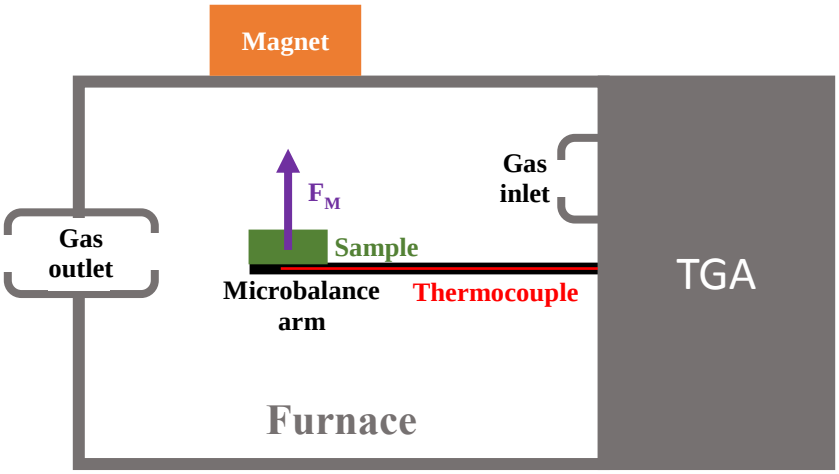

Figure 2.3- Schematic representation of the assembly to measure the Curie temperature.

2.2.3 Diffraction techniques for the crystal and magnetic structure

X-ray and Neutron Diffraction (XRD and ND respectively) are two very common techniques used to characterise the structure of a material. These techniques are based on the diffraction produced when a X-ray or neutron beam is scattered by a material following the Bragg's law:

$$2dsin\theta = n\lambda \qquad (2.1)$$

where d is the distance between the crystallographic planes, n is the interference order, λ is the incident wavelength and θ is the angle between the incident beam and the scattering planes. The main difference between XRD and ND is the interaction between the incident beam and the material.

In XRD, the beam is scattered due to the interaction with the electrons of the atoms, and thus, the intensity of the scattered beam is proportional to

the number of electrons, Z, within the electronic cloud. A consequence of this dependence is the difficulty to evaluate the structure of materials with atoms of similar Z (as Fe and Co) or with small values of Z (as N). The intensity of the reflections is variable and depends on the form factor f(θ) which decreases with the angle θ (Figure 2.4).

For ND, as neutrons do not have any electrical charge, they can penetrate further into the sample and only scatters with the nucleus of the atoms. The diffraction of the neutrons can be due to two interactions, the nuclear and the magnetic interaction, the latter as a consequence of the magnetic moment of neutrons.

The interaction of neutrons with the nucleus of atoms is characterised by the diffusion amplitude or Fermi length, b, which is independent of the scattering angle θ (Figure 2.4), and thus it present constant peak intensity for all the scattering angles. Another difference with XRD is the dependence of the cross section with Z. As neutrons do not interacts with electrons, the cross section is dependent on the nucleus characteristics. In this way, with ND it may be easier to differentiate between atoms with similar Z and with low Z, as well as between isotopes of the same element, for example ^{1}H and ^{2}H [1–3].

As a consequence of the electronic origin of the magnetic interactions of neutrons with atoms, the variation of the magnetic form factor with the angle, $f_{mag}(\theta)$, is similar to the XRD f(θ), with a more pronounced reduction (Figure 2.4). The consequence of this behaviour of the magnetic form factor is the appearance of magnetic reflections only at very low angles.

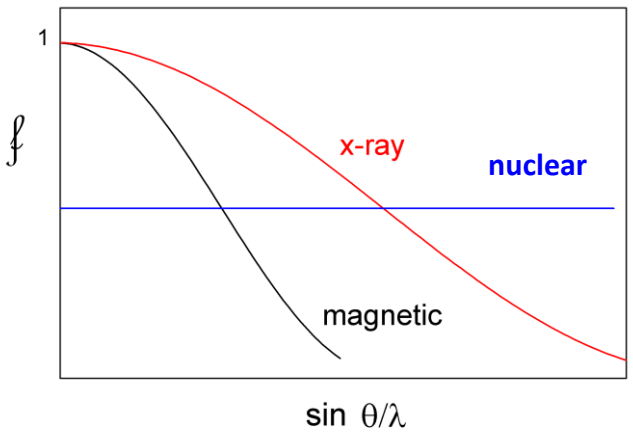

Figure 2.4- Magnetic, nuclear and X-ray form factors evolution with θ.

In this work, three X-ray diffractometers have been used; Philips X'Pert Pro diffractometer, at the Advanced Research Facilities (SGIker) of the University of the Basque Country, a Rigaku Ultima IV diffractometer at the University of Delaware, and a SIEMENS D500 diffractometer at the NCSR "Demokritos", all of them in the Bragg-Brentano geometry, with Cu-Kα radiation (λ = 1.5418 Å).

The D20 high-intensity two-axis diffractometer with variable resolution at the Institut Laue-Langevin was used with a wavelength of λ = 2.41 Å.

Diffraction data obtained in this work was fitted by a least square method using the FullProf suit software [4]

2.2.4 Electron microscopy

In optical microscopy the real limit of resolution is about of 200 nm because of the wavelength of the visible light.

Electrons can reach wavelengths of 4 pm at an energy of 100 keV. Improving the electromagnetic lenses used to guide the beam of electrons, electronic microscopes are nowadays able to detect single atoms with a spatial resolution of 0.05 nm [5].

2.2.4.1 Scanning electron microscopy (SEM)

The SEM scans the surface of the sample with a focused beam of electrons to generate an image. It is a powerful instrument to analyse the morphology, topology and composition of a wide range of samples. It is possible also to make a quantitative analysis of the chemical composition in a point of the surface of the samples by analysing the X-rays emitted by the atoms excited by the impinging electrons (Energy-dispersive X-ray spectroscopy or EDS technique).

In a typical SEM instrument, represented in Figure 2.5, an electron beam is accelerated and focused by a series of electromagnetic lenses. The position of the beam over the surface of the sample is controlled by scanning coils.

When the electron beam interacts with the sample, three different outgoing radiation signals are produced, as seen in Figure 2.6, and detected by different sensors; characteristic X-rays (used in EDS as mentioned on the first paragraph of this section), backscattered electrons (BSE) and secondary electrons (SE). BSE are high energy electrons result of the elastic backscatter of the electrons by atoms of the sample. As the backscattering is proportional to the atomic number, the number of BSE detected on regions with atoms of high Z is greater, helping on the differentiation of phases. SE, on the other hand, are low energy electrons produced when electrons are ejected from the K-orbitals of the sample atoms. Thanks to the wide depth of field that can be achieved while measuring SE, the image obtained have a characteristic three-dimensional appearance useful to understand the surface structure of the sample.
The interaction volume, i.e. the region of interaction between the sample

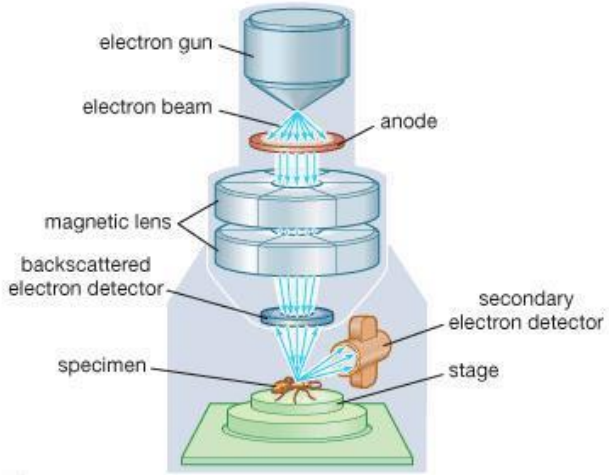

Figure 2.5- Basic arrangement of a scanning electron microscope.

and the electron beam, depends on the applied accelerating voltage and the atomic composition of the sample. Due to the low-energy characteristic of SE, only those produced very near to the surface can be detected, with a depth below 50 nm. In the case of BSE and characteristic X-rays, the interaction depth can reach 1-5 μm [6].
In this work, three commercial SEMs with EDX have been used; a JEOL JSM-6335F at the University of Delaware, a Phenom ProX at the NCSR Demokritos and a Hitachi TM3000 at the University of the Basque Country.

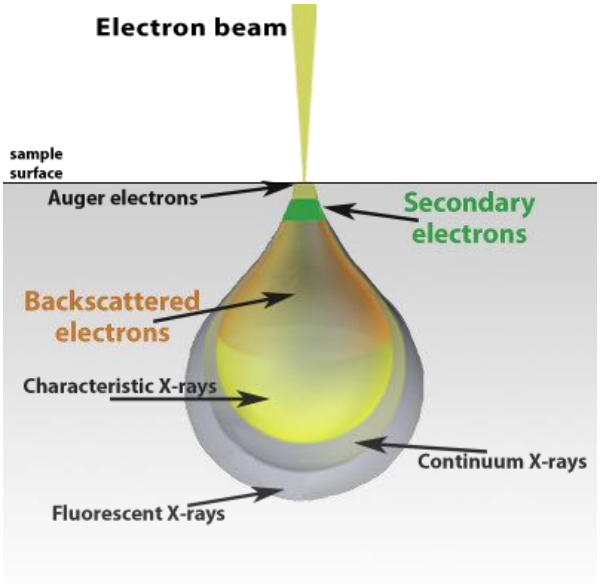

Figure 2.6- Schematic of electron beam interaction.

2.2.4.2 Scanning transmission electron microscopy (STEM)

The STEM is a type of transmission electron microscope that generates images from electrons passing through a thin sample. This image, similar to the SEM, is generated by scanning the sample with a focused electron beam. An additional objective system is needed below the sample compared with SEM in order to get the image from the samples (Figure 2.7). In addition to the signals explained in the previous section (EDS, SE and EDS), the transmission operation of these microscopes allows to obtain other signals as bright field images (BF), electron energy loss spectroscopy (EELS) and high-angle annular dark-field imaging (HAADF).

EELS is based on the identification of the energy loss process undergone by inelastic scattered electrons that go through the sample. This technique is capable of identify atomic composition, chemical bonding and surface properties among other properties of the sample. The main difference compared to the EDS is the energy resolution, being ~1 eV for the EELS and higher than 10 eV for EDS.

HAADF method is capable of generating images with atomic resolution and strongly dependent on the Z number of the elements, by means of

Rutherford-scattered electrons, i.e. electrons scattered by the interaction with the atomic nuclei of the sample.

In this work, two commercial STEMs have been used, the high resolution FEI TITAN Low-base at the Advanced Microscopy Laboratory (LMA) in Zaragoza, with a spatial resolution down to 0.09 nm in image mode, and a JEOL JEM-3010 at the University of Delaware.

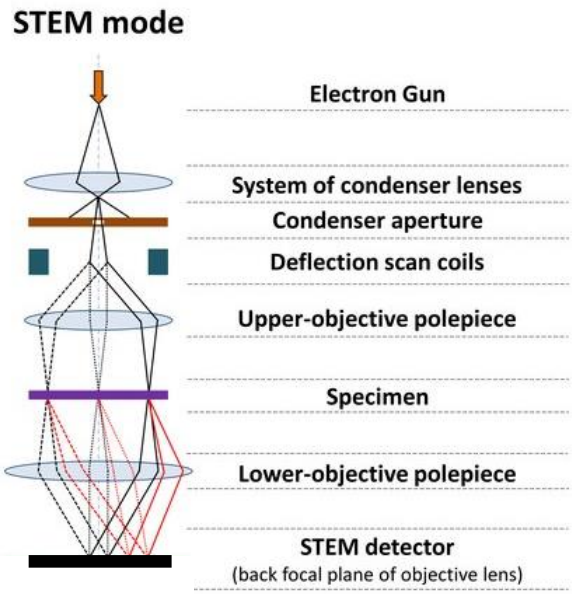

Figure 2.7- Schematic representation of a scanning transmission microscopy.

2.2.5 Magnetometry

2.2.5.1 Vibrating sample magnetometer (VSM)

The VSM is a scientific instrument used to measure the magnetization of materials that was developed by S. Foner in 1959 [7] after the development of the Vibrating-Coil Magnetometer by D.O. Smith in 1956 [8].

The Figure 2.8 shows the schematic basic operation of this system: a sample is placed within a uniform magnetic field (H) generated by a electromagnet (or by a superconducting coil) which induces a magnetic moment (m) in the sample, while a perpendicular oscillation movement is

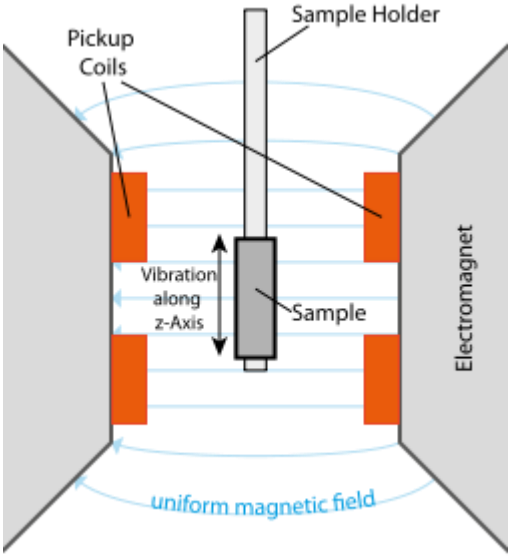

Figure 2.8- Schematic basic operation of a VSM.

applied to the sample. This uniform oscillating movement of the magnetized sample induces a voltage in the pickup coils proportional to the magnetic moment of the sample, and independent of the applied magnetic field. The obtained signal is amplified and recorded by standard techniques.

Within this work, field and temperature dependant magnetization curves have been made with two different VSMs. The first is a commercial MicroSense EZ7 with a maximum magnetic field of 2 T and a temperature range from 90 K to 1000 K. The last system is a high field VSM (HF-VSM) that has a He closed circuit refrigerated superconductor magnet that allow measurements between 2 K and 325 K with an applied magnetic field up to 14 T.

2.2.5.2 Superconducting quantum interference device (SQUID)

The operation of a SQUID magnetometer is based on the influence of magnetic flux on a Josephson junction. The basic component of a SQUID is a superconducting ring with one or two weak links. There are two different types of SQUIDs:

The dc SQUID is built with two Josephson junctions and a dc current is applied to this device. The effect of a radio frequency (RF) field on the critical current is used to detect quasi-static flux variations.

The RF SQUID is a simple ring with only one Josephson junction. Variation of the flux in the ring results in a change of impedance. This change in impedance results in detuning of a weakly coupled resonator circuit driven by an RF current source. Therefore, when a magnetic flux is applied to the ring, an induced current flows around the superconducting ring. In turn, this current induces a variation of the RF voltage across the circuit. With a lock-in amplifier this variation is detected. A feedback arrangement is used to minimize the current flowing in the ring, the size of the feedback current being a measure of the applied magnetic flux.

The sensitivity of the SQUID magnetometer ranges in 10^{-10}-10^{3} Am^2 with accuracies of 1% for typical commercial systems. In this work a Quantum Design SQUID magnetometer was used at the NCSR Demokritos.

2.2.5.3 Magnetometry data analysis.

While the coercive field is obtained directly from the hysteresis loop, other properties of the material are not so straight forward to obtain.

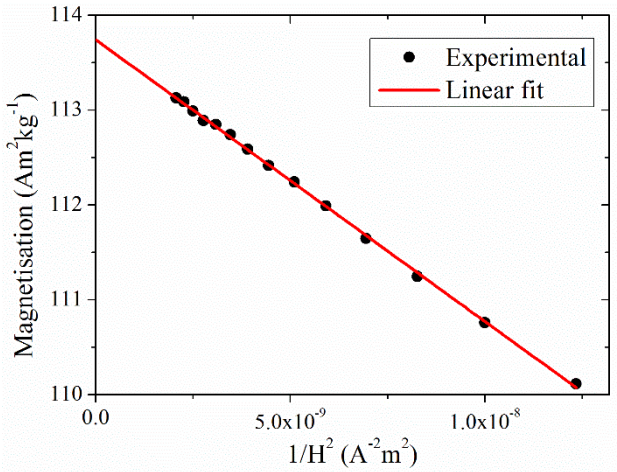

Figure 2.9- Example of fitting using the law of approach to saturation for the $SmFe_9Co_2Ti$ alloy with a saturation magnetisation $M_s \approx 114$ Am^2kg^{-1}.

The technical saturation magnetisation of the materials can be estimated by the "law of approach" to saturation [9]. In the high-field region, the magnetisation can be defined as

$$M = M_S\left(1 - \frac{a}{H} - \frac{b}{H^2}\right) + \chi H \qquad (2.2)$$

Where the term χH represents the field-induced increase in the spontaneous magnetisation of domains, which for temperatures well below T_c can be neglected, and *a* and *b* are constants. When the magnetisation of the material is represented as function of $1/H^2$ at high values of H, and fitting $M(1/H^2)$ to a linear equation, the value of M at $1/H_2 = 0$ is equal to M_s (Figure 2.9).

In order to calculate the value of the anisotropy field and the anisotropy constants (K_1 and K_2) of a material, magnetisation curves of field oriented powders are measured parallel and perpendicular to the easy axis of magnetisation. A fast and less accurate way to calculate the anisotropy field in this kind of measurements is by linearly prolonging the perpendicular curve, taking as the anisotropy field the value at which this prolongation intersects the parallel curve (Figure 2.10).

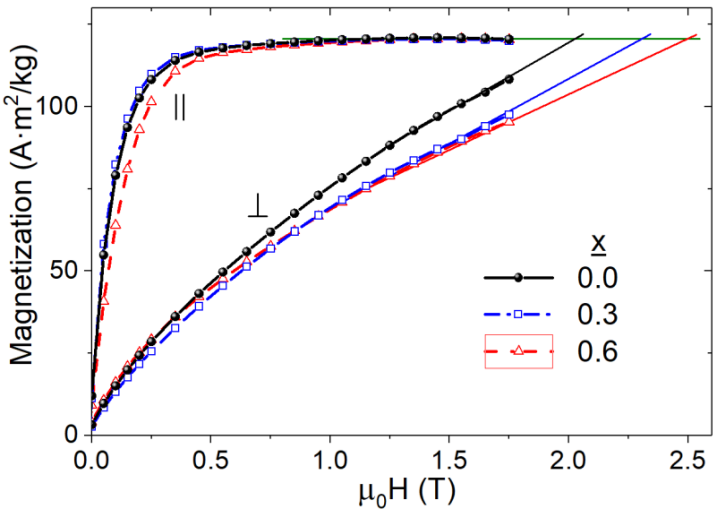

Figure 2.10- RT isotherms for field-oriented powders in parallel (∥) and perpendicular (⊥) directions to the easy axis of magnetisation. The prolongation of the curves is used to estimate the anisotropy field.

Another way to obtain the anisotropy field and the anisotropy constants is by fitting the experimental values of the magnetisation of the perpendicular curves (Figure 2.11) to the equation [9]

$$HM_s = 2K_1\left(\frac{M}{M_s}\right) + 4K_2\left(\frac{M}{M_s}\right)^3 \qquad (2.3)$$

Where H is the applied field, M_s is the saturation magnetisation, M is the magnetisation and K_1 and K_2 are the anisotropy constants. The anisotropy field can be defined as the field where M_s is reached, and can be calculated as

$$H_a = \frac{2K_1+4K_2}{M_s} \qquad (2.4)$$

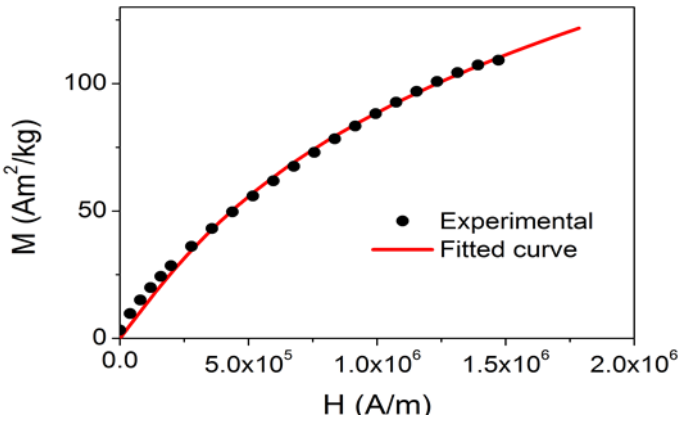

Figure 2.11- Experimental magnetisation and fitted curve of $ZrFe_{10}Si_2$.

2.2.6 Mössbauer spectroscopy (MS)

MS is based on the recoilless gamma ray emission and absorption known as Mössbauer effect, discovered in 1957 by Rudolf Mössbauer [10]. In this technique, an absorption spectra is obtained by detecting the gamma radiation that goes through a sample exposed to a gamma bean produced by a source, typically of ^{57}Co to detect ^{57}Fe atoms, as shown in Figure

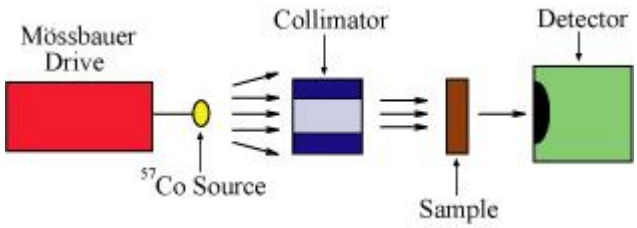

Figure 2.12- Schematic representation of the Mössbauer spectroscopy system.

2.12. When the emitting and absorbing nuclei are in identical chemical environment, the nuclear transition energies are exactly equal and resonant absorption would be observed with both materials at rest. When there is a difference in the chemical environment, the nuclear levels are slightly shifted and the resonant absorption would disappear. In order to

obtain this resonance, the energy of the gamma rays has to be slightly change, for which the relativistic Doppler effect is used by having a linear accelerated movement of the source, going through a range of velocities typically of ±11 mm/s. Three main parameters related with the modified environment can be obtained:

- The Isomer Shift (IS), is related to the non-zero volume of the nucleus and the electron charge density due to s-electrons within it. This leads to a monopole (Coulomb) interaction, altering the nuclear energy levels. The difference between the s-electron environment of the source and the absorber produces a shift in the resonance energy of the transition, which shifts the whole spectrum positively or negatively, and sets the centroid of the spectrum relative to a known absorber, usually α-Fe at room temperature. This effect allows to know the chemical state of the atoms.
- The Quadrupole Splitting (QS), appears as a consequence of the presence of an asymmetrical electric field due to the non-spherical charge distribution of nuclei states with an angular momentum quantum number $l > 1/2$. In the case of an isotope with $l = 3/2$ excited state as ^{57}Fe, the excited state is split into two substates giving a two line spectrum or "doublet". The value of the crystalline electric field gradient in each atomic position can be obtained from this parameter, and thus, the anisotropy of each position, which is related to the magnetic anisotropy by the S-O coupling.
- The Magnetic Hyperfine field (Bhf). The nuclear spin moment experiences a magnetic dipolar interaction (Zeeman splitting) with the magnetic field produced by its own atom (Fermi contact term), the surrounding ones (dipolar field) and with external applied fields, the sum of all these fields is the Magnetic Hyperfine field (Bhf). This magnetic field splits the nuclear levels with a spin l into $(2l + 1)$ substates, which for ^{57}Fe is translated to six possible transitions for a 3/2 to 1/2 transition, giving a sextet. The line positions are related to the splitting of the energy levels and give information about the magnetic moment of the atoms in each position. In case of a paramagnetic material, the atomic field fluctuation gives a $Bhf = 0$. In polycrystalline samples, without applied field, the intensity of the sextet lines follow the ratio 3:2:1:1:2:3.

In this work, MS was performed at room temperature in the transmission geometry using a conventional constant-acceleration spectrometer with a ^{57}Co-Rh source and the spectra were fitted by a least square method with the NORMOS software package developed by Brand [11].

2.3 References

[1] G. Büldt, H.U. Gally, J. Seelig, G. Zaccai, Neutron diffraction studies on phosphatidylcholine model membranes. I. Head group conformation, J. Mol. Biol. 134 (1979) 673–691. doi:10.1016/0022-2836(79)90479-0.

[2] A.C. Wright, A.C. Hannon, R.N. Sinclair, T.M. Brunier, C.A. Guy, R.J. Stewart, M.B. Strobel, F. Jansen, Neutron scattering studies of hydrogenated, deuterated and fluorinated amorphous silicon, J. Phys. Condens. Matter J. Phys. Condens. Matter J. Phys. Condens. Matter. 19 (2007) 415109–415109. doi:10.1088/0953-8984/19/41/415109.

[3] R.B. Calvert, J.R. Shapley, A.J. Schultz, J.M. Williams, S.L. Suib, G.D. Stucky, Equilibrium Isotope Effect on Hydrogen Distribution between Carbon- and Metal-Bound Sites. A Neutron Diffraction Study of Partially Deuterated Decacarbonyldihydriodomethylenetriosmium, J. Am. Chem. Soc. 100 (1978) 6240–6241. doi:10.1021/ja00487a051.

[4] J. Rodríguez-Carvajal, Recent advances in magnetic structure determination by neutron powder diffraction, Phys. B Phys. Condens. Matter. 192 (1993) 55–69. doi:10.1016/0921-4526(93)90108-I.

[5] C. Kisielowski, B. Freitag, M. Bischoff, H. van Lin, S. Lazar, G. Knippels, P. Tiemeijer, M. van der Stam, S. von Harrach, M. Stekelenburg, M. Haider, S. Uhlemann, H. Müller, P. Hartel, B. Kabius, D. Miller, I. Petrov, E.A. Olson, T. Donchev, E.A. Kenik, A.R. Lupini, J. Bentley, S.J. Pennycook, I.M. Anderson, A.M. Minor, A.K. Schmid, T. Duden, V. Radmilovic, Q.M. Ramasse, M. Watanabe, R. Erni, E.A. Stach, P. Denes, U. Dahmen, Detection of Single Atoms and Buried Defects in Three Dimensions by Aberration-Corrected Electron Microscope with 0.5-Å Information Limit, Microsc. Microanal. 14 (2008) 469–477. doi:10.1017/S1431927608080902.

[6] J.I. Goldstein, Electron Beam-Specimen Interaction, in: Pract. Scanning Electron Microsc., Springer US, Boston, MA, 1975: pp. 49–94. doi:10.1007/978-1-4613-4422-3_3.

[7] S. Foner, Versatile and Sensitive Vibrating-Sample Magnetometer, Rev. Sci. Instrum. 30 (1959) 548–557. doi:10.1063/1.1716679.

[8] D.O. Smith, Development of a Vibrating-Coil Magnetometer, Rev. Sci. Instrum. 27 (1956) 261–268. doi:10.1063/1.1715538.

[9] B.D. Cullity, C.D. Graham, Introduction to magnetic materials, Mater. Today. 12 (2009) 45. doi:10.1016/S1369-7021(09)70091-4.

[10] R.L. Mössbauer, Kernresonanzfluoreszenz von Gammastrahlung in Ir191, Zeitschrift Für Phys. 151 (1958) 124–143. doi:10.1007/BF01344210.

[11] R.A. Brand, J. Lauer, D.M. Herlach, The evaluation of hyperfine field distributions in overlapping and asymmetric Mossbauer spectra: A study of the amorphous alloy Pd 77.5-xCu6Si16.5Fex, J. Phys. F Met. Phys. 13 (1983) 675–683. doi:10.1088/0305-4608/13/3/018.

3 Dy free, Nd lean NdFeB magnets

3.1 Introduction

As it has been previously explained, the most powerful and predominant permanent magnet used nowadays is that based on $Nd_2Fe_{14}B$, crystallizing in a tetragonal structure with space group P42/mnm as shown in Figure 3.1. The crystal structure of this phase can be described as a layer structure with an alternate stacking sequence of a Nd-rich layer and a sheet formed only by Fe atoms [1]. Nd atoms are distributed in two crystallographic sites, 4*f* and 4*g*, and Fe is distributed between 6 sites (16*k1*, 16*k2*, 8*j1*, 8*j2*, 4*c* and 4*e*)

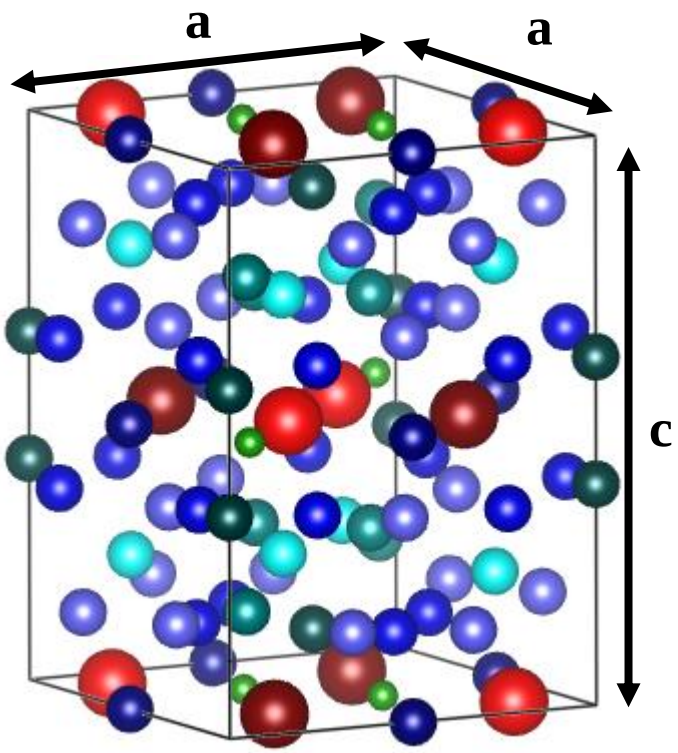

Figure 3.1-Tetragonal structure of the Nd2Fe14B. Nd atoms are represented by shades of red, B atoms are green and the different sites of Fe have different shades of blue.

As an attempt to reduce the use of rare earths, mainly the more scarce heavy rare earths, two approaches are of great interests regarding this type of magnets; exchange-coupled nanocomposites and grain boundary diffusion process (GBDP).

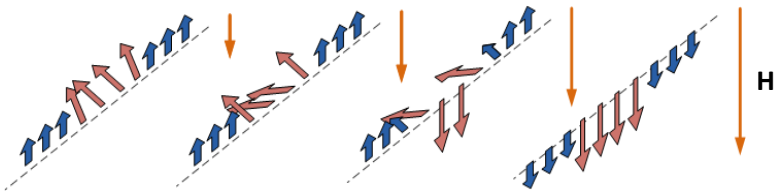

Figure 3.2- Schematic one-dimensional model of the microstructure and the micromagnetic structure of the exchange-coupled composite magnet demagnetisation. The blue arrows represents the hard phase while the brown represents the soft phase.

In 1989, Coehoorn et al. [2] discovered that the exchange coupling between phases in rapidly quenched Nd2Fe14B−Fe3B two-phase ribbons with very fine grain size enhanced the remanent magnetisation and the energy product. After this work, in 1991, Kneller and Hawig [3] proposed a theoretical treatment of an exchange-coupled hard/soft nanocomposite magnet based on the previous work of Coehoorn et al. This model showed a new approach to obtain high energy products in permanent magnet materials.

In their work, Kneller and Hawig used a one-dimensional model with alternation hard and soft regions. Figure 3.2 shows the schematic hard/soft/hard trilayer structure with inter-phase exchange-coupling. When the soft layer is thin enough, magnetic moments of the three layers will be switched coherently.

The general shape of the hysteresis loop of an exchange-coupled nanocomposite with the optimum microstructure (fine mixture) should be similar to that for a conventional single-phase permanent magnet, while if there is no exchange coupling it would be a constricted loop formed by individual contributions from the soft and the hard phase (coarse mixture) as shown in Figure 3.3.

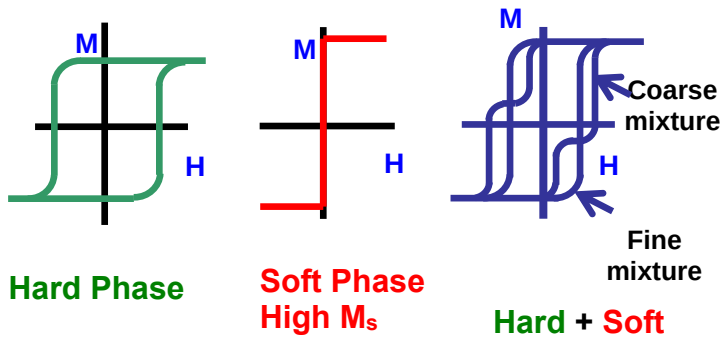

Figure 3.3- Schematic hysteresis loops of the mixture of the hard phase and the soft phase.

Another feature of this kind of magnets is that the demagnetisation curve after previous saturation will be reversible in reverse fields $H < H_{n0}$, i.e., before the magnetisation of the hard phase begins to switch as illustrated schematically in Figure 3.4. Is because of this typical magnetic behaviour, resembling a mechanical spring, that such magnets have been named exchange-spring magnets. Their unusual reversibility in conjunction with a high remanence and a high coercivity distinguishes them uniquely from the conventional single ferromagnetic phase permanent magnets, where the demagnetisation curves reflect essentially the distribution of the critical switching fields and are, therefore, mainly irreversible.

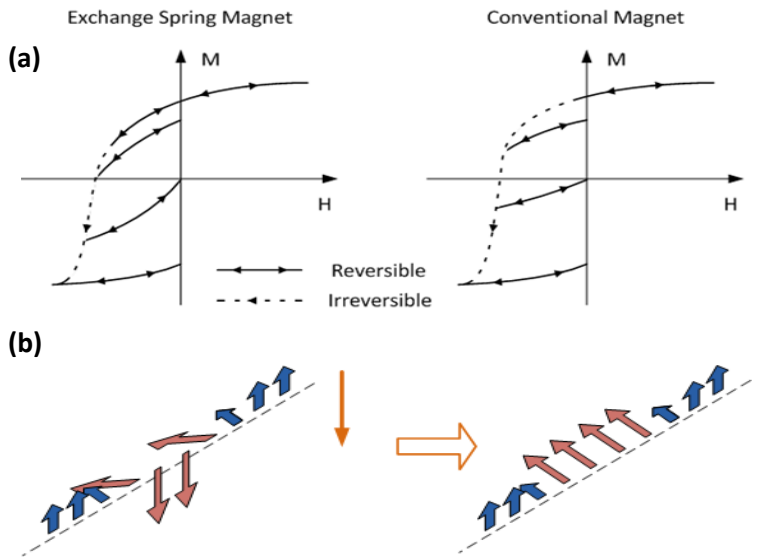

Figure 3.4- (a) Schematic demagnetisation curves for an exchange spring magnet and a conventional magnet and (b) schematic representation of the reversibility of the magnetic moments.

Schrefl et al. [4] used a finite element method to analyse a hard-soft composite structure with soft phase grains embedded in the hard phase matrix and concluded that in order to introduce magnetic hardness from the hard phase into the soft magnetic regions, a size of the soft phase region smaller than twice the domain wall width of the hard phase is required. Another result of their calculations was a value above 0.5 on the saturation remanence ratio ($m_r = M_r/Ms$).

Skomski and Coey [5] obtained a similar conclusion about the soft phase critical dimension and calculated that in an ideal Sm2Fe17N/FeCo multilayer nanocomposite structure could be possible to archive an energy product of 120 MGOe.

After the work of Kneller and Hawig, a great theoretical and experimental effort was done to obtain systems based on exchange-coupled nanocomposites, obtaining remarkable results in remanent magnetisation enhancement and energy product enhancement [6–15].

A potential candidate for the development of this kind of magnets are melt-spun Nd-lean Nd-Fe-B alloys. The amount of amorphous/disordered phase obtained with this method can be controlled using different wheel speeds [16] and tuned by small substitutions of Nb [17,18] avoiding any further treatments, but it leads to a high structural inhomogeneity compared with heat treated samples. The use of non-conventional annealing processes has been greatly useful to obtain a more uniform microstructure, such as flash annealing, which allows heat rates of 25 K/s. With this method, Nd(Pr)-lean exchange coupled magnets where obtained with a grain size of 20 nm [19].

Another way to face this issue has been to study the influence of doping on the crystallisation behaviour (microstructural engineering). Zhang et al. [20] found that the exchange-coupling could be improved, leading to a noteworthy rise of the coercivity with a minor decrease of remanence, by small Nb substitutions (Nb is a grain growth retarder) as it made the grains smaller and more homogeneous. Other compositions of Nd-lean based (Nd-Fe-Co-B) were studied with Nb and Cu substitution (Cu is immiscible and acts as nucleation points) by Wu et.al. [21], who found that the amorphous phase at the grain boundaries is enriched with Nb and B, making this phase more stable. This amorphous phase controls the grain growth during the fabrication process. Nb plays an important role during annealing, controlling the sample microstructure while Cu does not show a substantial influence on microstructure nor on magnetic properties of these alloys because their significant amount of Co may enlarge the solubility of Cu, inhibiting the clustering of Cu atoms.

The main problem of NdFeB permanent magnets is the rapidly decreasing coercivity with temperature. Addition of heavy rare earths (especially Dy and Tb) is commonly used by the industry to increase the coercivity at room temperature and to improve its temperature dependence, making

possible to use these magnets in applications that require a high-temperature operation, like electric motors and generators. However, this increase of the coercivity comes with a reduction of the remanent magnetisation as shown in Figure 3.5 [22].

In the search to avoid the use of these critical materials, GBDP through infiltration of eutectic alloys is emerging as an efficient technique to enhancing Hc and at the same time keeping the total RE content relatively low [23–25]. Most of the current work has been done using Dy-based eutectic alloys, developing Dy-rich shells in the GB. During the GBDP, the Dy is partially consumed forming Nd-Dy-O precipitates close to the flake boundary, leaving less Dy for the GBD and limiting the enhancement of the coercivity [23].

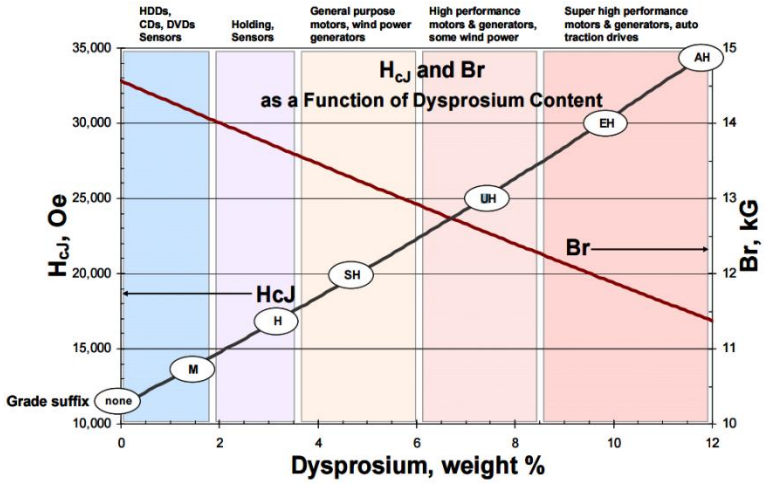

Figure 3.5- Coercivity (H_{cJ}) and Residual Induction (B_r) as a function of dysprosium content. In white circles, grade of the magnet; on top, applications for each grade.

Other interesting eutectic alloys, based on the more abundant light rare earths, have also been used as infiltration material. Among these other alloys, an emphasis has been made on Pr as it is more abundant and cheaper than the normally used Dy and Tb [26]. For example, using $Pr_{68}Cu_{32}$, the coercivity was enhanced from 1.3 to 1.8 T by GBDP on Nd-Fe-B powders made by hydrogenation-disproportionation-desorption-recombination (HDDR) [27]. Another recent work made on Nd-rich hot-deformed magnets using a similar eutectic alloy ($Pr_{90}Cu_{10}$) reported a higher coercivity enhancement (2.6 T) after GBDP [28], their analysis on the microstructure studied by 3DAP show the formation of a

$(Nd_{1-x}Pr_x)_2Fe_{14}B$ (x = 0-0.5 at.%) shell at the surface of hard grains. Recently, the latter eutectic alloy and the $Nd_3(Co_{0.75}Cu_{0.25})$ have been used to demonstrate their applicability in hard bonded magnets produced by a combination of additive manufacturing (binder jetting) and GBDP [29].

The experimental results on the development of coercivity presented in this chapter are divided in two sections, a first section in which the effect of Cu and Nb on the crystallisation process is studied, and a second section in which a GBDP is done on Nd-Fe-B ribbons with a $Pr_{25}(Co_{0.75}Cu_{0.25})_{25}$ alloy. These results have been already published at D Salazar et al 2017 J. Phys. D: Appl. Phys. 50 015305 [30] and D. Salazar et al Appl. Phys. Lett. 113, 152402 (2018) [31] respectively.

3.2 Developing coercivity on Nd-lean NdFeB phases by grain boundary diffusion

3.2.1 Effect of Nb and Cu on the crystallisation behaviour

In this section of the work, I report the effect of small additions of Nb and Cu on Nd-lean Nd-Fe-B samples. A total of 4 compositions were prepared by arc-melting the pure constituents: $Nd_{12}Fe_{81}B_6Nb_1$, $Nd_{10}Fe_{84}B_6$, $Nd_9Fe_{84}B_6Nb_1$ and $Nd_9Fe_{84}B_6Nb_{0.5}Cu_{0.5}$ (Table 3.1). These alloys were consequently melt-spun at wheel speeds of 15-40 m/s under Ar atmosphere. In order to induce the crystallisation of the amorphous ribbons obtained, the samples were annealed in quartz tubes under vacuum at a temperature between 600 ºC and 800 ºC for times from 15 to 120 minutes.

A first DTA and XRD study to identify the thermal processes that the alloys undergo as a function of temperature was done to choose the annealing temperatures.

The XRD spectra and the DTA measurements for the different alloys are shown in Figure 3.6. The XRD spectra show that for wheel speeds of 26 and 40 m/s, the ribbons are found in an amorphous state, while for a wheel speed of 15 m/s a crystalline order is observed (Figure 3.6 a). The analysis of this data shows that the crystalline phases present on 9NFBNC_15 as-spun ribbons correspond to the 2:14:1 hard magnetic phase (•) and the secondary α-Fe phase (§), formed by the excess of Fe present in the alloy.

Table 3.1- Sample compositions, sample quotation and crystallisation temperature of the Nd-Fe-B phase (T_1) and the α-Fe (T_2) determined by DTA and XRD.

Sample	Quote	$T_{1\text{-DTA}}$ (ºC)	$T_{1\text{-XRD}}$ (ºC)	$T_{2\text{-DTA}}$ (ºC)	$T_{2\text{-XRD}}$ (ºC)
$Nd_{10}Fe_{84}B_6$ at 26 m/s	10NFB_26	323-367	360	577	600
$Nd_9Fe_{84}B_6Nb_{0.5}Cu_{0.5}$ at 40 m/s	9NFBNC_40	265-342	415	595	---
$Nd_9Fe_{84}B_6Nb_1$ at 40 m/s	9NFBN_40	351-376	440	610	---
$Nd_9Fe_{84}B_6Nb_{0.5}Cu_{0.5}$ at 15 m/s	9NFBNC_15	---	---	---	---
$Nd_{12}Fe_{81}B_6Nb_1$ at 26 m/s	12NFBN_26	276-348	---	611	---

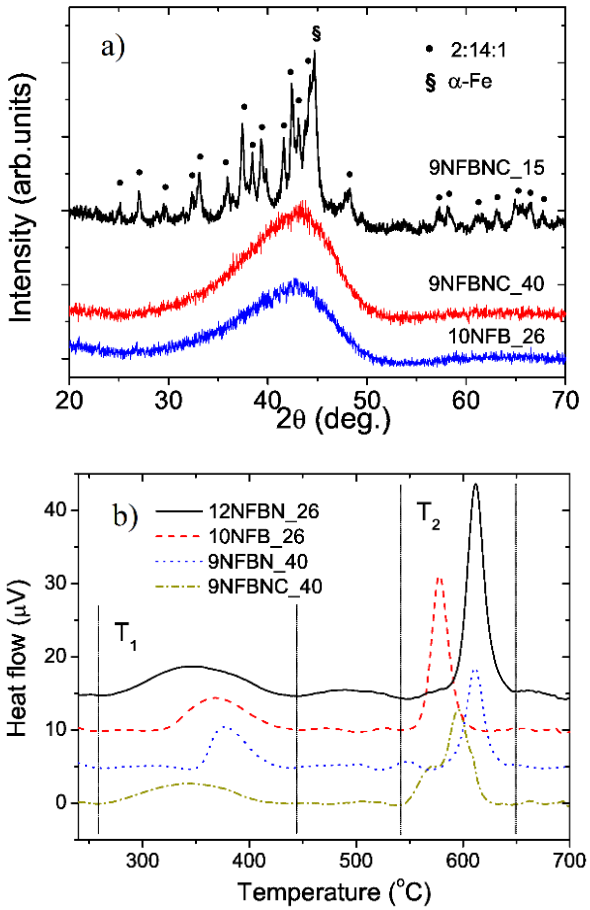

Figure 3.6- a) X-ray diffraction of selected as-spun samples and b) DTA analysis of crystallisation processes in amorphous Nd-Fe-B-based samples

As it was expected, the DTA data (Figure 3.6b) shows two exothermic peaks corresponding with the crystallisation of two phases, a first broader peak at temperatures around T_1 (~350 ºC) which corresponds with the crystallisation of the $Nd_2Fe_{14}B$ phase (as can be seen in Figure 3.7), and a second sharper peak at the higher temperature T_2 (~600 ºC) that can be associated with the crystallisation of the α-Fe phase. Table 3.2 shows a summary of the crystallisation temperatures for each sample, from which values the effect of Nb and Cu addition on their behaviour can be extracted. The addition of Nb in the samples affects mainly to the crystallisation temperature of the secondary α-Fe phase, increasing its crystallisation temperature from 577 ºC, in samples without Nb, to 611 ºC in samples with 1 at% Nb. Regarding this crystallisation process, the larger

heat flow shown on samples made with lower wheel speed (26 m/s) can be associated with the presence of α-Fe nuclei in the as-spun ribbons, which would act as facilitators for the crystal growth. This is corroborated with the smaller heat flow at T_2 shown by more disordered samples made at higher wheel speeds. The onset of the T_1 peak is associated with the nucleation of the 2:14:1 phase, in which the addition of Cu has a clear influence, decreasing this temperature. In that way, the nucleation occurs before in the sample with Cu (9NFBNC_40), $T_1 \approx 265$ ºC than in the one without Cu (9NFBN_40), $T_1 \approx 351$ ºC. These results suggest that the

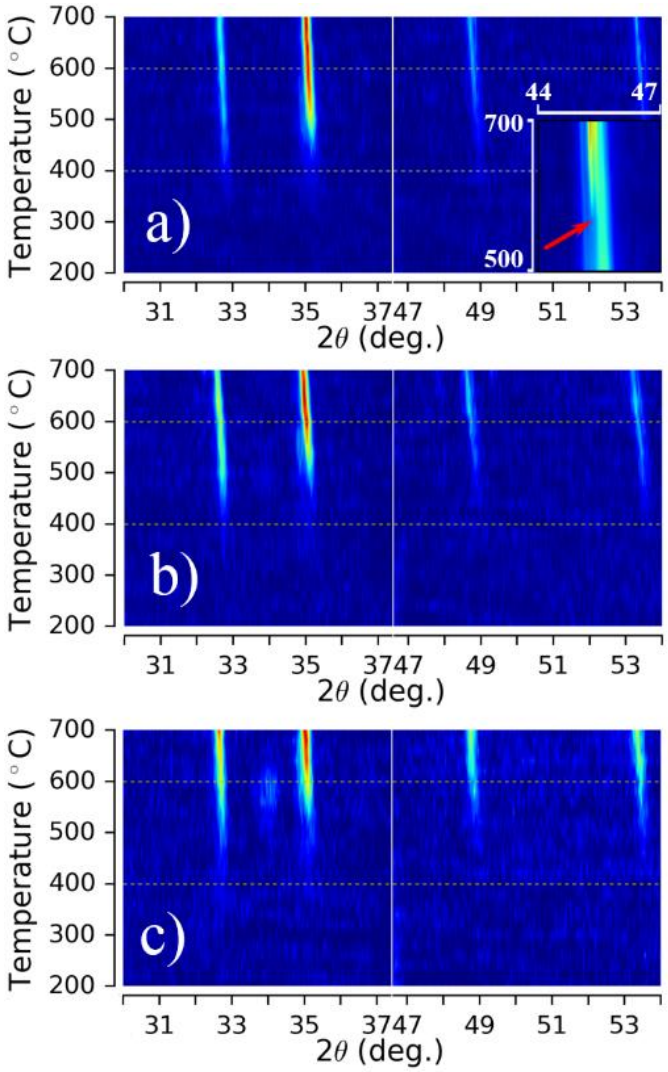

Figure 3.7- X-ray thermodiffraction profiles of amorphous ribbons: a) 10NFB_26, b) 9NFBNC_40 and c) 9NFBN_40. Inset. Evidence of splitting of diffraction peak corresponding to Pt at 2θ=45º due to the crystallisation of α-Fe phase.

crystallisation temperatures of both phases, 2:14:1 and α-Fe, are mainly influenced by the addition of Nb and Cu, rather than by the initial structural state of the sample.

The thermal processes described previously are related with the nucleation of stable phases and can be associated with the formation of their corresponding crystalline structures, which can be quantitatively identified by X-ray diffraction experiments on annealed amorphous samples at the crystallisation temperatures.

Once the different crystallisation processes have been identified, thermal annealing of the amorphous ribbons are done at temperatures between the two identified temperatures T_1 and T_2 looking for the optimum grain size and hard/soft phase ratio. The crystal structures and the amount of each crystallised phase in the samples can be obtained by XRD experiments.

X-ray thermo-diffraction spectra for a) 10NFB_26, b) 9NFBNC_40 and c) 9NFBN_40 are shown in Figure 3.7. In the setup of this experiment, the sample-holder is made of Pt, which has its main diffraction peaks at $2\theta \sim 39^{\circ}$ and 45°, overlapping with the characteristic peak of the α-Fe phase around 45° (see Figure 3.6a). For this reason, the X-ray spectra are presented with a gap between 37°-47°. A huge drawback comes with the quantitative analysis of these spectra due to this sample-holder contribution as it denies the possibility to quantify the amount of α-Fe on the samples, except for the 10NFB_26 sample, where a peak appears slightly below 45° corresponding to the α-Fe phase as observed in the inset of Figure 3.8. The appearance of this peak occurs around 600 ºC, close to the temperature observed by DTA. In contrast, the crystallisation of the 2:14:1 structure is well detected in all the samples spectra at temperatures around 350 ºC. The temperatures of crystallisation obtained from XRD are higher than those found by DTA as shown in Table 3.1. This discrepancy occurs because the peaks of XRD appears when there is a minimum of crystalline order in the sample, which occurs some time after the crystallisation starts, and so, as the temperature is sweeping continuously, at higher temperature.

By means of a sequential Rietveld refinement of the X-ray thermo-diffractions, it is possible to quantitatively calculate the amount of the different phases appearing along the annealing process and the temperature at which they are formed. However, due to the problem with the Pt contribution, only relative values of the phases concentration obtained from these refinements are shown in Figure 3.8.

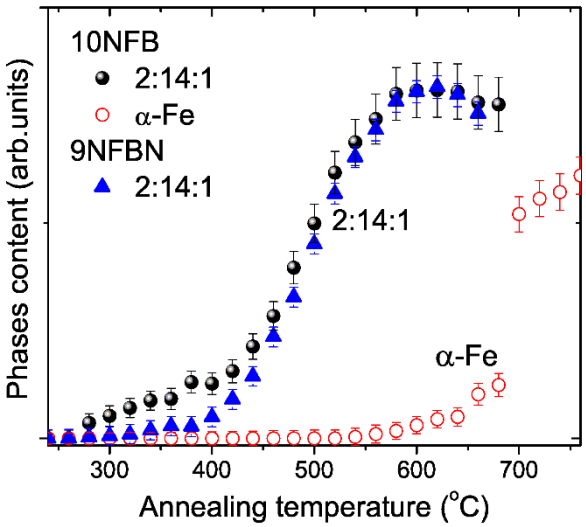

Figure 3.8- Evolution of phases obtained from X-ray thermodiffraction profiles fitted by the Rietveld method.

The results presented up to now give a deep vision of the crystallisation behaviour of these alloys, allowing a better procedure planning to obtain an optimised microstructure. The heat treatments that these samples have to undergo must lie between the temperatures of both crystallisations, with the intention to obtain $Nd_2Fe_{14}B$ grains with an optimal size but without an excessive growth of the α-Fe phase in order to obtain the maximum coercivity [32]. In Figure 3.9 are shown the representative results for the 9NFBN_40 and 9NFBNC_40 samples. The inset shows the maximum coercivity that was obtained for each annealing temperature.

The as-spun ribbons present a very small coercivity as expected for an amorphous/highly disordered alloy. This coercivity increases sharply with the annealing temperature up to a critical temperature at which the amount/size of the α-Fe phase is too large, promoting easy nucleation of reversed domains, which leads to low coercivity. As previously discussed, to obtain a good exchange-coupling between the hard and the soft phases, the later should have, at most, double the size of the domain

wall of the hard magnetic phase, which for Nd-Fe-B is around 5 nm, and this would lead to an increased remanence and a minor decrease of coercivity. The hysteresis loops in Figure 3.9 show the typical shapes that can be found in these systems. The samples heat treated at the lowest temperature (650 ºC) present a clearly constricted shape, indicating the presence of two uncoupled phases. In the case of the most disordered samples, 9NFBN_40 and 9NFBNC_40, the maximum H_c was obtained after annealing at 750 ºC for 120 and 60 minutes, showing a reduced remanence $m_R = M_R/M_s$ of 0.64 and 0.57 (the M_s of these samples was estimated by the law of approach to saturation) respectively, which, together

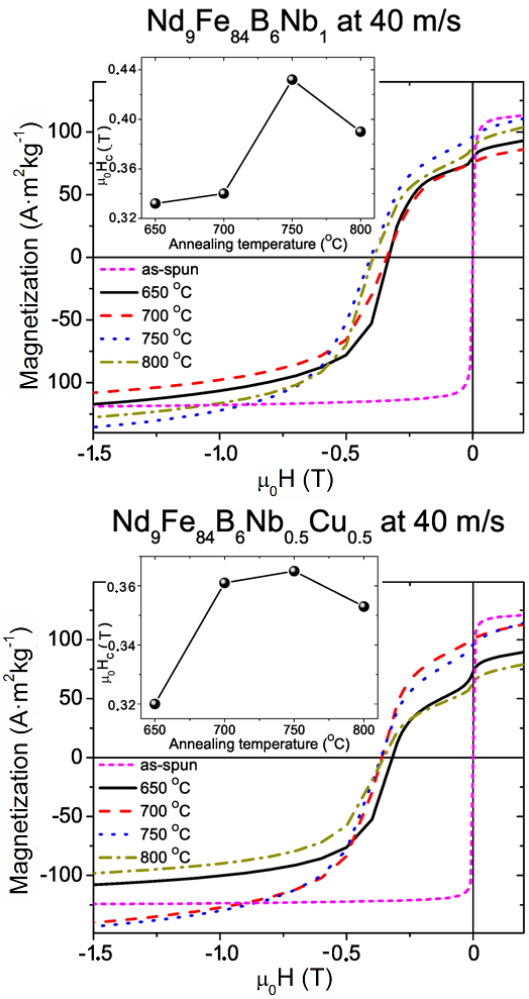

Figure 3.9- Hysteresis loops of samples a) 9NFBN_40 and b) 9NFBNC_40 heat treated between 650 and 800 ºC at different times.

with a smooth single-phase like hysteresis loop, indicates a good exchange-coupling between both magnetic phases. Samples that were annealed at higher temperatures and for longer times showed a reduced coercivity together with a constricted hysteresis loop, showing again the decoupling of both magnetic phases present at the sample due to an excessive growth of the soft magnetic phase.

The results of the coercivity obtained for all the heat treatments performed to the different samples are summarised in Figure 3.10. The samples containing Nb were annealed at higher temperatures to overcome the inhibition of grain growth effect of this element [21]. On the other hand, it was found that Cu facilitates the early appearance of the hard magnetic phase, because early nucleation can promote grain growth at lower temperatures. Such an effect disagrees with the results obtained by Wu's group [21], where no increase of the crystallization of the hard phase at low temperatures was observed. In their case, however, the presence of Co in the alloy increased the solubility of Cu in the amorphous region of the ribbons, which neutralise the effect of Cu on the nucleation of the hard phase. Due to the effect of these two elements in the crystallisation behaviour, it is possible to obtain samples with different microstructure at the same annealing conditions.

The sample with the highest $\mu_0 H_c$ was the near stoichiometric alloy 12NFBN_26, with a value of 1.1 T, reached after annealing it at temperatures between 650 ºC and 700 ºC. The Nd-lean Nd-Fe-B-Nb-Cu ribbons obtained at 40 m/s showed a maximum coercivity of 0.37 T after treating them for 60 minutes at 750 ºC, showing a dropping of the coercivity when annealed at the same temperature for longer times. This coercivity obtained is higher than that for the 9NFBN_40 for the same heat treatment ($\mu_0 H_c \approx 0.33$ T), but in this case, the coercivity continues growing with longer annealing up to 120 minutes. In both cases, the use of higher temperatures worsens the coercivity due to the excessive growth of the α-Fe phase.

In an attempt to get closer to the optimum grain size for the maximum coercivity of the hard phase avoiding the formation of large amounts of the α-Fe phase, nanocrystalline ribbons of 9NFBNC_15 were prepared at wheel speeds of 15 m/s. The as-spun ribbons of this sample had a nanocomposite structure with a relatively high coercivity (>0.05 T), due to the proper grain size and lack of excess α-Fe phase. In nanocrystalline ribbons, a coercivity ≥ 0.6 T could be obtained at lower annealing temperatures (650 ºC – 90 min) or higher temperature, but shorter time (700 ºC – 30 min) than those used for amorphous ribbons, like the 9NFBNC_40 sample.

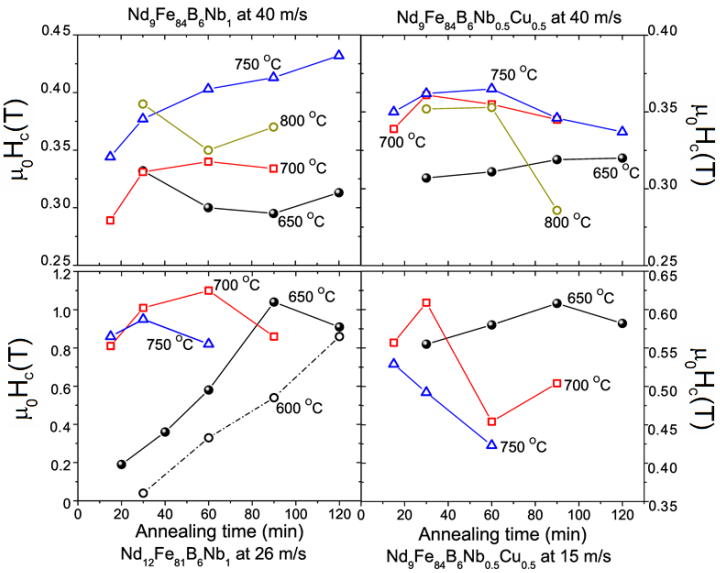

Figure 3.10- Coercive field of ribbons heat treated at different temperatures and times.

XRD was done on the ribbons with the highest coercivity for each composition and analysed by the Rietveld method to evaluate the phase ratio of the phases present in the samples and the crystallite sizes. The X-ray spectra for selected heat treated samples and their refinement are shown in Figure 3.11. The lattice parameters of the $Nd_2Fe_{14}B$ phase were constant in all samples with values of $a = 8.80$ Å and $c = 12.21$ Å. However, the phase ratio obtained with these refinements of the XRD spectra is not very reliable as most samples display a pronounced texture. If we compare the value obtained by this method with the nominal one considering the excess of Fe present in the composition for the samples melt-spun at 26 m/s, for the Nd-lean 10NFB_26 a 60% of α-Fe was estimated

from XRD, which is much higher than the nominal value of 16.7%, whereas for the stoichiometric 12NFBN_26 the estimated value was 5%, very close the nominal 0%. These discrepancies led to a different approach to estimate the amount of each phase by Mössbauer spectroscopy.

As previously shown, the $Nd_2Fe_{14}B$ phase present 6 non-equivalent crystallographic sites for Fe (16*k1*, 16*k2*, 8*j1*, 8*j2*, 4*c* and 4*e*), each of them contributing with a magnetic sextet to the Mössbauer spectrum. In order to better determine the distribution of the Fe atoms after crystallisation among the α-Fe and $Nd_2Fe_{14}B$ and to simplify the analysis of the spectra, the relative areas of the six sextets of the $Nd_2Fe_{14}B$ assumed to have the original populations: 16:16:8:8:4:4 for the sites 16*k1*, 16*k2*, 8*j1*, 8*j2*, 4*c* and 4*e* respectively.

The Mössbauer spectra of selected samples are shown in Figure 3.12. From these spectra is possible to see that they are composed of seven sub-spectra, one sextet for the α-Fe phase and six sextets for the $Nd_2Fe_{14}B$ phase, which indicates the ferromagnetic behaviour of both phases at room temperature. It is worth noticing that in the case of 9NFBNC_40 it was necessary to include an extra paramagnetic contribution to get a better refinement, but the contribution of this phase was estimated to be 1 at% and was not evidenced in the XRD nor in the magnetic characterisation. The value of the different phase distribution for each alloy obtained by Mössbauer spectroscopy, is close to the nominal value, as displayed in Table 3.2.

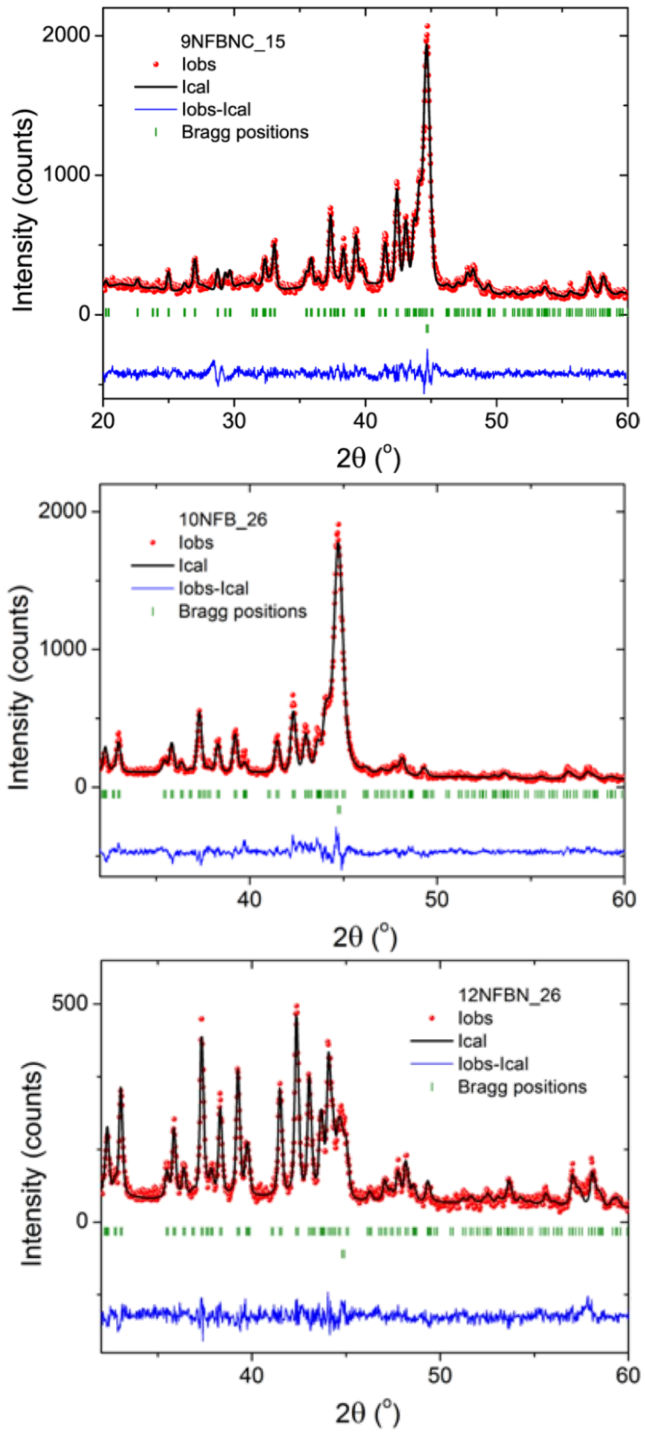

Figure 3.11- Refinement of X-ray powder diffraction for samples 9NFBNC_15, 10NFB_26 and 12NFBN_26 with maximum Hc with Rietveld refinement.

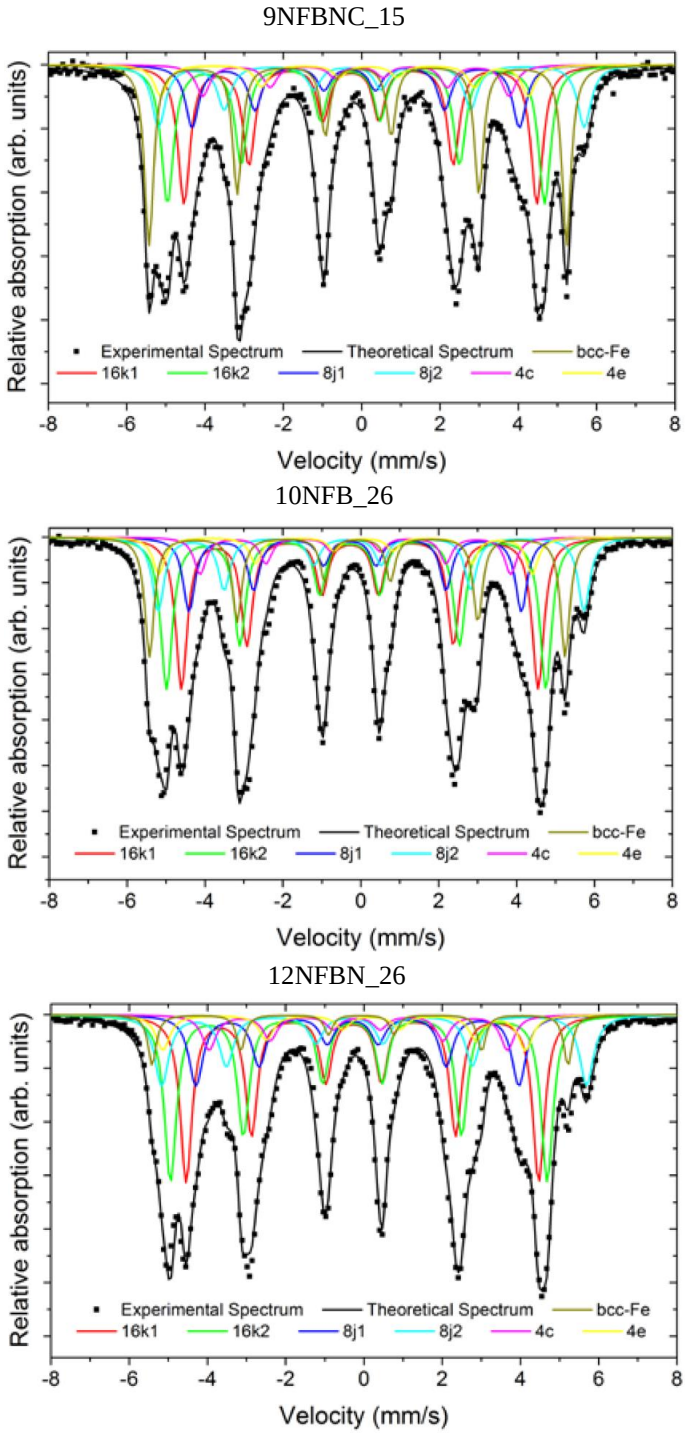

Figure 3.12- Mössbauer spectra (at room temperature) of 9NFBNC_15, 10NFB_26 and 12NFBN_26 samples with the best coercivities.

It is important to see the interrelations between the different parameters displayed in Table 3.2. The sample with the highest coercivity (1.1 T) is the stoichiometric 12NFBN_26. At the same time it presents the lowest value of α-Fe phase content (5.8%) and of saturation magnetisation (106.5 $A \cdot m^2 \cdot kg^{-1}$); and the best coupling between phases, as deduced from the highest m_R value of 0.72. On the other hand, the sample 9NFBNC_40, which has the lowest coercivity (0.37 T), also shows the highest amount of α-Fe phase (23.8%) and the largest value of saturation magnetisation (169.3 $A \cdot m^2 \cdot kg^{-1}$). These values go together with the worse exchange coupling represented by a value of $m_R = 0.57$. However, the sample with the same composition but melt-spun at lower wheel speed, 9NFBNC_15, presents the highest coercivity for the Nd-lean samples (0.61 T) and a slightly higher $m_R = 0.64$, indicating a better exchange coupling.

To analyse the dependence of the hard magnetic properties of the samples on the microstructure, the grain size was estimated by SEM and XRD. The values obtained by analysis of the X-ray spectra were not very accurate, as values near 100 nm fall in the upper limit for their estimation by X-rays. Figure 3.13 shows the micrograph of the heat-treated 12NFBN_26 sample. The values for the grain sizes, summarised in Table 3.2, are at the single/multi-domain threshold, which in the case of $Nd_2Fe_{14}B$ is 77-120 nm [33].

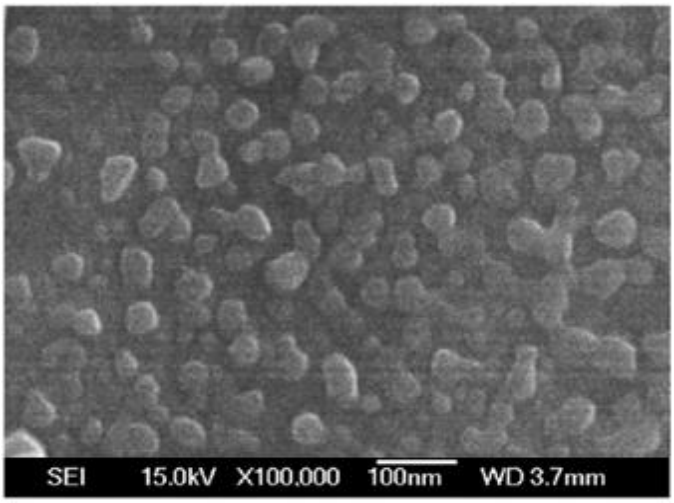

Figure 3.13- SEM image of 12NFBN_26 heat treated at 700 ºC for 60 minutes.

Table 3.2- Summary of best heat treated samples, heat treatments, coercive field, saturation magnetisation, normalised remanence, phase contents obtained by Mössbauer and estimated from nominal composition (in brackets) and grain size observed from XRD and by SEM, when available (in brackets).

Sample	HT (ºC min)	$\mu_0 H_c$ (T)	M_s ($A \cdot m^2 \cdot kg^{-1}$)	M_r/M_s	$Nd_2Fe_{14}B$ (%)	α-Fe (%)	Grain size (nm)
10NFB_26	650-60	0.51	123	0.71	84.7 (83.3)	15.3 (16.7)	80 (125)
9NFBNC_40	750-60	0.37	169	0.57	75.2 (75)	23.8 (25)	>100
9NFBN_40	750-120	0.43	143	0.64	82.7 (75)	17.3 (25)	88
9NFBNC_15	700-30	0.61	148	0.64	78.2 (75)	21.8 (25)	>100 (90)
12NFBN_26	700-60	1.1	106	0.72	94.2 (100)	5.8 (0)	98 (48)

3.2.2 Coercivity enhancement by grain boundary diffusion process

In this section of the work, I present the study of the effect of the grain boundary diffusion of a non-magnetic rare earth-based eutectic alloy in the magnetic properties of the $Nd_2Fe_{14}B/\alpha$-Fe nanocomposite was studied. The eutectic alloy used was arc-melted $Pr_{75}(Co_{0.75}Cu_{0.25})_{25}$, having a melting point of 560 ºC. Four compositions with different amounts of Nd were prepared by arc-melting the pure constituents; $Nd_{10}Fe_{84}B_6$ (Nd10), $Nd_{11}Fe_{83}B_6$ (Nd11), $Nd_{12}Fe_{81}B_6Nb_1$ (Nd12) and $Nd_{13}Fe_{81}B_6$ (Nd13). All these samples were consequently melt-spun at a wheel speed of 26 m/s and annealed in quartz tubes under vacuum at a temperature of 700 ºC for 60 minutes. This annealing process was selected as it gave the best magnetic properties on all samples. For the GBDP, small pieces of the eutectic alloy were placed in a quartz tube together with the nanocrystalline ribbons with a mass ratio of 5:1 (Nd-Fe-B: Pr-Co-Cu) under controlled Ar atmosphere using a glove box and then sealed under vacuum. The samples were afterwards heat-treated at 600 ºC for 1-6 hours. This temperature is enough to facilitate the infiltration process in the 25-30 µm thick ribbons, and not so high that it could lead to excessive grain growth.

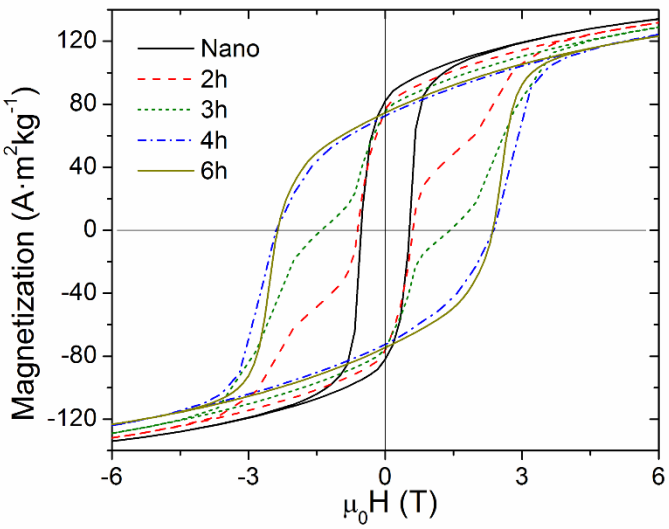

Figure 3.14- Hysteresis loops of Nd-Fe-B ribbons infiltrated at 600 ºC during different times.

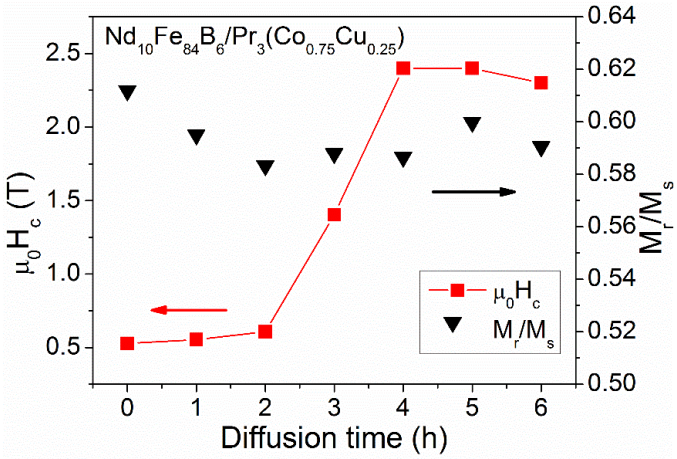

Figure 3.15- Coercivity and reduced remanence of Nd-Fe-B ribbons infiltrated at 600 ºC during different times

The GBDP produces a continuous enhancement of coercivity as a function of infiltration time, as can be appreciated in Figure 3.15, while the remanence remains nearly constant. The hysteresis loops of the ribbons shown in Figure 3.14 show a great enhancement of the coercivity with the infiltration time, from 0.53 T for initial nanocrystalline ribbons to 2.5 T for 4 hours and longer times. For intermediate times (1, 2 and 3 hours) the ribbons present a hysteresis loop with a constricted shape, evidencing the presence of two phases, an infiltrated phase in the outer region of the ribbons, and a not-infiltrated phase in the inner part where the eutectic alloy couldn't reach for those times. For 4 hours and more, the infiltration is even throughout the ribbon, and the hysteresis loops have a uniform single phase like shape. However, as the eutectic alloy is non-magnetic, a reduction of the magnetisation is expected. The saturation magnetisation decreases from 140 $A \cdot m^2 \cdot kg^{-1}$ to 130 $A \cdot m^2 \cdot kg^{-1}$, while the remanence is decreased from 87 $A \cdot m^2 \cdot kg^{-1}$ to 74 $A \cdot m^2 \cdot kg^{-1}$. The estimated $(BH)_{max}$ for the completely infiltrated sample was 87 $kJ \cdot m^{-3}$, which is a reasonable value for isotropic magnets but could be highly improved by texturization.

In Figure 3.16 can be seen how the XRD intensity that corresponds to the α-Fe phase that is formed during the crystallisation of the sample (at $2\theta \approx 44.7º$) decreases with infiltration time, disappearing completely after 6 hours. This reduction of the α-Fe can be seen as a reaction with the Pr_2(Co,Cu) alloy, transforming into a new phase containing Fe and Pr.

As XRD do not show any new peak, it is probable that this new phase is a $(Pr,Nd)_2Fe_{14}B$ compound.

In Figure 3.17 can be seen the difference between the samples with different amount of Nd. These values are also summarised in Table 3.3. As seen in Table 3.3, the FWHM of the peak corresponding with the [214] reflection of the $Nd_2Fe_{14}B$ phase remains rather similar for the different samples, suggesting a grain size of comparable dimensions for all the samples. With this in mind, the variation on the coercivity on the nanocrystalline ribbons with different compositions before infiltration can be associated with the different amount of α-Fe phase. As happened in the previous section, values of phase amounts obtained by analysing the XRD spectra gave values too far from the nominal ones, so Mössbauer spectroscopy was used again as a more reliable analysis of this parameter.

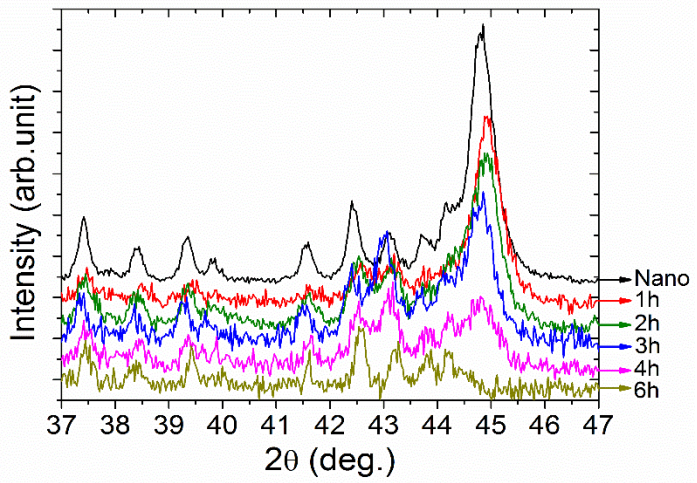

Figure 3.16- XRD of Nd-Fe-B ribbons infiltrated at 600 ºC during different times.

Table 3.3- Summary of the most relevant results obtained for the samples; coercive field of the nanocrystalline ribbons before GBDP, coercive field after being infiltrated for 4 hours, $Nd_2Fe_{14}B$ phase amount before infiltration, α-Fe phase amount before infiltration and FWHM of the $Nd_2Fe_{14}B$ [214] XRD peak

Sample	$\mu_0 H_c$ nanocrystalline (T)	$\mu_0 H_c$ infiltrated (T)	$Nd_2Fe_{14}B$ (%)	α-Fe (%)	FWHM [214] (2θ)
Nd10	0.44	2.4	84.7	15.3	0.21274
Nd11	0.56	2.4	84.6	15.4	0.22083
Nd12	1.01	1.14	94.2	5.8	0.21057
Nd13	0.82	2.6	95.5	4.5	0.24301

After infiltration, the coercivity is enhanced up to ~2.5 T in all samples, except in the stoichiometric Nd12 one, which remains almost unchanged. This behaviour gives an insight of the importance of the α-Fe phase in order to get an effective GBDP but the behaviour of the Nd13 sample cannot be explained with this hypothesis, suggesting a different enabler of the infiltration in this sample.

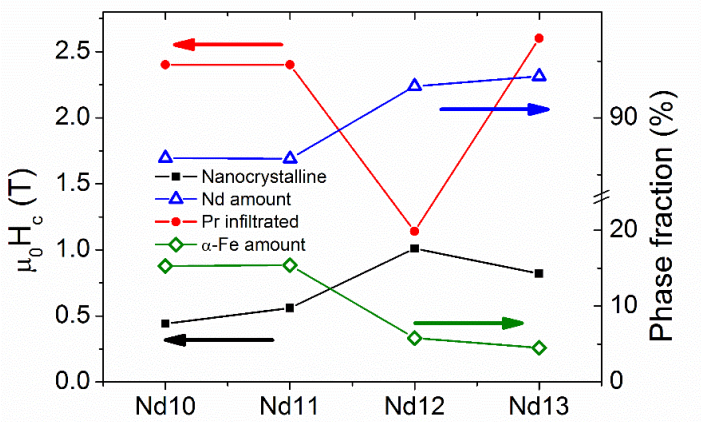

Figure 3.17- Evolution of coercivity before (black) and after (red) GBDP and amount of α-Fe (green) and $Nd_2Fe_{14}B$ (blue) phases for compositions with different amount of Nd.

A suitable tool to give a vision on the structure and composition is STEM with EDS. A preliminary study was carried out on a JEOL JSM 6330F, showing the most relevant images in Figure 3.18. The STEM image was taken on the sample before infiltration shows dark spots of ~15 nm diameter that correspond with grains of the segregated α-Fe phase and some bright spots that correspond with a Nd-rich phase. The grain size estimated of the $Nd_2Fe_{14}B$ phase is around 100-150 nm, in the frontier between single/multi-domain size as mentioned in the previous section, which remains similar after the infiltration. The elemental mapping done

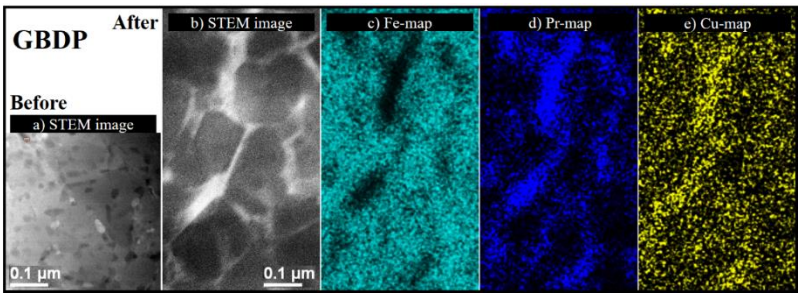

Figure 3.18- STEM images and elemental mapping for Fe, Pr and Cu on $Nd_{10}Fe_{84}B_6$ ribbons infiltrated for 4h.

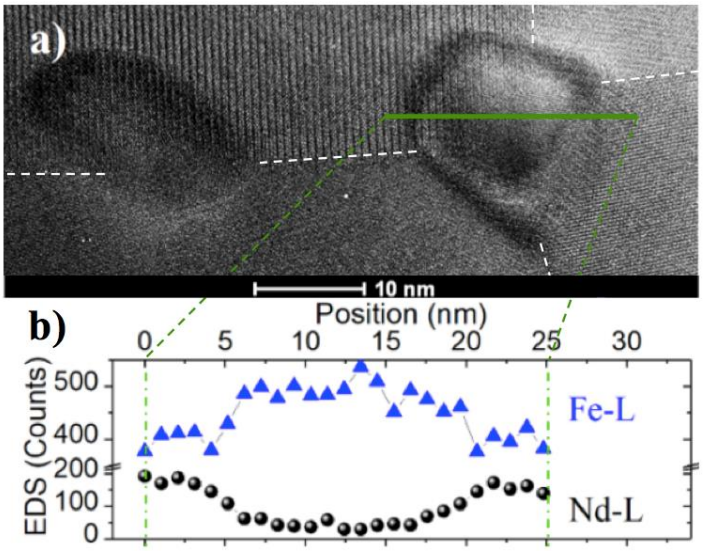

Figure 3.19- High-resolution image (a) and compositional profile across a typical Fe-rich precipitate (b) obtained by EDS on a $Nd_{10}Fe_{84}B_6$ ribbon before infiltration.

by EDS shows the presence of a Fe-rich phase within the grains and a Pr-rich phase at the boundaries. This boundary phase seems to contain also the Cu. However, the low resolution of this microscope averts more detailed studies.

In order to have a better understanding of the GBDP and the mechanism of coercivity enhancement, a high-resolution STEM, (an FEI TITAN equipped with X-Ray (EDS) and Electron Energy Loss Spectroscopies

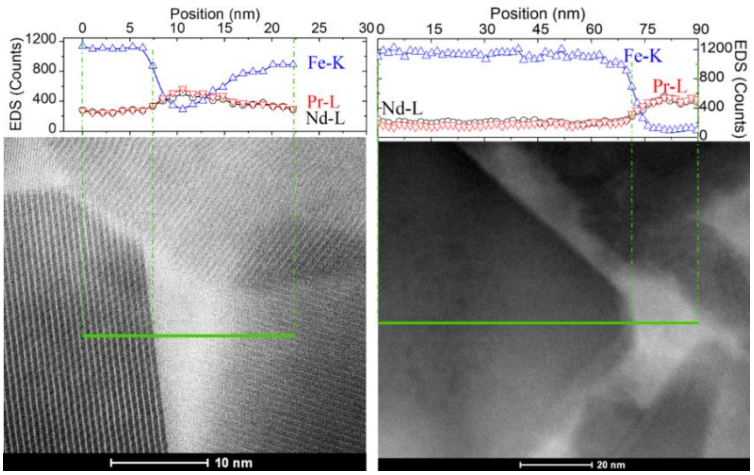

Figure 3.20- HAADF image and compositional profile obtained by EDS analysis on $Nd_{10}Fe_{84}B_6$ ribbons after GBDP. Peaks from the EDS spectrum are Fe-K_α, Pr-L_α and Nd-L_α.

(EELS)) of the Advanced Microscopy Laboratory (LMA) in Zaragoza was used. Figure 3.19 shows the HAADF-STEM image of a ribbon before infiltration in a region surrounding an α-Fe precipitate. It is clearly seen how the α-Fe segregates at the surface and corner junction of hard magnetic grains. The size of this particular cubic soft magnetic grain is 15 nm as estimated from the low-resolution STEM images, and its composition can be characterised by Fe-L_α and Nd-L_α EDS profiles. As expected, the Nd is reduced almost to zero inside the grain while the Fe increases, confirming the formation of α-Fe grains due to the Nd deficiency in the initial composition. These soft magnetic grains are possible domain wall nucleation sites resulting in low coercivity (~0.53 T, values comparable with those obtained previously in similar systems [34]).

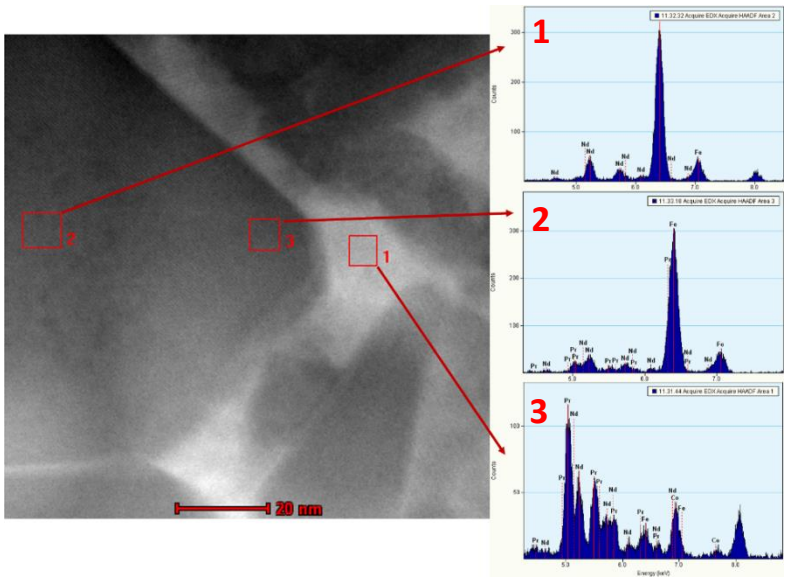

Figure 3.21- EDX spectra of a sample infiltrated during 6h at the inter-grain Pr,Nd-rich region (1), well inside the grains with pure $Nd_2Fe_{14}B$ phase (2) and close to the surface with a (Pr,Nd)$Fe_{14}B$ phase (3).

Images obtained from samples after the infiltration are shown in Figure 3.20 and Figure 3.21. Here it is possible to see an abrupt structural and compositional change at the edge of the hard magnetic phase grains, confirming that the EDS analysis has enough spatial resolution to determine compositional changes at the thin boundary phase. Looking at the evolution of the Fe-K_α, Pr-L_α and Nd-L_α signals of the EDS profiles it is noticeable the presence of Nd together with Pr in the intergranular phase. At the same time, the Fe content is sharply diminished at the edge of the

grain, confirming the existence of a rare earth-rich PrNd-Fe intergranular phase after infiltration. Figure 3.21 shows the results of a semi-quantitative compositional analysis around the edges of the grains. This analysis shows that the samples present an outer shell made of a $(Pr,Nd)_2Fe_{14}B$ phase. This shows that the Pr is diffused inside the grains as well as Nd is diffused into the intergranular phase. However, well inside the grains, there is no presence of Pr and the hard phase is a pure $Nd_2Fe_{14}B$. Cu and Co remain mostly in the intergranular phase.

In all former studies found in literature, the highest coercivity obtained by GBDP was achieved by the infiltration of $Nd_{62}Dy_{20}Al_{18}$, increasing the coercivity from 0.91 to 2.75 [35]. The formation of a thick Nd-rich intergranular phase and a Dy-rich shell at the surface of the grains promotes a magnetic isolation of the grains, which increases the nucleation field for reversal magnetisation.

The infiltration made in this work results in the disappearance of the soft α-Fe phase and the formation of a non-magnetic Pr-rich intergranular phase, which acts as a magnetic isolator for the hard grains [28], together with a ferromagnetic $(Pr,Nd)_2Fe_{14}B$ shell layer around the grains. This shell layer presents an anisotropy field slightly larger than that of $Nd_2Fe_{14}B$ (7.07 T), like that for pure $Pr_2Fe_{14}B$ is 7.93 T [36], which is much smaller than that from Dy (15.8 T) [36,37]. The reason for this shell layer, with just slightly higher anisotropy, to avoid the nucleation of reversed magnetic domains may be due to the formation of hard grain surfaces with few defects and homogeneous magnetocrystalline anisotropy during the infiltration, keeping high values of the nucleation field. Recent simulations evaluating the effect of the Nd content and the thickness of the grain boundary determined that the magnetisation and the exchange interactions decrease to zero with the increasing Nd content at the intergranular phase[38]. For that reason, the highest coercivity can be obtained only by the formation of a Nd-rich thin (1.5-2 nm) grain boundary phase. In our samples, the non-magnetic Pr(Nd)-Fe phase can be considered as a defect that might delay the domain wall motion at the same time that it decouples the hard grains.

3.3 Summary and conclusions

In this chapter, the results of two main studies looking for the reduction of rare earth, and primarily heavy rare earths, in Nd-Fe-B based alloys have been shown. These studies were based on the addition of doping elements for the control of the microstructure during crystallisation of Nd-lean Nd-Fe-B alloys and on the process of infiltration of a light RE eutectic alloy as well as its effect on microstructured Nd-Fe-B alloys with different amounts of Nd in their composition.

Regarding the crystallisation process of Nd-Fe-B alloys, it has been shown how the microstructure of as-spun ribbons can be controlled by the wheel speed allowing the obtaining of ribbons highly disordered (at high wheel speeds) or nanocrystalline ribbons (at low wheel speeds) that allows the reduction of the annealing temperature to obtain the desirable properties. As for the crystallisation process during heat treatments, all the alloys showed the formation of two magnetic phases; the 2:14:1 hard magnetic phase at temperatures in the range of 280-400 ºC, and the soft magnetic α-Fe phase at around 600 ºC. In this alloys, two different dopants have been used to control the grain growth during annealing; Nb and Cu. The doping of Nb shows an increase in the crystallisation temperatures which suggest an inhibition of grain growth due to the presence of this element. On the other hand, doping with Cu shifts to lower temperatures the onset of the hard phase crystallisation temperature, which suggests the helping on the nucleation process when this element is present. However, the early formation of 2:14:1 phase by heat treatment helps the crystallisation of the secondary α-Fe phase. We can conclude that the formation of the latter phase is also driven by doping and, furthermore, is detrimental to the exchange coupling in the nanostructured magnets studied.

About the GBDP, the infiltration of Pr_3(Co,Cu) in Nd-Fe-B alloys enhances the coercivity of microstructured ribbons almost five-fold from its initial value, reaching 2.5 T, comparable with the best values reached using Dy based alloys. Before infiltration, the ribbons were composed of two phases, hard $Nd_2Fe_{14}B$ nanocrystalline grains and α-Fe precipitates. Analysis of XRD and Mössbauer spectroscopy shows that the amount of α-Fe is greatly reduced after the infiltration. This fact, together with the lack of enhancement of the coercivity on the stoichiometric sample suggest an important role of this soft phase presence on the infiltration process. But this effect does not explain the coercivity enhancement in the

Nd-abundant sample, in which the amount of α-Fe at the beginning is even lower.

One of the infiltrated Nd-lean samples was analysed under high-resolution TEM to gain insight of the effect of the infiltration process on the microstructure of the sample. The images of EDS showed a Pr-rich Pr(Nd)-Fe intergranular phase and a gradient of composition within the grains, which can be described as a core-shell structure, with a pure $Nd_2Fe_{14}B$ core and a $(Pr,Nd)_2Fe_{14}B$ gradient layer at the surface. These core-shell hard grains are decoupled by the non-magnetic Pr(Nd)-Fe phase allocated in the boundaries. This intergranular phase might pin the domain wall hindering its motion, which together with the single domain $Nd_2Fe_{14}B$ nanograins with few defects and nucleation field similar to the hard phase, helps to increase the coercivity of the samples.

3.4 References

[1] M. Sagawa, K. Hiraga, H. Yamamoto, Y. Matsuura, Permanent magnet materials based on the rare earth-iron-boron tetragonal compounds (invited), IEEE Trans. Magn. 20 (1984) 1584–1589. doi:10.1109/TMAG.1984.1063214.

[2] R. Coehoorn, D.B.B. de Mooij, C. de Waard, Meltspun permanent magnet materials containing Fe3B as the main phase, J. Magn. Magn. Mater. 80 (1989) 101–104. doi:10.1016/0304-8853(89)90333-8.

[3] E.F. Kneller, R. Hawig, The exchange-spring magnet: A new material principle for permanent magnets, IEEE Trans. Magn. 27 (1991) 3588–3600. doi:10.1109/20.102931.

[4] T. Schrefl, H. Kronmüller, J. Fidler, Exchange hardening in nano-structured two-phase permanent magnets, J. Magn. Magn. Mater. 127 (1993) L273–L277. doi:10.1016/0304-8853(93)90042-Z.

[5] R. Skomski, J.M.D. Coey, Giant energy product in nanostructured two-phase magnets, Phys. Rev. B. 48 (1993) 15812–15816. doi:10.1103/PhysRevB.48.15812.

[6] L. Withanawasam, A.S. Murphy, G.C. Hadjipanayis, R.F. Krause, Nanocomposite R2Fe14B/Fe exchange coupled magnets, J. Appl. Phys. 76 (1994) 7065–7067. doi:10.1063/1.358028.

[7] L. Withanawasam, G.C. Hadjipanayis, R.F. Krause, Enhanced remanence in isotropic fe-rich melt-spun nd-fe-b ribbons, J. Appl. Phys. 75 (1994) 6646–6648. doi:10.1063/1.356882.

[8] A. Manaf, R.A.A. Buckley, H.A.A. Davies, New nanocrystalline high-remanence Nd-Fe-B alloys by rapid solidification, J. Magn. Magn. Mater. 128 (1993) 302–306. doi:10.1016/0304-8853(93)90475-H.

[9] K. O'Donnell, C. Kuhrt, J.M.D. Coey, Influence of nitrogen content on coercivity in remanence-enhanced mechanically alloyed Sm-Fe-N, J. Appl. Phys. 76 (1994) 7068–7070. doi:10.1063/1.358029.

[10] I.A. Al-Omari, D.J. Sellmyer, Magnetic properties of nanostructured CoSm/FeCo films, Phys. Rev. B. 52 (1995) 3441–3447. doi:10.1103/PhysRevB.52.3441.

[11] M. Dahlgren, R. Grossinger, E. de Morais, S. Gama, G. Mendoza, J.F. Liu, H.A. Davies, Enhancement of the Curie temperature for exchange coupled Nd-Fe-B and Pr-Fe-B magnets, IEEE Trans. Magn. 33 (1997) 3895–3897. doi:10.1109/20.619607.

[12] J.P. Liu, C.P. Luo, Y. Liu, D.J. Sellmyer, High energy products in rapidly annealed nanoscale Fe/Pt multilayers, Appl. Phys. Lett. 72 (1998) 483–485. doi:10.1063/1.120793.

[13] G.C. Hadjipanayis, L. Withanawasam, R.F. Krause, Nanocomposite R2Fe14B/α-Fe permanent magnets, IEEE Trans. Magn. 31 (1995) 3596–3601. doi:10.1109/20.489581.

[14] H. Zeng, J. Li, J.P. Liu, Z.L. Wang, S. Sun, Exchange-coupled nanocomposite magnets by nanoparticle self-assembly, Nature. 420 (2002) 395–398. doi:10.1038/nature01208.

[15] M. Yue, Y. Li, Q. Wu, W. Liu, Bulk Nanostructural Permanent Magnetic Materials, Rev. Nanosci. Nanotechnol. 3 (2014) 276–288. doi:10.1166/rnn.2014.1057.

[16] Y. Sen, L. Shandong, L. Xiansong, S. Xiaoping, G. Benxi, D. Youwei, Exchange coupled Nd2Fe14B/α-Fe nanocomposite magnets with fine α-Fe grains obtained by low wheel speed spinning, J. Alloys Compd. 343 (2002) 217–222. doi:10.1016/S0925-8388(02)00137-8.

[17] K. Men, K. Li, Y. Luo, D. Yu, K. Zhang, J. Jin, Y. Mao, The crystallization behavior of as-quenched Nd9Fe85Nb0.5B5.5 alloys, J. Alloys Compd. 635 (2015) 61–65. doi:10.1016/J.JALLCOM.2015.02.046.

[18] W. Zhou, C. Chang, A. Inoue, X. Wang, F. Li, J. Huo, Direct production of hard magnetic ribbons with enhanced magnetic properties by controlling cooling rate of melt, J. Appl. Phys. 117 (2015) 123905. doi:10.1063/1.4915280.

[19] S. David, D. Givord, Coercivity in lean rare earth NdFeB and PrFeB nanocomposite hard magnetic materials, J. Alloys

Compd. 281 (1998) 6–11. doi:10.1016/S0925-8388(98)00761-0.

[20] R. Zhang, Y. Liu, J. Ye, W. Yang, Y. Ma, S. Gao, Effect of Nb substitution on the temperature characteristics and microstructures of rapid-quenched NdFeB alloy, J. Alloys Compd. 427 (2007) 78–81. doi:10.1016/J.JALLCOM.2006.03.034.

[21] Y.Q. Wu, D.H. Ping, K. Hono, M. Hamano, A. Inoue, Microstructural characterization of an α-Fe/Nd2Fe14B nanocomposite magnet with a remaining amorphous phase, J. Appl. Phys. 87 (2000) 8658. doi:10.1063/1.373593.

[22] S. Constantinides, The Important Role of Dysprosium in Modern Permanent Magnets, Arnold Magn. Technol. (2012) 1–8. http://www.arnoldmagnetics.com/wp-content/uploads/2017/10/Important-Role-of-Dysprosium-in-Modern-Permanent-Magnets-150906.pdf (accessed August 7, 2018).

[23] S. Sawatzki, C. Kübel, S. Ener, O. Gutfleisch, Grain boundary diffusion in nanocrystalline Nd-Fe-B permanent magnets with low-melting eutectics, Acta Mater. 115 (2016) 354–363. doi:10.1016/j.actamat.2016.05.048.

[24] H. Sepehri-Amin, T. Ohkubo, The mechanism of coercivity enhancement by the grain boundary diffusion process of NdFeB sintered magnets, Acta Mater. 61 (2013) 1–9. doi:10.1016/j.actamat.2012.12.018.

[25] T. Zhang, F. Chen, Y. Zheng, H. Wen, L. Zhang, L. Zhou, Anisotropic behavior of grain boundary diffusion in hot-deformed Nd-Fe-B magnet, Scr. Mater. 129 (2017) 1–5. doi:10.1016/j.scriptamat.2016.10.017.

[26] C.C. Pavel, R. Lacal-Arántegui, A. Marmier, D. Schüler, E. Tzimas, M. Buchert, W. Jenseit, D. Blagoeva, Substitution strategies for reducing the use of rare earths in wind turbines, Resour. Policy. 52 (2017) 349–357. doi:10.1016/j.resourpol.2017.04.010.

[27] Z. Lin, J. Han, M. Xing, S. Liu, R. Wu, C. Wang, Y. Zhang, Y. Yang, J. Yang, Improvement of coercivity and thermal stability

of anisotropic Nd13Fe79.4B7Nb0.3Ga0.3powders by diffusion of Pr-Cu alloys, Appl. Phys. Lett. 100 (2012) 052409. doi:10.1063/1.3681803.

[28] H. Sepehri-Amin, L. Liu, T. Ohkubo, M. Yano, T. Shoji, A. Kato, T. Schrefl, K. Hono, Microstructure and temperature dependent of coercivity of hot-deformed Nd-Fe-B magnets diffusion processed with Pr-Cu alloy, Acta Mater. 99 (2015) 297–306. doi:10.1016/j.actamat.2015.08.013.

[29] L. Li, A. Tirado, B.S. Conner, M. Chi, A.M. Elliott, O. Rios, H. Zhou, M.P. Paranthaman, A novel method combining additive manufacturing and alloy infiltration for NdFeB bonded magnet fabrication, J. Magn. Magn. Mater. 438 (2017) 163–167. doi:10.1016/j.jmmm.2017.04.066.

[30] D. Salazar, A. Martín-Cid, R. Madugundo, J.S. Garitaonandia, J.M. Barandiaran, G.C. Hadjipanayis, Effect of Nb and Cu on the crystallization behavior of under-stoichiometric Nd-Fe-B alloys, J. Phys. D. Appl. Phys. 50 (2017) 015305. doi:10.1088/1361-6463/50/1/015305.

[31] D. Salazar, A. Martín-Cid, R. Madugundo, J.M. Barandiaran, G.C. Hadjipanayis, Coercivity enhancement in heavy rare earth-free NdFeB magnets by grain boundary diffusion process, Appl. Phys. Lett. 113 (2018) 152402. doi:10.1063/1.5043389.

[32] A.H. Morrish, The Physical Principles of Magnetism, IEEE Press, 1965. doi:10.1002/9780470546581.

[33] E. Girt, K.M. Krishnan, G. Thomas, E. Girt, Z. Altounian, Coercivity limits and mechanism in nanocomposite Nd–Fe–B alloys, J. Magn. Magn. Mater. 231 (2001) 219–230. doi:10.1016/S0304-8853(01)00031-2.

[34] J. Bauer, M. Seeger, A. Zern, H. Kronmüller, Nanocrystalline FeNdB permanent magnets with enhanced remanence, J. Appl. Phys. 80 (1996) 1667–1673. doi:10.1063/1.362965.

[35] L. Liu, H. Sepehri-Amin, T. Ohkubo, M. Yano, A. Kato, N. Sakuma, T. Shoji, K. Hono, Coercivity enhancement of hot-deformed Nd-Fe-B magnets by the eutectic grain boundary diffusion process using Nd62Dy20Al18 alloy, Scr. Mater. 129

(2017) 44–47. doi:10.1016/j.scriptamat.2016.10.020.

[36] E.B. Boltich, E. Oswald, M.Q. Huang, S. Hirosawa, W.E. Wallace, E. Burzo, Magnetic characteristics of R2Fe14B systems prepared with high purity rare earths (R=Ce, Pr, Dy, and Er), J. Appl. Phys. 57 (1985) 4106–4108. doi:10.1063/1.334633.

[37] J.F. Herbst, W.B. Yelon, Crystal and magnetic structure of Pr2Fe14B and Dy2Fe14B, J. Appl. Phys. 57 (1985) 2343–2345. doi:10.1063/1.334342.

[38] J. Fischbacher, A. Kovacs, M. Gusenbauer, H. Oezelt, L. Exl, S. Bance, T. Schrefl, Micromagnetics of rare-earth efficient permanent magnets, J. Phys. D. Appl. Phys. 51 (2018) 193002. doi:10.1088/1361-6463/aab7d1.

4 New Rare earth lean magnets

4.1 Introduction

As has been previously mentioned in chapter 1, the compounds based on the $ThMn_{12}$ tetragonal structure, referred as 1:12 from now on, are good candidates for permanent magnets. This structure, shown in Figure 4.1, has the space group I4/mmm where two Th atoms occupy the 2a site while twenty-four atoms of Mn are evenly distributed between the 8*i*, 8*j* and 8*f* sites [1].

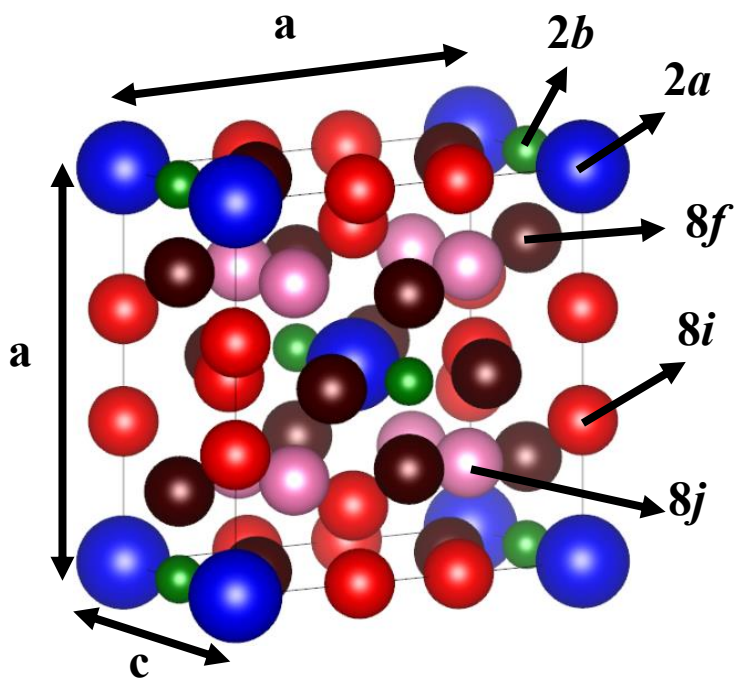

Figure 4.1- Schematic representation of the ThMn12 type of structure.

The ideal compound with this structure and with good properties for permanent magnet applications would be RFe_{12}, being R a rare earth, but this kind of compounds is not stable and a third non-magnetic element is needed in order to stabilise the 1:12 structure, obtaining a ternary compound of the $R(Fe,M)_{12}$ type. The most common elements used to stabilise this structure are the transition metals (M = Ti, Mo, Nb, V), which have a preference to substitute the iron on the 8*i* sites, characterised by the largest Wigner-Seitz cell and hyperfine field. Another possibility to

stabilise the 1:12 structure is the use of sp elements (M = Si, Al) that have a preference for the 8*f* site and allows for a greater saturation magnetisation with higher amounts of the M element [2–4]. Recently, it has been shown that the substitution of R for Zr can help with the stabilisation of the 1:12 structure as a consequence of the reduction of the average radius of the atoms in the 2a site, even at the full substitution $Zr(Fe,M)_{12}$ [5,6].

Other elements can be added to these compounds in order to improve their properties or reduce their criticality reducing the amount of R. For example, the addition of Co can lead to an increase of the Curie temperature as well as the saturation polarisation and the anisotropy constant in some alloys [7–12]. In the case of the substitution of R, aside of the already mentioned Zr, Ce has attracted particular attention due to its relative abundance and low cost compared with other rare earths and in spite of its mixed-valence behaviour, which leads to a decreased Curie temperature and lower saturation magnetisation and anisotropy [7,13–17].

These compounds with the 1:12 structure are characterised by a negative value of the crystal field parameter (A_2^0) and they present the strongest uniaxial magnetocrystalline anisotropy for the rare earths R with a positive Stevens coefficient (ϑ_2). In this way, Sm compounds shows the greatest uniaxial anisotropy, while the use of Nd or Ce leads to magnetocrystalline anisotropy that is not completely uniaxial [18]. The modification of the crystal lattice with interstitial nitrogen (which is allocated in the 2b site shown in Figure 4.1) reverses the sign of the A_2^0 parameter, therefore it favours the uniaxial magnetocrystalline anisotropy in compounds with ϑ_2 negative (i.e. Nd, Pr, Ce) while it makes it planar in compounds with ϑ_2 positive as Sm. This interstitial modified compounds present an enhanced Curie temperature and can show an increase of the saturation magnetisation [19–21].

The results shown in this chapter are divided in two sections depending on the non-magnetic element used to stabilise the 1:12 structure, Ti or Si. The intrinsic properties of each alloy are studied to evaluate their stability and capability as candidates for permanent magnet applications. The most promising alloys are then selected to develop coercivity.

4.2 Ti stabilised 1:12 alloys

In this section I report the results obtained synthesising two families of compounds; (Ce,Sm)Fe_9Co_2Ti and (Nd,Y)$Fe_{11}Ti$, both of them stabilised in the 1:12 structure with Ti. The advantage of using Ti as stabilising element is that just 1 atom per formula unit is needed, minimizing the effect of the substitution of Fe and thus obtaining better magnetic properties compared with other stabilising elements [2].

For the first compound, a series of compositions $Ce_{1-x}Sm_xFe_9Co_2Ti$ (x = 0, 0.25, 0.5, 0.75 and 1) were prepared by arc-melting the pure constituents with a purity better than 99.7 at.% and annealing at 1100 ºC for 48 hours to stabilise the 1:12 structure. The samples with Sm had to be charged with 18-20 weight-% excess of this element to compensate the evaporation loses during the melting process [16,17]. To fabricate ribbons, these alloys were subsequently melt-spun at a wheel speed of 35 m/s and heat treated in order to tune the microstructure to develop coercivity.

Recent theoretical predictions (H.C. Herper, personal communication, September 30, 2017) indicate that substituting Y for Nd in $Nd_{1-x}Y_xFe_{11}Ti$ will greatly improve the magnetic anisotropy. In collaboration with Onur Tosun, from the University of Delaware, the $Nd_{0.5}Y_{0.5}Fe_{11}Ti$ alloy was prepared by arc-melting the pure constituents with a purity better than 99.7 at.% and annealed at 1175 ºC for 3 days to stabilise the 1:12 structure. Afterwards, this compound was ground under 45 µm and nitrogenated to improve its magnetic properties. In addition, melt-spun ribbons were made from the as-cast alloy at 35 m/s and annealed at 850 ºC for 4 hours to obtain the 1:12 structure for its posterior nitrogenation following the same procedure as with the bulk samples.

4.2.1 (Ce,Sm)Fe_9Co_2Ti

4.2.1.1 Intrinsic properties

Figure 4.2 shows the X-ray diffractograms of the $Ce_{0.5}Sm_{0.5}Fe_9Co_2Ti$ alloy randomly and field oriented. From this diffractograms can be seen that the alloy is composed of two phases, the 1:12 and the cubic α-Fe(Co,Ti). The amount of this secondary phase was determined by Mössbauer spectroscopy to be below 5% of the total in all cases. The

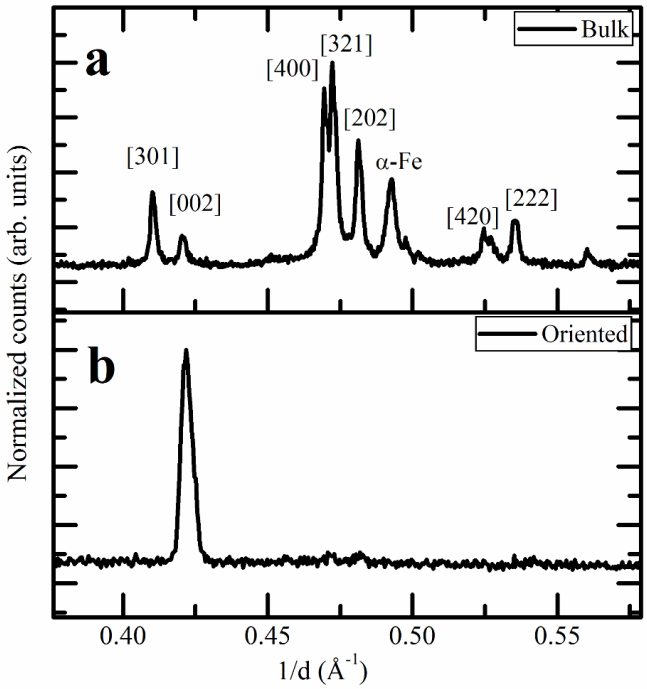

Figure 4.2- XRD patterns for random oriented microcrystalline powder (a) and field-oriented microcrystalline powder (b) with composition $Ce_{0.5}Sm_{0.5}Fe_9Co_2Ti$.

lattice parameters for all the Sm substitution are summarised in Table 4.1. The lattice parameter a remains constant through all the compositions while parameter *c* is slightly reduced by a 0.3% from the pure Ce (x = 0) to the pure Sm (x = 1) alloy. The diffractogram of the oriented powders shows only the [002] plane reflection, which indicates the existence of a uniaxial magnetocrystalline anisotropy in the c-axis direction.

In Figure 4.3 are shown the magnetisation measurements performed to field oriented powders along the parallel and perpendicular direction to the c-axis. The saturation magnetisation obtained from this measurements, using the law of approach to saturation, is ~115 Am^2/kg, without significant variations with the amount of Sm. On the other hand, the anisotropy field increases from 2.6 T for x = 0 up to 8.6 T for x = 1. It is possible to see also that this anisotropy field remains constant for x = 0 and x = 0.25, while it increases linearly for higher concentrations of Sm. The Curie temperature also increases with the substitution of Ce by Sm, increasing from 382 ºC for x = 0 up to 489 ºC for x = 1. All the intrinsic properties are summarised in Table 4.1

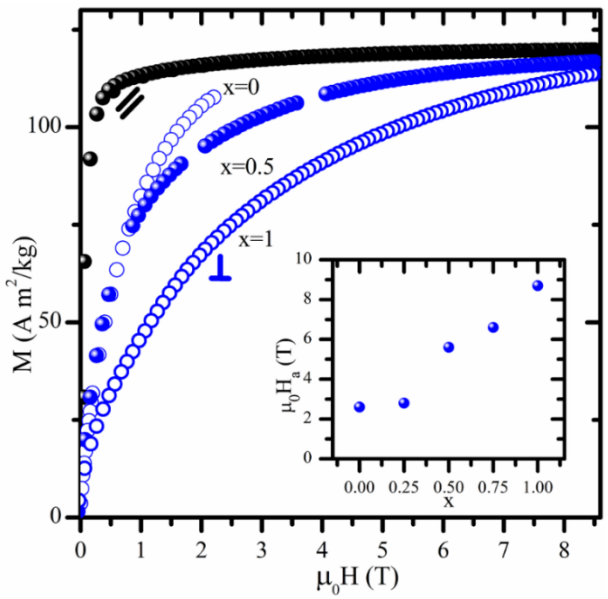

Figure 4.3- Magnetisation curves of field-oriented powders for different compositions of $Ce_{1-x}Sm_xFe_9Co_2Ti$ alloys parallel (black) and perpendicular (blue) to the easy axis of magnetisation. Inset: evolution of the anisotropy field with the concentration of Sm

Table 4.1- Summary of magnetic properties for $Ce_{1-x}Sm_xFe9Co2Ti$.

x	M_s (Am^2/kg)	μ_0H_a (T)	T_c (ºC)	Lattice parameters	
				a **(Å)**	***c*** **(Å)**
0.00	127	2.6	382	8.527	4.797
0.25	113	2.8	417	8.505	4.791
0.50	117	5.6	453	8.499	4.799
0.75	128	6.6	489	8.520	4.785
1.00	112	8.7	489	8.517	4.779

4.2.1.2 Melt-spun ribbons

As-spun ribbons of these alloys present a highly disordered 1:12 phase to which are related the broad reflections shown in Figure 4.4.a. These as-spun ribbons present very low coercivity, always below 0.02 T for all compositions, as can be seen in Figure 4.5 for x = 0.5. After optimal heat treatments, the XRD patterns of Figure 4.4.b shows a sharp peak around $2\theta = 45º$ for x = 0.5, which corresponds to the [110] reflection of a cubic

α-Fe(Co,Ti) that is formed during the annealing. At the same time, the reflections of the 1:12 phase get sharper, suggesting the growth of crystals with this structure.

The inset of Figure 4.5 shows the evolution of the coercivity obtained for $Ce_{0.5}Sm_{0.5}Fe_9Co_2Ti$ heat-treated at different times and temperatures. This evolution is related to the growth of crystals with the 1:12 structure. The coercivity initially increases but, after reaching a maximum, it decreases. This behaviour can be due to a mixture of two effects, the growth of the 1:12 crystals above the single-domain critical size of 100-200 nm [22–25] and the formation of un-coupled α-Fe grains, evidenced by the two-step demagnetisation process in the hysteresis loops. The crystalline grains of this samples were estimated to be ~35-60 nm from XRD analysis.

The optimal heat treatment for each sample, summarised in Table 4.2 together with the coercivity reached in each case, is considered for the highest coercivity reached without presenting a step-like hysteresis loop.

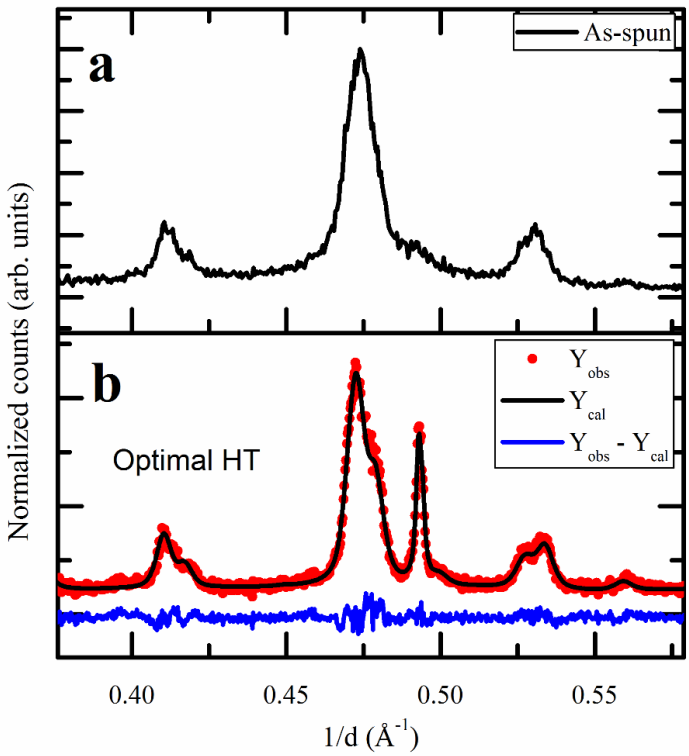

Figure 4.4- XRD patterns for as-melt-spun ribbons (c) and Rietveld refinement of optimally heat treated ribbons (d) with composition $Ce_{0.5}Sm_{0.5}Fe_9Co_2Ti$.

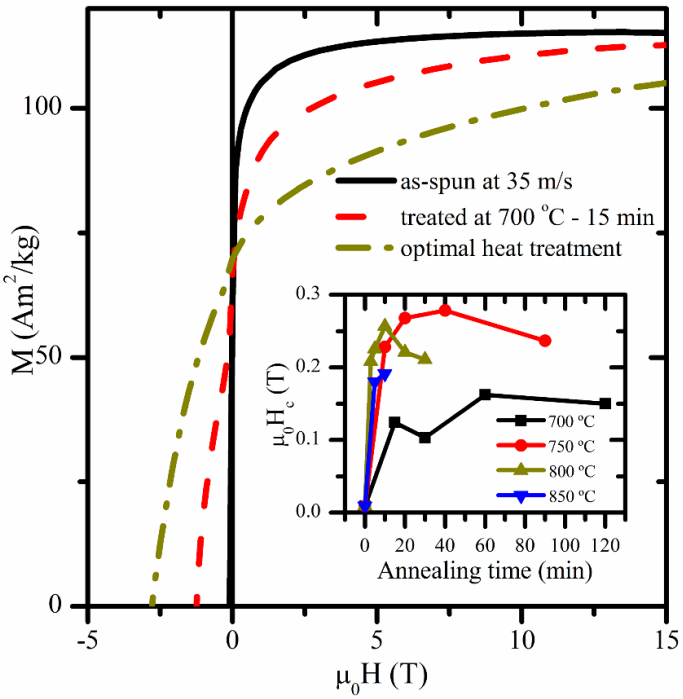

Figure 4.5- Magnetisation curves for as-spun and heat treated ribbons with composition $Ce_{0.5}Sm_{0.5}Fe_9Co_2Ti$. Inset: evolution of the coercivity for different annealing times and temperatures

Table 4.2- Summary of magnetic properties and optimal heat treatments for $Ce_{1-x}Sm_xFe_9Co_2Ti$ ribbons. μ_0H_a values are obtained from microcrystalline powdered samples

x	Optimal treatment (ºC-min)	M_s (Am^2/kg)	μ_0H_a (T)	μ_0H_c (T)	T_c (ºC)
0.00	800-3	127	2.6	0.08	382
0.25	800-5	113	2.8	0.12	417
0.50	750-40	117	5.6	0.26	453
0.75	800-10	128	6.6	0.37	489
1.00	850-10	113	8.7	0.44	489

Figure 4.6 a and b show the Mössbauer spectra obtained at RT of the as-spun and heat treated $SmFe_9Co_2Ti$ ribbons. The as-spun spectrum presents wider lines than the crystallised one. Such a broadening is due to chemical and structural disorder. For the heat-treated ribbons spectrum,

the black circles correspond to the experimental data, the coloured lines to the contribution of each environment, 8*i*, 8*j* and 8*f* from the ThMn12 phase and one site from the α-Fe. Each site from the ThMn12 phase corresponds to the sum of three environments. The black line is the superposition of all the sextets of each environment. The resonant area of the α-Fe phase (purple thicker curve) is much smaller than that of the $ThMn_{12}$ phase, which indicates a low amount of free α-Fe in the sample, under 5%.

The parameters obtained from the Mössbauer spectra of the optimally heat treated ribbons are summarised in Table 4.3. The Fe content for each site obtained from the value of the resonant areas allows deducing the occupation of Co atoms for each site. For concentrations of Sm below x = 0.5, the Co is evenly distributed between the 8*j* and the 8*f* sites, while for concentrations above x = 0.5 there is a preference for Co to locate in the 8*j* site, having a distribution of 70% in the 8*j* site and 30% in the 8*f*.

The redistribution of Co between 8*j* and 8*f* sites can be seen when comparing the fitted sub-spectra of these sites for the compositions with x = 1 and x = 0. As seen in Figure 4.6 c and d, the area of the 8*j* site is larger for x = 0 while the area of the 8*f* site is smaller for x = 0. Along with the change of the area, there is also a change in the shape due to the different environments. This is in agreement with the decrease of the hyperfine field in the 8*j* site while the hyperfine field of 8*f* site increases. The isomer shift also shows a clear change for concentrations below x = 0.5.

Table 4.3- Mössbauer parameters for $Ce_{1-x}Sm_xFe_9Co_2Ti$ heat treated ribbons, IS: isomer shift, Bhf: hyperfine field, QS: quadrupole splitting and the resonant area. nCo corresponds to the Co occupation.

x	Site	<IS> (mm/s)	<Bhf> (T)	<QS> (mm/s)	<AREA> (%)	nCo
0.00	8*i*	-0.18	28.3	-0.02	36.4	0.0
	8*j*	-0.12	25.4	0.03	31.2	0.9
	8*f*	-0.15	26.7	0.10	28.3	1.1
	α-Fe	0.00	33.0	0.00	4.2	
0.25	8*i*	-0.19	28.8	0.02	35.3	0.0
	8*j*	-0.11	26.1	0.05	30.0	1.0
	8*f*	-0.17	27.0	0.10	29.8	1.0
	α-Fe	0.00	33.0	0.00	4.8	
0.50	8*i*	-0.14	30.7	0.07	31.3	0.0
	8*j*	-0.10	29.4	-0.03	28.2	1.4
	8*f*	-0.20	26.4	0.09	36.0	0.6
	α-Fe	0.00	33.0	0.00	4.4	
0.75	8*i*	-0.12	30.4	0.09	34.2	0.0
	8*j*	-0.11	28.8	-0.10	27.7	1.4
	8*f*	-0.19	26.4	0.09	36.2	0.6
	α-Fe	0.00	33.0	0.00	1.8	
1.00	8*i*	-0.12	30.5	0.07	34.3	0.0
	8*j*	-0.15	28.6	0.09	26.6	1.5
	8*f*	-0.16	26.4	0.08	36.1	0.5
	α-Fe	0.00	33.0	0.00	3.1	

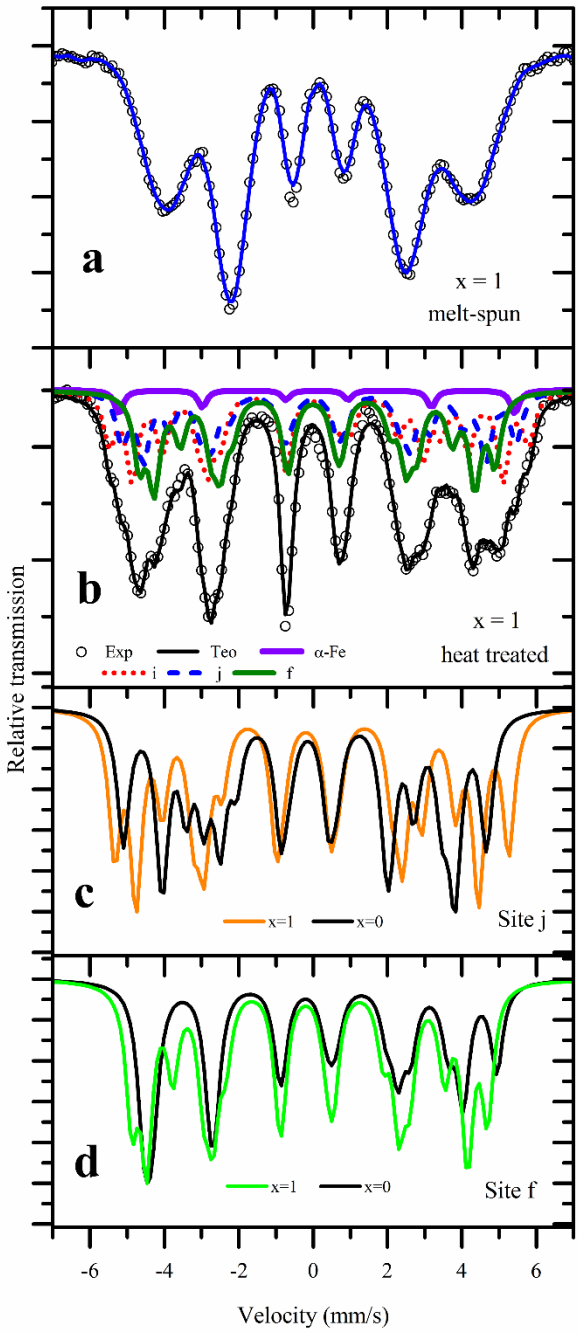

Figure 4.6- Mössbauer spectra of as-spun (a) and optimally heat treated ribbons with the fitted sub-spectra (b) for the $SmFe_9Co_2Ti$ alloy. Comparison of the fitting of sites j (c) and f (d) for the compositions with x = 0 and x = 1.

4.2.2 $(Nd,Y)Fe_{11}TiN_x$

4.2.2.1 Intrinsic properties

The alloy with Y substitution was confirmed to have a greater anisotropy field as predicted, going from 1 T of the pure Nd alloy to 1.75 T for a substitution of 50% of the Nd by Y as evidenced in Figure 4.7. Together with this increment of the anisotropy field, the saturation magnetisation is slightly reduced from 130 Am^2kg^{-1} to 127 Am^2kg^{-1} and the Curie temperature was diminished from 300 ºC down to 270 ºC.

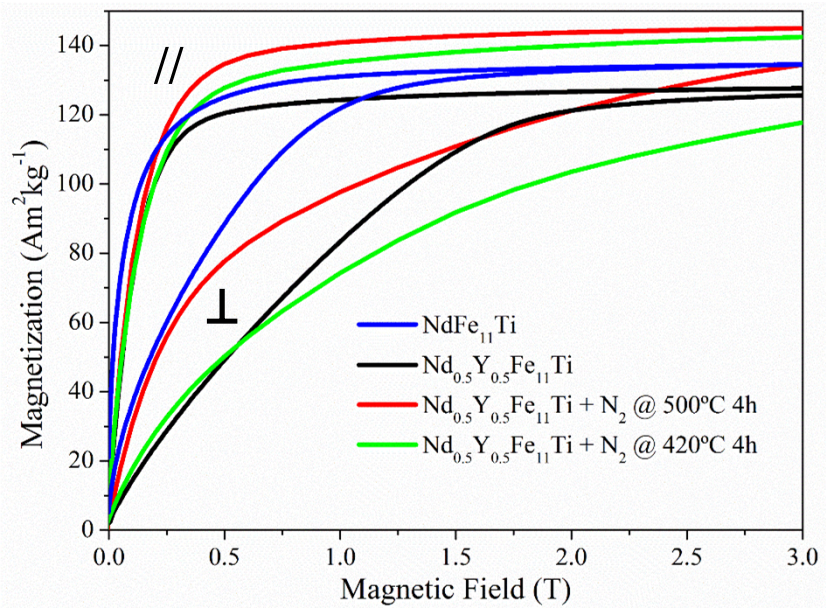

Figure 4.7- Room-temperature isotherms for field-oriented powders in parallel (//) and perpendicular (⊥) directions

In order to further improve the magnetic properties of this newly synthesised alloy, several nitrogenation processes were carried out at different temperatures. In Figure 4.7 is possible to see the enhancement of the anisotropy field of the sample before and after nitrogenation, increasing up to over 5 T. The magnetisation curves of two different nitrogenation processes show the effect on the sample of an excessive temperature during the process. The best process parameters found were 4h at 420 ºC with a nitrogen pressure of 1 bar. The increase of the saturation magnetisation can be mostly attributed to the free α-Fe phase formation during the process as can be verified from the increase in the intensity of the [110] reflection on the XRD pattern shown in Figure 4.8.

From this XRD patterns is possible also to see how the reflections corresponding with the 1:12 structure are shifted to lower 2θ angles, suggesting an expansion of the lattice parameters as was expected for an interstitially modified 1:12 compound [26]. As above, Figure 4.8 also shows the XRD pattern of a sample nitrogenated at a too high temperature (500 ºC). From this diffractogram is possible to see how while the 1:12 structure still exists with similar lattice parameters as the best nitrogenated one, a huge reflection appears around 2θ = 45º. At first, this reflections could be assigned to a cubic α-Fe as there are no other new reflections appearing, but the broadness can suggest that a new phase is formed which has only one reflection seen in the scanned 2θ range and overlapping with the α-Fe one.

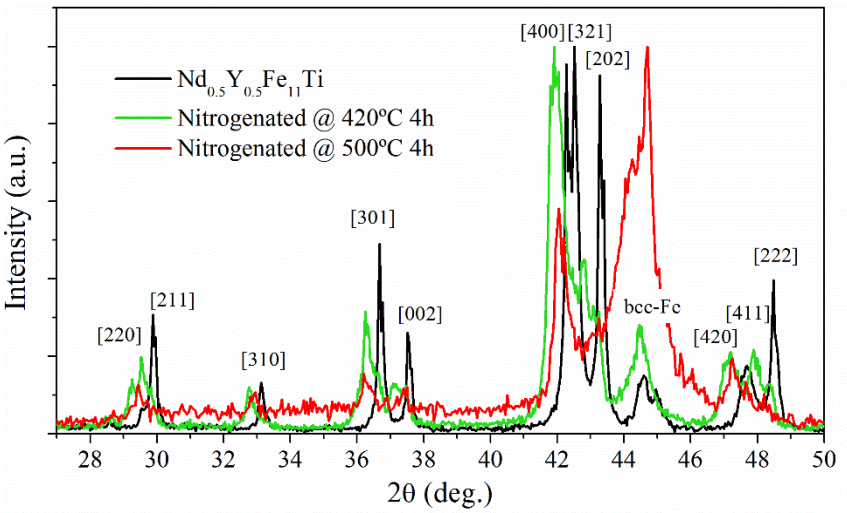

Figure 4.8- X-ray diffractograms the $Nd_{0.5}Y_{0.5}Fe_{11}Ti$ alloy before and after the nitrogenation process.

From the thermogravimetric analysis curve under magnetic field shown in Figure 4.9, it is possible to see that the Curie temperature of the nitrogenated samples is enhanced after the process reaching a value of 390 ºC. The broad peak, corresponding with the Curie temperature of these samples, suggests that there is a gradient of nitrogen concentration on the sample, which can be due to different grain sizes needing different time to become fully nitrogenated. This effect can be also seen comparing the width of the XRD reflections of the nitrogenated sample with the parent sample.

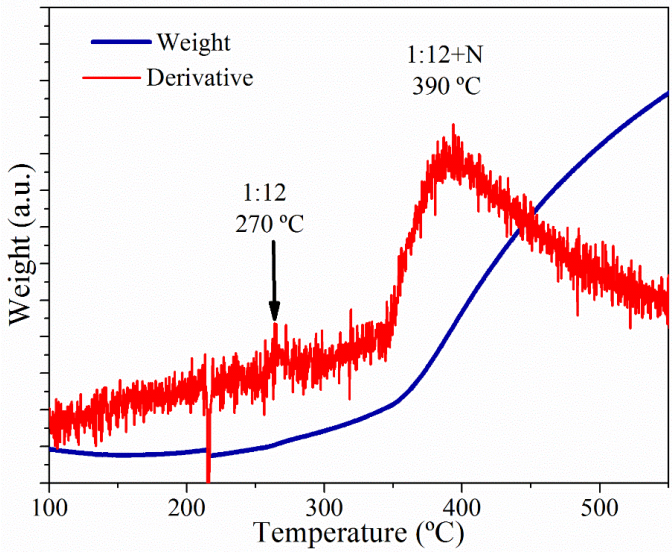

Figure 4.9- Thermo-magnetic curve of a nitrogenated sample.

4.2.2.2 Melt-spun ribbons

After the successful improvement of the magnetic properties of this alloy upon nitrogenation, a preliminary study was done on the nitrogenation of melt-spun ribbons.

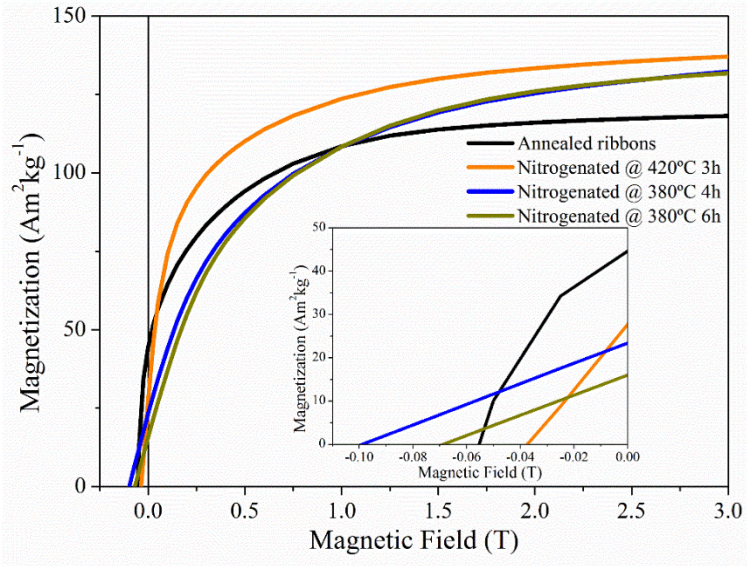

Figure 4.10- Magnetisation curves of ribbons. Inset: Detail of the coercive field.

As can be seen from the hysteresis loops shown in Figure 4.10, the crystalline ribbons with the 1:12 phase present quite a low coercivity of just 0.055 T. Trying to nitrogenate them with similar parameters as the bulk sample, a reduction on the coercivity was found, reaching just ~0.04 T. A reduction of the temperature of the process was done in order to get a better nitrogenated sample. The best sample obtained, after 6 hours at 380 ºC in a pressure of 1 bar of nitrogen, presented an enhancement of an 80% of the coercivity, reaching a value of 0.1 T. In all the nitrogenated samples the saturation magnetisation was increased, which indicates the formation of α-Fe during the process as confirmed by XRD (Figure 4.11).

From the XRD patterns shown in Figure 4.11 is possible to see again the shift of the reflections corresponding to the 1:12 structure to lower 2θ angles, indicating the expansion of the lattice parameters. Together with this displacement, a broadening of the reflections indicates either that the sample loses part of the crystallinity or that there is a gradient on the nitrogenation of the structure. The huge increase of the intensity for the α-Fe reflection confirms that the reduction on the coercivity for the sample nitrogenated at 420 ºC was due to the formation of this soft phase. In the best-obtained sample is possible to see also a big increment of the α-Fe phase, which suggests that better nitrogenation parameters can be achieved for these samples, which could lead to a better enhancement of the coercivity.

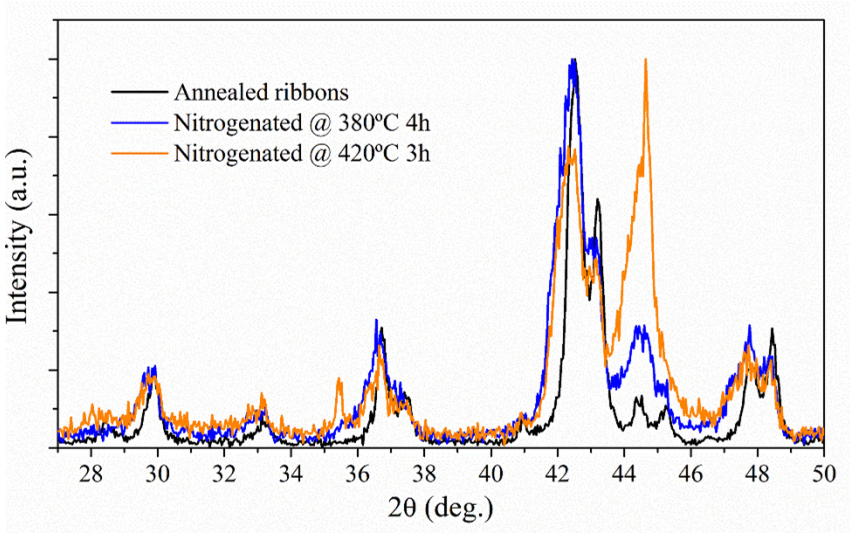

Figure 4.11- X-ray diffractograms of the ribbons before and after the nitrogenation process.

A summary of the properties obtained for this samples in bulk and ribbons are shown in Table 4.4.

*Table 4.4- Summary of the properties of the $Nd_{1-x}Y_xFe_{11}Ti + N_2$ system (Nitrogenation parameters: T = 420 ºC, P = 1 bar, Powder size <45 µm, t = 4 hours). * This value is affected by the α-Fe present at the sample*

Sample	Ms (Am^2kg^{-1})	μ_0H_a (T)	Tc (ºC)	μ_0H_c (T)
$NdFe_{11}Ti$	~130	~1	300	-
$Nd_{0.5}Y_{0.5}Fe_{11}Ti$	~127	~1.75	270	~0.055
$Nd_{0.5}Y_{0.5}Fe_{11}Ti + N_2$	~142*	>3	390	~0.1

4.3 Si stabilised 1:12 alloys

In this section, I report the results obtained for two families of compounds that have been stabilised in the 1:12 structure substitution Fe by Si; $(Zr,Ce)_{1.1}Fe_{10}Si_2$ and $(Zr,Nd)Fe_{10}Si_2$. In these samples, two atoms of Si are used to stabilise the structure as it yields better properties than other substitutions [27,28].

For the first compound, a series of compositions $(Zr_{1-x}Ce_x)_{1.1}Fe_{10}Si_2$ (x = 0, 0.3 and 0.6) were prepared by arc-melting the pure constituents with a purity better than 99.7 at.%. One advantage of these samples is that they crystallise directly in the 1:12 structure from the melt. Anyway, they were annealed at 1000 ºC for 24 hours in order to ensure the homogeneity.

Regarding the $Zr_{1-x}Nd_xFe_{10}Si_2$ compounds, following the research of M. Gjoka et al. [18], a single composition was used to attempt to nitrogenate; $Nd_{0.6}Zr_{.04}Fe_{10}Si_2$. This sample was prepared by arc-melting the pure constituents with a purity better than 99.9 at.%, obtaining an alloy with over 95% of the 1:12 without needing further annealing. This alloy was ball milled to obtain powder with a grain size of ~10 µm for nitrogenation. At the time this research was started (January 2017), no report was available about the nitrogenation of the 1:12 compounds stabilised with Si. Thus, the nitrogenation attempts on this sample were performed at high pressures of nitrogen to see if this parameter has an effect on the process. Soon after, a patent was granted related to the nitrogenation of Ce-Fe-Si compounds at high N_2 pressures [29].

4.3.1 Intrinsic properties of $Zr_{1-x}Ce_xFe_{10}Si_2$

From the magnetisation curves shown in Figure 4.12 is possible to see that the saturation magnetisation of the alloys, calculated by the law of approach to saturation from magnetisation curves of the parallel oriented powders, remains constant with the addition of Ce at a value of ~120 Am^2kg^{-1}. On the other hand, the anisotropy field is enhanced as the concentration of Ce increases from 2.03 T for x = 0 up to 2.5 T for x = 0.6. The anisotropy constants K_1 and K_2 were calculated from the magnetisation curves perpendicular to the easy axis of magnetisation by the equation $HM_s = 2K_1\left(\frac{M}{M_s}\right) + 4K_2\left(\frac{M}{M_s}\right)^3$, where M is the magnetisation at H applied field. The values of K_1 remained constant for all compounds at a value of 0.51±0.02 $MJ{\cdot}m^{-3}$ while the K_2 parameter increased from 0.24 $MJ{\cdot}m^{-3}$ for x = 0, to 0.38 $MJ{\cdot}m^{-3}$ for x = 0.3 and up to 0.42 $MJ{\cdot}m^{-3}$ for x = 0.6.

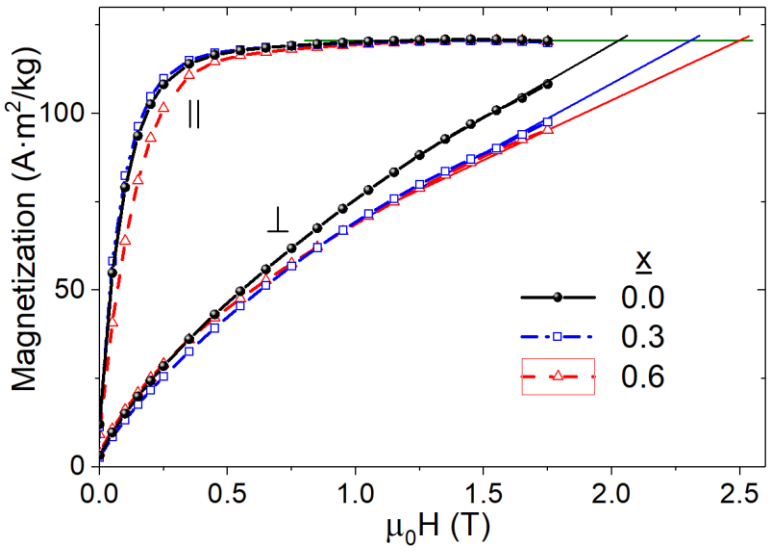

Figure 4.12- RT isotherms for field-oriented powders in parallel (||) and perpendicular (⊥) directions to the easy axis of magnetisation.

The XRD patterns shown in Figure 4.13 show that the samples present a pure 1:12 phase. With the addition of Ce to the alloy, the reflections of this phase are shifted to lower 2θ angles, which indicates an expansion of the lattice due to the presence of Ce. Table 4.5 shows a summary of the magnetic and structural parameters of each sample. From the values calculated by Rietveld analysis, the lattice parameter *a* increases twice as

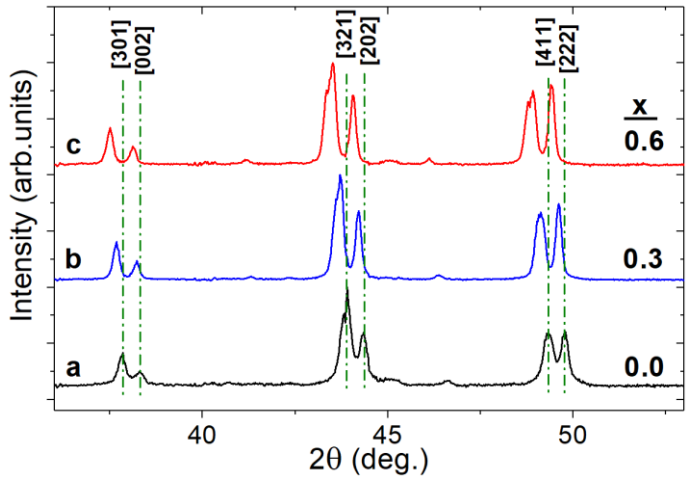

Figure 4.13- XRD at RT for (a) $Zr_{1.1}Fe_{10}Si_2$, (b) $(Zr_{0.7}Ce_{0.3})_{1.1}Fe_{10}Si_2$ and (c) $(Zr_{0.4}Ce_{0.6})_{1.1}Fe_{10}Si_2$ samples

much as the lattice parameter *c*, 1% vs. 0.5%, which results in an increase of the tetragonal distortion of the structure (a/c ratio) of about 0.5%, which can be related to the 25% increase of the anisotropy.

Table 4.5- Summary of magnetic and structural parameters of $(Zr_{1-x}Ce_x)_{1.1}Fe_{10}Si_2$ at RT: M_s: saturation magnetisation, H_a: anisotropy field, a,c: lattice parameters

Ce content	M_s ($A \cdot m^2\ kg^{-1}$)	$\mu_0 H_a$ (T)	*a* (Å)	*c* (Å)	*a*/*c*
x = 0.0	120	2.03	8.274	4.701	1.760
x = 0.3	120	2.31	8.303	4.707	1.764
x = 0.6	120	2.50	8.354	4.724	1.768

Normally, the introduction of a third element on this kind of alloys alter the neighbours of the Fe atoms in the structure, resulting in a complex mix of Mössbauer subspectra. In this case, the analysis of the spectra shown in Figure 4.18.a shows the evolution with temperature of the [301] and [002] reflections, which are closely related with the lattice parameters *a* and *c* respectively. While the [301] reflection shifts linearly with temperature, the [002] reflection displacement is more complex. In order to study the evolution of the lattice parameters with temperature, a sequential refinement of the NDP patterns was done with the FullProf suite. The values of the *a* and *c* lattice parameters obtained by this refinement are shown in Figure 4.18.b and Figure 4.18.c respectively. The lattice

parameter *a* presents a linear behaviour in agreement with can be carried out assuming wider sextets for each Fe position, as Si atoms do not induce large changes in the hyperfine field values. The results of this analysis are summarised in Table 4.6. In order to obtain an optimal fitting, a paramagnetic phase should be considered, having a contribution below 2% for all samples and with different hyperfine parameters. As the amount of these paramagnetic phases is too low, their hyperfine parameters are but a rough estimation, but still we can assign it to traces of the cubic $Zr_6Fe_{16}Si_7$ structure, which has been observed to coexist with $Zr_{1.1}Fe_{10}Si_2$, or to the $CeFe_2Si_2$ for the $Zr_{1.1}Fe_{10}Si_2$ alloy, which is paramagnetic at RT [6,30]. These paramagnetic phases are also detected at the neutron powder diffraction (NPD) patterns shown in Figure 4.14.

Note that the maximum Fe occupancy at any crystallographic site of the 1:12 structure is 4 atoms, i.e. 40% of the 10 Fe atoms per formula unit. Table 4.6 shows that the preferred Si occupancy is the 8*f* site for all samples, but for x = 0 there is also Si in the other two positions. Ce progressively displaces Fe from the 8*i* to the 8*j* positions, so Si is in turn displaced from the 8*j* to 8*i* sites. For x = 0.6, there is no Si in 8*j* position. Such preferential atomic occupancy has an influence on the magnetocrystalline anisotropy, as confirmed by the increase of the quadrupole splitting (QS) in position 8*f*. Moreover, the tendency of Ce to displace Fe to the 8*j* position can lead to instability of the 1:12 phase since, although the displacement of Fe from 8*i* is linear, it is not linear for 8*j*, leading to a formation of a secondary phase when x is slightly below 0.6. Once such positions are fully occupied, at some x above 0.3 and below 0.6, a further

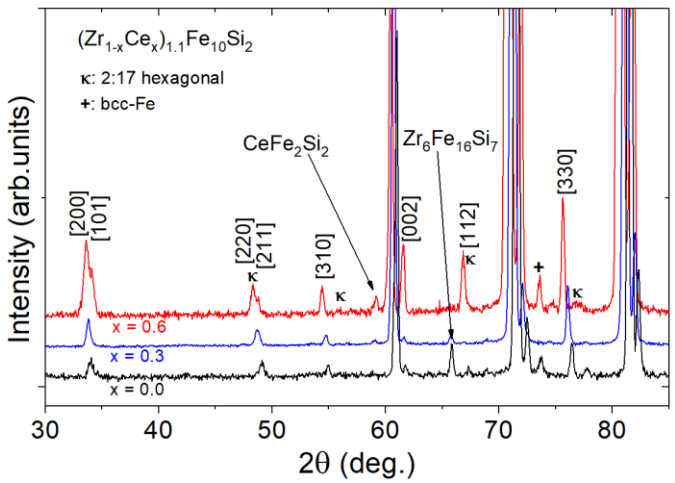

Figure 4.14- Magnified NPD patterns for all samples at RT.

increase of Ce cannot be accommodated by the same crystal structure, because no more Fe can be displaced to the 8*j* position, leading to a formation of a secondary phase.

Figure 4.15.a shows clear differences on M(T) depending on the field orientation for all samples. In particular for x = 0.6, and only for this composition, when the field is applied along the a-axis, the magnetisation shows two transitions; the first one around 450 K that can be associated with a secondary magnetic phase at this temperature. The second transition is the Curie temperature of the 1:12 phase (~560 K). The transition at 450 K was not clearly evidenced when the field was applied along the c-axis. We can explain this behaviour in terms of a small amount of a secondary magnetic phase, probably a 2:17 hexagonal phase, which has been reported to appear for x > 0.6 [6], and having Tc ~ 473 K. Some of the 2:17 phase diffraction peaks can be distinguished in the NPD pattern shown in Figure 4.14. This phase could be hidden in the Mössbauer spectra since its contribution is small and, once distributed into several sextets, can be blurred in the background noise. However, the WID of the 8*j* sub-spectrum for x = 0.6 is larger (0.52 mm/s) than in the others, hinting for an extra ferromagnetic contribution at RT in this compound.

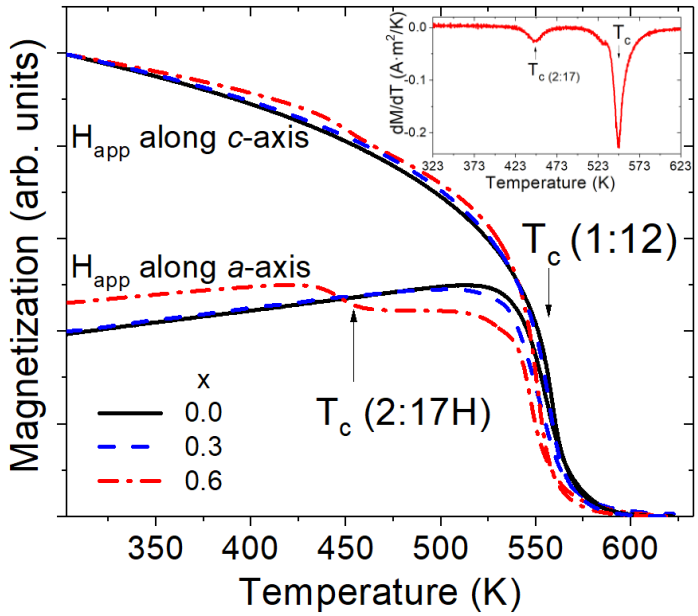

Figure 4.15- M(T) curves for all oriented samples with the magnetic field (10 mT) applied along the a- and c-axis.

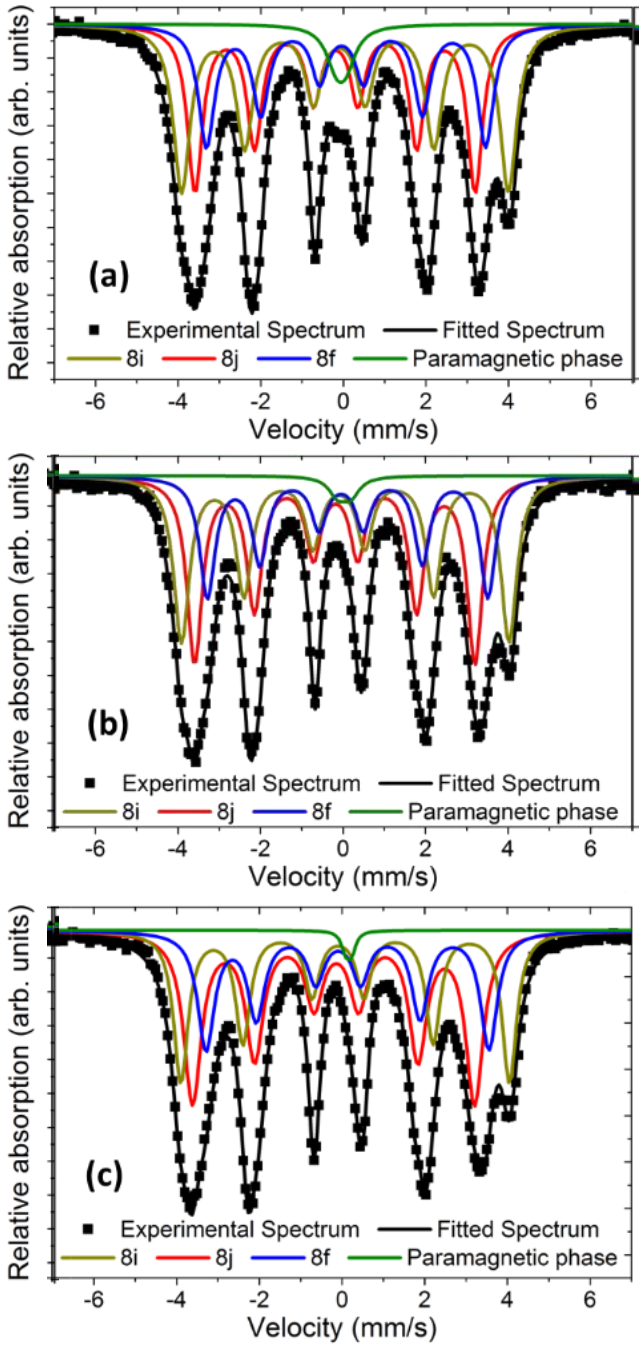

Figure 4.16- Mössbauer spectra at RT for (a) $Zr_{1.1}Fe_{10}Si_2$, (b) $(Zr_{0.7}Ce_{0.3})_{1.1}Fe_{10}Si_2$ and (c) $(Zr_{0.4}Ce_{0.6})_{1.1}Fe_{10}Si_2$ samples

Table 4.6- Mössbauer hyperfine parameters for $(Zr_{1-x}Ce_x)_{1.1}Fe_{10}Si_2$ compounds. ISO = Isomer Shift, QS = Quadrupole Splitting, B_{hf} = hyperfine field, WID = line width. The Fe content is referred only to the 1:12 phase, so the total Fe in 8i, 8j and 8f positions add to 100% to make clear the preferential occupancies of Fe and Si. Natural Width of the line is ≈ 0.27 mm/s.

Ce content	Fe position	% Fe	ISO	QS (mm/s)	B_{hf} (T)	WID (mm/s)
x=0.0	8*i*	**38**	0.07	0.14	24.5	0.44
	8*j*	**35**	-0.09	-0.01	21.0	0.44
	8*f*	27	0.11	**0.11**	21.0	0.47
	Paramagnetic	<2	0.03	0.21	-	0.32
x=0.3	8*i*	**35**	0.08	0.16	24.6	0.46
	8*j*	**39**	-0.09	-0.02	21.1	0.45
	8*f*	26	0.13	**0.16**	21.1	0.45
	Paramagnetic	<1	0.20	0.20	-	0.27
x=0.6	8*i*	**32**	0.09	0.17	24.6	0.42
	8*j*	**40***	-0.07	-0.06	21.1	0.52
	8*f*	28	0.12	**0.23**	21.2	0.49
	Paramagnetic	<1	0.40	0.17	-	0.27

NPD patterns at temperatures between 300 and 800 K were recorded for all samples. In Figure 4.17 is shown the diffraction patterns for x = 0.3 at 320 K, in the ferromagnetic state, and at 650 K, in the paramagnetic state. The difference between the high-temperature pattern and the low-temperature one reveals the magnetic contribution of the sample which appears at the [110] and [220] reflections. This magnetic contribution indicates that the magnetic moment lies along the direction perpendicular to these diffraction planes, i.e., along the c axis, confirming the uniaxial anisotropy of the sample. The magnetic moments of the atoms were not possible to be calculated accurately by the refinement of these patterns due to the insufficient magnetic contribution. This magnetic contribution decreases monotonously up to Tc, and therefore the easy direction is unchanged in all the temperature range.

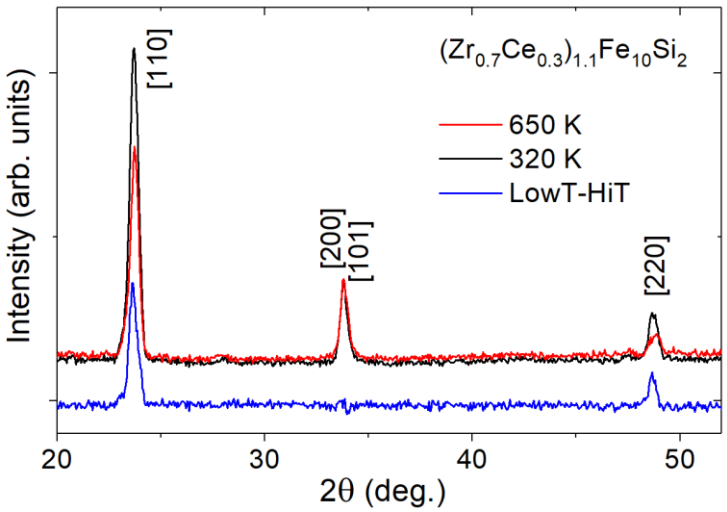

Figure 4.17- Neutron powder diffraction for x = 0.3, at the ferromagnetic (320 K) and the paramagnetic state (650 K).The difference show the magnetic peaks are only [110] and [220].

Figure 4.18.a shows the evolution with temperature of the [301] and [002] reflections, which are closely related with the lattice parameters *a* and *c* respectively. While the [301] reflection shifts linearly with temperature, the [002] reflection displacement is more complex. In order to study the evolution of the lattice parameters with temperature, a sequential refinement of the NDP patterns was done with the FullProf suite. The values of the *a* and *c* lattice parameters obtained by this refinement are shown in Figure 4.18.b and Figure 4.18.c respectively. The lattice parameter *a* presents a linear behaviour in agreement with

Figure 4.18.a, on the other hand, the lattice parameter *c* remains almost constant up to ~550 K. From this point, c starts to increase linearly. This change of behaviour occurs at the Curie temperature of the samples.

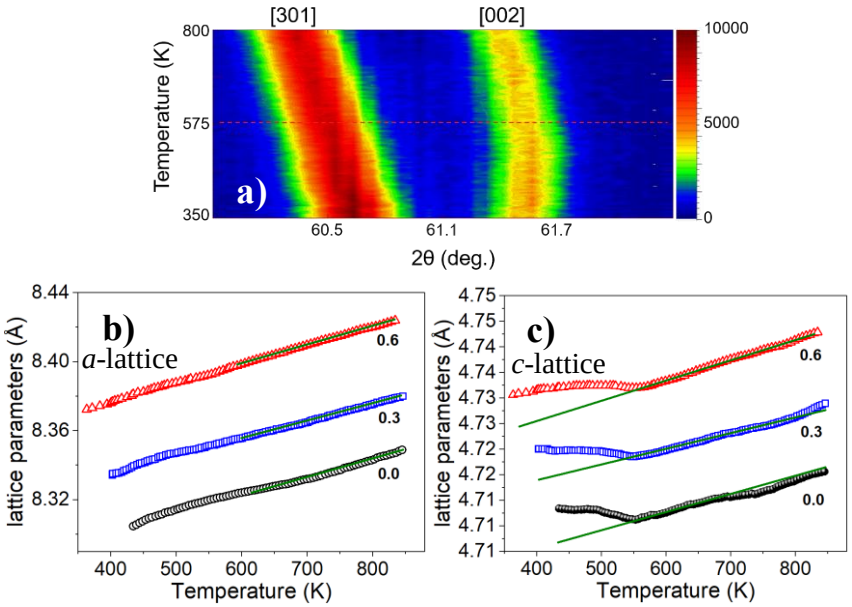

Figure 4.18- a) Neutron powder thermodiffraction for the sample with x = 0.3. b) *a*- and c) *c*-lattice parameters as a function of temperature for all samples

Linear thermal expansion coefficients (αL) were estimated from high-temperature data, in the paramagnetic state (above 600 K). Extrapolated to RT, αL along the a-axis are 1.69×10^{-5}, 1.45×10^{-5} and 1.48×10^{-5} K^{-1} for x = 0.0, 0.3 and 0.6 respectively, and along c-axis 0.98×10^{-5}, 1.00×10^{-5} and 1.00×10^{-5} K^{-1}. Although the αL values are quite similar for different compositions, they depend considerably on the crystalline orientation, being around a 50% higher along the a- than along the c-axis. These values are close to those reported in similar systems (Y(Fe,Mo)12) [31] which show a mainly linear thermal expansion.

Extrapolating the linear behaviour of *c* at high temperatures below Tc (solid line in Figure 4.18.c), we can obtain the difference on the *c* lattice parameter (Δ*c*) due to the anomaly. These differences are represented in Figure 4.19 and follow a clear M^3 law.

As the anomalous behaviour of the c-axis appears below the Curie temperature it can be considered as a magnetic one. It is directed along the

magnetic moment direction and, hence, can be assigned to a large positive spontaneous magnetostriction of $\lambda = \Delta c/c \approx 1500$ ppm at RT. This is of the same order of magnitude of the (Tb-Dy)Fe2 (TERFENOL-D) with $\lambda \approx 2000$ ppm at RT, the highest magnetostrictive compound known to date [32,33]. The direct dependence of Δc vs. $(M_s)^3$ shown in Figure 4.19 indicates a pure single ion contribution to the magnetostriction, indicating also the same origin for the uniaxial anisotropy, for all the compounds. Such analysis of the thermal dependence of the magnetostriction was proposed by O'Handley [34,35] in the 80's and successfully used for studying magnetostriction in amorphous ferromagnets [36]. The single ion term is due to the interaction between the Fe electron orbitals and the crystal electric field and scales as M^3, while a possible two ions contribution, which could arise from an anisotropic exchange between different magnetic atoms, like Fe and Ce, will follow an M^2 law[35].

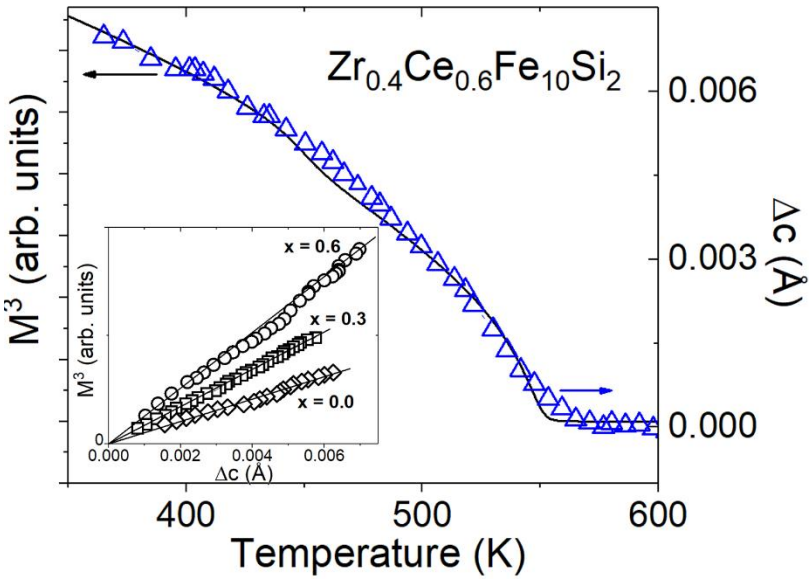

Figure 4.19- Evolution of Δc for x = 0.6 as a function of temperature compared with the corresponding M^3(T) curve. The inset shows the M^3 dependence of Δc for all the alloys

4.3.2 Nitrogenation of $Zr_{0.4}Nd_{0.6}Fe_{10}Si_2$

Unlike Ti-based nitrogenated alloys, several nitrogenation attempts were required for the $Zr_{0.4}Nd_{0.6}Fe_{10}Si_2$ at different temperatures, nitrogen pressures and times in order to get the nitrogenated sample. The processes carried out are summarised in Table 4.7. The range of temperatures used was 400-550 ºC, the pressure range was 6.7-20 bar and the time employed in the process varied from 4 to 18 hours.

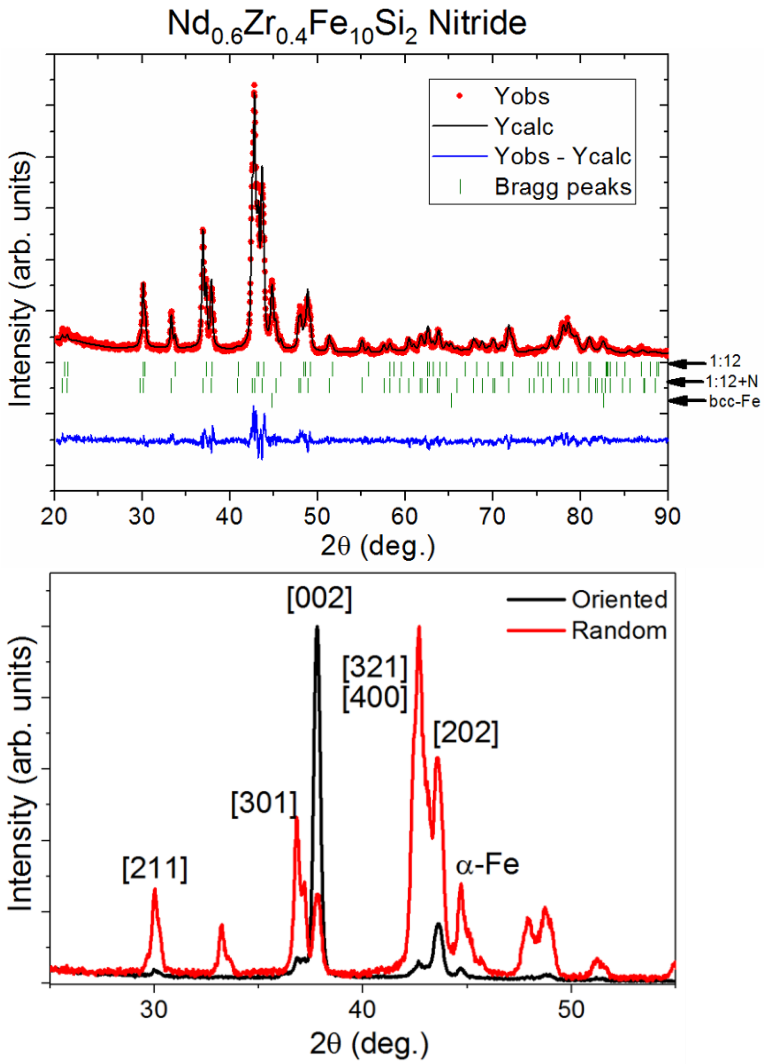

Figure 4.20- Rietveld refinement (up) of the best nitrogenated sample and the comparison between the random oriented and field oriented XRD pattern of the same sample (bottom).

In the thermo-magnetic curve of the best-nitrogenated sample (at 550 ºC with a pressure of 20 bar for 18 hours) shown in Figure 4.21 is possible to see two magnetic transitions under 550 ºC. The first one, at 295 ºC, corresponds with the base 1:12 structure [18] while the second one, at 380 ºC can be associated to the nitrogenated 1:12 structure. When the temperature reaches values above 550 ºC, the signal of the TGA starts to decrease, which indicates either a reduction of the magnetic signal or a loose of mass. This process can be assigned to the degradation of the nitrogenated sample at such high temperatures, either releasing the nitrogen or forming new phases more stable than the nitrogenated 1:12.

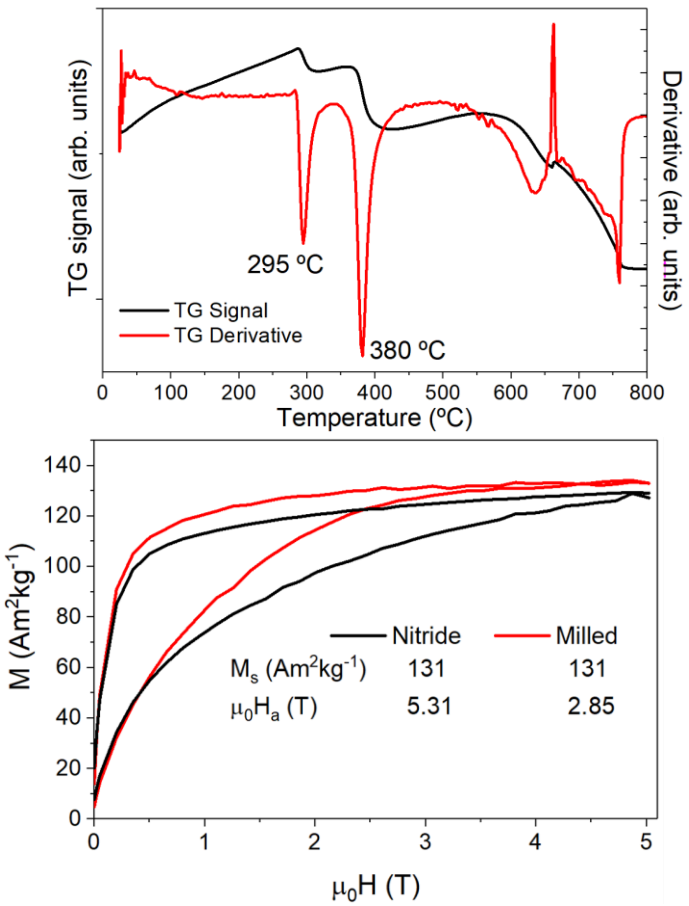

Figure 4.21- Thermo-magnetic curve of the best nitrogenated sample (top) and RT isotherms for field-oriented powders in parallel (//) and perpendicular (⊥) directions to the easy axis of magnetisation (bottom).

Table 4.7- Summary of the different attempts of nitrogenation with the conditions of the experiment, the increment of the mass and the volume (calculated from XRD) of the sample after the process and the ratio between phases.

Conditions	**Mass gain [%]**	**Volume increment [%]**	**1:12 [%]**	**1:12 nitrogenated [%]**	**α-Fe [%]**
Milled	-	-	99.5	-	0.5
4h - 6.7bar 400ºC	-	2	65.0	27.9	7.1
8h - 6.7bar 400ºC	-	2	57.6	35.3	7.1
2.5h - 20bar 500ºC	0.54	2	59.1	36.1	4.8
3h - 20bar 550ºC	0.83	2	44.5	49.5	6.0
18h - 20bar 550ºC	1.63	2.65	27.5	63.8	8.7

The XRD patterns refined by the Rietveld method shown in Figure 4.20 effectively show that the samples are composed of two well-differentiated 1:12 phases, a 27.5% in volume with the same crystal structure as the base 1:12 alloy and a 63.8% in volume with an expansion of the lattice parameters. The amount of α-Fe present in the sample is increased after the nitrogenation process in all cases, reaching a value of 8.7%. This expansion of the crystal structure was calculated to be of a 2.65% in volume, but with a different behaviour between the *c*-lattice parameter, which increases a 0.23%, and the *a*-lattice parameter, which increases in a 1.21%. This different expansion of the lattice parameters increases the tetragonal distortion of the structure, which can lead to the increase of the anisotropy as shown previously for $Zr_{1-x}Ce_xFe_{10}Si_2$.

The appearance of the XRD pattern and the good fitting achieved by the use of two differentiated 1:12 structures, with one of them remaining with the original lattice parameters, suggests that the partial nitrogenation of the sample is not due to the time of the process but to the presence of a superficial effect on some grains which impedes the starting of the nitrogenation.

The comparison of the XRD patterns of field-oriented powders and isotropic powders shows an enhancement of the [002] reflection indicating a uniaxial magnetocrystalline anisotropy along the c-axis. The reflections appearing together with this one, as the [202], can be related to the misorientation of the base 1:12, which presents a conical anisotropy [18], as deduced from Mössbauer spectroscopy in oriented powder samples.

From the magnetisation curves shown in Figure 4.21, it was possible to calculate the saturation magnetisation by the law of approach to saturation on the measurement parallel to the c-axis. This value, after being corrected for the presence of α-Fe, remained constant with the nitrogenation process at a value of 131 Am^2kg^{-1}. At the same time, the anisotropy field was greatly enhanced by an 86% from 2.85 T up to 5.31 T.

4.4 Summary and conclusions

In this chapter, several R-Fe 1:12 alloys have been studied to obtain magnetic properties worthy for application to permanent magnets. In order to get the 1:12 structure, Ti and Si have been used as stabilising elements.

For the first alloy, a study on the effect of Sm substitution for Ce in $Ce_{1-x}Sm_xFe_9Co_2Ti$ has been done. The anisotropy field of the $CeFe_9Co_2Ti$ alloy is too low to obtain a practical coercivity in the best heat treated melt-spun ribbons, achieving a value of just $\mu_0H_c = 0.08$ T. Substitution of Ce by Sm largely improves the magnetic anisotropy field, from 2.6 T up to 8.7 T for the $SmFe_9Co_2Ti$ alloy. This increment of the anisotropy shows a step between x = 0.25 and x = 0.5. Analysis of the Mössbauer spectra indicates a redistribution of cobalt in the 8*f* and 8*j* sites as the samarium concentration increases. It goes from 50/50 in the 8*j* and 8*f* sites respectively to 70/30 for Sm concentrations higher than x = 0.25. This coincides with the rise of the hyperfine field in the 8*j* site while the hyperfine field of 8*f* site decreases. The isomer shift also shows variations for Sm concentrations above 0.25. The redistribution of Co could be responsible for the behaviour of the anisotropy seen in these samples. Because of the improvement of the anisotropy by Sm substitution, the coercivity developed on the melt-spun ribbons after heat treatments is also increased up to 0.44 T for the $SmFe_9Co_2Ti$ alloy, which is a promising value for the development of medium-grade permanent magnets. However, the formation of α-Fe during heat treatments of these ribbons restricts the coercivity to a very low value relative to its anisotropy field.

The alloy $Nd_{0.5}Y_{0.5}Fe_{11}Ti$ shows a higher anisotropy field (1.75 T) than its counterpart $NdFe_{11}Ti$ (1 T) as theoretically predicted. The best nitrogenation process found for this sample was at 420 ºC for 4 hours. This process resulted in an increase of the lattice parameters of the crystal structure as well as the Curie temperature, from 270 ºC up to 390 ºC, and the anisotropy field, from the mentioned 1.75 T up to over 5 T. This enhancement of the magnetic properties upon nitrogenation was expected from the previous results on nitrogenation of the 1:12 structure found in the literature. A preliminary study was performed on the nitrogenation of melt-spun ribbons of this alloy. The as-melt-spun ribbons needed an annealing process of 4 hours at 1100 ºC to stabilise the 1:12 structure and presented a coercivity of 0.055 T. After three test of nitrogenation, the best sample obtained by a nitrogenation at 380 ºC for 4 hours presented

an enhanced coercivity of 0.1 T, but the amount of α-Fe was greatly increased. Further nitrogenation processes must be done in order to find the optimal temperature and time to avoid the formation of α-Fe while enhancing the coercivity.

The effect of Zr substitution for Ce in $Zr_{1-x}Ce_xFe_{10}Si_2$ has been studied. It was found that the increase of magnetic anisotropy in $Zr_{1-x}Ce_xFe_{10}Si_2$ (from $\mu_0 H_a$ = 2.0 T, for x = 0, up to 2.5 T for x = 0.6) correlates with the increase of the cell volume and the tetragonal distortion (*a/c*) of the lattice produced by the Ce substitution of Zr. However, no change in the magnetisation is observed. Mössbauer spectroscopy has shown that Ce displaces Fe from the 8*i* to the 8*j* position in the 1:12 structure and increases the crystal electric field gradient in the 8*f* position of Fe, leaving the hyperfine field unchanged in all Fe positions. The complete filling of 8*j* positions by Fe, for x slightly below 0.6, leads to the instability of the 1:12 phase upon a further increase of Ce, as when x = 0.6, more Fe cannot be accommodated by the same crystal structure, facilitating the formation of the 2:17 phase. An analysis on the thermal expansion was also carried out observing a *c*-lattice anomaly below Tc, which is assigned to a giant magnetostriction of about 1500 ppm in all the compounds at RT. The M^3 dependence of the magnetostriction reveals a pure single ion (or crystal field) origin of both the magnetostriction and the anisotropy in these compounds. The results so far indicate a pure geometric origin of the magnetic anisotropy.

Finally, the nitrogenation of $Zr_{0.4}Nd_{0.6}Fe_{10}Si_2$ has been presented. A partially nitrogenated sample was obtained after a nitrogenation process at 550 ºC with a pressure of nitrogen of 20 bar for 18 hours. This sample presented two differentiated structures, one 1:12 structure with the same lattice parameters as the original one and a second 1:12 structure with expanded lattice parameters. As this two structures were well-defined in the XRD patterns, the incomplete nitrogenation can be due to a surface effect on some of the grains of the sample, like oxidation, rather than a lack of time on the process. The magnetic properties of the nitrogenated sample were greatly enhanced, increasing the Curie temperature from 295 ºC up to 380 ºC and the anisotropy field from 2.85 T up to 5.31 T. The saturation magnetisation remained constant at a value of 131 Am^2kg^{-1}. The behaviour of the sample at high temperatures, not showing signs of degradation below 550 ºC, opens a door to the development of sintered magnets based on nitrogenated 1:12 alloys by means of alternative sintering processes as the spark plasma sintering technique.

4.5 References

[1] J. V. Florio, R.E. Rundle, A.I. Snow, Compounds of thorium with transition metals. I. The thorium–manganese system, Acta Crystallogr. 5 (1952) 449–457. doi:10.1107/S0365110X52001337.

[2] K.H.J. Buschow, Permanent magnet materials based on tetragonal rare earth compounds of the type RFe12-xMx, J. Magn. Magn. Mater. 100 (1991) 79–89. doi:10.1016/0304-8853(91)90813-P.

[3] M. Bacmann, C. Baudelet, D. Fruchart, D. Gignoux, E.K. Hlil, G. Krill, M. Morales, R. Vert, P. Wolfers, Exchange interactions and magneto-crystalline anisotropy in RFe12-xMxand parent interstitial compounds, in: J. Alloys Compd., Elsevier, 2004: pp. 166–172. doi:10.1016/j.jallcom.2004.04.083.

[4] D. Salazar, A. Martín-Cid, J.S. Garitaonandia, T.C. Hansen, J.M. Barandiaran, G.C. Hadjipanayis, Role of Ce substitution in the magneto-crystalline anisotropy of tetragonal ZrFe10Si2, J. Alloys Compd. 766 (2018) 291–296. doi:10.1016/j.jallcom.2018.06.225.

[5] S. Sakurada, A. Tsutai, M. Sahashi, A study on the formation of ThMn12 and NaZn13 structures in RFe10Si2, J. Alloys Compd. 187 (1992) 67–71. doi:10.1016/0925-8388(92)90521-A.

[6] A.M. Gabay, G.C. Hadjipanayis, ThMn12-type structure and uniaxial magnetic anisotropy in ZrFe10Si2and Zr1-xCexFe10Si2alloys, J. Alloys Compd. 657 (2016) 133–137. doi:10.1016/j.jallcom.2015.10.073.

[7] D. Goll, R. Loeffler, R. Stein, U. Pflanz, S. Goeb, R. Karimi, G. Schneider, Temperature dependent magnetic properties and application potential of intermetallic Fe 11- x Co x TiCe, Phys. Status Solidi - Rapid Res. Lett. 8 (2014) 862–865. doi:10.1002/pssr.201409270.

[8] Y. Matsuura, S. Hirosawa, H. Yamamoto, S. Fujimura, M. Sagawa, Magnetic Properties of the Nd2(Fe1-xCox)14B System., Appl. Phys. Lett. 46 (1985) 308–310. doi:10.1063/1.95668.

[9] Y. chang Yang, S. Hong, Z. Zhen-yong, L. Tong, G. Jian-liang, Crystallographic and magnetic properties of substituted YTi (Fe1-xTx)11, Solid State Commun. 68 (1988) 175–179. doi:10.1016/0038-1098(88)91094-0.

[10] S.F. Cheng, V.K. Sinha, Y. Xu, J.M. Elbicki, E.B. Boltich, W.E. Wallace, S.G. Sankar, D.E. Laughlin, Magnetic and structural properties of SmTiFe11-xCox alloys, J. Magn. Magn. Mater. 75 (1988) 330–338. doi:10.1016/0304-8853(88)90039-X.

[11] V.K. Sinha Cheng, S. F., Wallace, W. E., Sankar, S. G., Magnetic behavior of heavy rare earth RTiFe11-xCox alloys, J. Magn. Magn. Mater. 81 (1989) 227–233. doi:http://dx.doi.org/10.1016/0304-8853(89)90255-2.

[12] H. Wuest, L. Bommer, A.M. Huber, D. Goll, T. Weissgaerber, B. Kieback, Preparation of nanocrystalline Ce1−xSmx(Fe,Co)11Ti by melt spinning and mechanical alloying, J. Magn. Magn. Mater. 428 (2017) 194–197. doi:10.1016/j.jmmm.2016.12.036.

[13] C. Zhou, F.E. Pinkerton, J.F. Herbst, Magnetic properties of CeFe11−xCoxTi with ThMn12 structure, J. Appl. Phys. 115 (2014) 17C716. doi:10.1063/1.4863382.

[14] C. Zhou, K. Sun, F.E. Pinkerton, M.J. Kramer, Magnetic hardening of Ce1+xFe11−yCoyTi with ThMn12 structure by melt spinning, J. Appl. Phys. 117 (2015) 17A741. doi:10.1063/1.4918562.

[15] A. Martin-Cid, D. Salazar, A.M. Schönhöbel, J.S. Garitaonandia, J.M. Barandiaran, G.C. Hadjipanayis, Magnetic properties and phase stability of tetragonal Ce1-xSmxFe9Co2Ti 1:12 phase for permanent magnets, J. Alloys Compd. 749 (2018) 640–644. doi:10.1016/j.jallcom.2018.03.325.

[16] A.M. Gabay, A. Martín-Cid, J.M. Barandiaran, D. Salazar, G.C. Hadjipanayis, Low-cost $Ce_{1-x}Sm_{x}(Fe, Co, Ti)_{12}$ alloys for permanent magnets, AIP Adv. 6 (2016) 056015. doi:10.1063/1.4944066.

[17] A. Martín-Cid, A.M. Gabay, D. Salazar, J.M. Barandiaran, G.C. Hadjipanayis, Tetragonal Ce-based Ce-Sm$(Fe, Co, Ti)_{12}$ alloys

for permanent magnets, Phys. Status Solidi. 13 (2016) 962–964. doi:10.1002/pssc.201600102.

[18] M. Gjoka, V. Psycharis, E. Devlin, D. Niarchos, G. Hadjipanayis, Effect of Zr substitution on the structural and magnetic properties of the series Nd1-xZrxFe10Si2with the ThMn12type structure, J. Alloys Compd. 687 (2016) 240–245. doi:10.1016/j.jallcom.2016.06.098.

[19] Y. Morii, H. Sun, H. Fujii, Y. Miyazaki, M. Akayama, S. Funahashi, Neutron powder diffraction from nitrogenated YFe11Mo, YFe9Mo3 and NdFe8Co3Ti, Phys. B Condens. Matter. 213–214 (1995) 291–293. doi:10.1016/0921-4526(95)00133-T.

[20] C.-K. Loong, S.M. Short, J. Lin, Y. Ding, A study of nitrogenation of a NdFe12−xMox compound by in situ neutron powder diffraction, J. Appl. Phys. 83 (1998) 6926. doi:10.1063/1.367658.

[21] S. Asano, S. Ishida, S. Fujii, Electronic structures and improvement of magnetic properties of RFe12X (R = Y, Ce, Gd; X = N, C), Phys. B Condens. Matter. 190 (1993) 155–168. doi:10.1016/0921-4526(93)90461-E.

[22] D. Nunes, R. Colaço, A.P. Gonçalves, L.C.J. Pereira, P.A. Carvalho, Microstructures and magnetic domain configurations of NdFe11Ti and Nd2(Fe,Ti)17 aggregates, Appl. Phys. A Mater. Sci. Process. 104 (2011) 1053–1060. doi:10.1007/s00339-011-6365-5.

[23] J. Yang, W. Mao, B. Cheng, Y. Yang, H. Xu, B. Han, S. Ge, W. Ku, Magnetic properties and magnetic domain structures of NdFe10.5Mo1.5 and NdFe10.5Mo1.5Nx, Appl. Phys. Lett. 71 (1997) 3290–3292. doi:10.1063/1.120315.

[24] T. Dragon, A. Forkl, Investigation of the Domain Structure of NdFellTi and NdFellTiN , Phys. Status Solidi. 749 (1996) 749–754. doi:10.1002/pssa.2211540228.

[25] H. Sun, Y. Otani, J.M.D. Coey, C.D. Meekison, J.P. Jakubovics, Coercivity and microstructure of melt-spun Sm(Fe11Ti), J. Appl. Phys. 67 (1990) 4659–4661. doi:10.1063/1.344845.

[26] P. Oleinek, W. Kockelmann, K.-H. Müller, M. Loewenhaupt, L. Schultz, Neutron and X-ray powder diffraction study on the compound NdFe10.75V1.25Ny, J. Alloys Compd. 281 (1998) 306–311. doi:10.1016/S0925-8388(98)00782-8.

[27] C. Zhou, F.E. Pinkerton, J.F. Herbst, High Curie temperature of Ce–Fe–Si compounds with ThMn12 structure, Scr. Mater. 95 (2015) 66–69. doi:10.1016/J.SCRIPTAMAT.2014.10.006.

[28] A.V. Andreev, S.V. Andreev, E.N. Tarasov, Magnetic properties of UFe12−xSix, J. Less Common Met. 167 (1991) 255–259. doi:10.1016/0022-5088(91)90280-H.

[29] C. Zhou, F.E. Pinkerton, J.F. Herbst, Cerium-iron-based magnetic compounds, 2014. https://patents.google.com/patent/US9548150B2/en (accessed October 7, 2018).

[30] A.M. Gabay, R. Cabassi, S. Fabbrici, F. Albertini, G.C. Hadjipanayis, Structure and permanent magnet properties of Zr1-xRxFe10Si2alloys with R = Y, La, Ce, Pr and Sm, J. Alloys Compd. 683 (2016) 271–275. doi:10.1016/j.jallcom.2016.05.092.

[31] H. Sun, M. Akayama, K. Tatami, H. Fujii, Magnetic properties of YFe12-xMox and YFe12-xMoxNy ($0.5 \leq x \leq 4.0$, $y \approx 1$), Phys. B Phys. Condens. Matter. 183 (1993) 33–39. doi:10.1016/0921-4526(93)90050-G.

[32] A.E. Clark, Magnetostrictive rare earth-fe compounds, 1980. doi:10.1016/S1574-9304(05)80122-1.

[33] G. Engdahl, E. Quandt, Handbook of Giant Magnetostrictive Materials, Academic Press, 2000. doi:10.1016/B978-012238640-4/50022-X.

[34] R.C. O'Handley, Magnetostriction of transition-metal-metalloid glasses: Temperature dependence, Phys. Rev. B. 18 (1978) 930–938. doi:10.1103/PhysRevB.18.930.

[35] R.C. O'Handley, M.O. Sullivan, Magnetostriction of Co80-xTxB20(T = Fe, Mn, Cr, or V) glasses, J. Appl. Phys. 52 (1981) 1841–1843. doi:10.1063/1.329546.

[36] J.M. Barandiarán, A. Hernando, O. V. Nielsen, Temperature dependence of magnetostriction in [Co1-x (FeNi)x]75Si 15B10 amorphous alloys, J. Magn. Magn. Mater. 46 (1985) 317–320. doi:10.1016/0304-8853(85)90052-6.

5 Fully Rare earth free magnets

5.1 Introduction

In previous chapters, the results obtained in phases with a reduction of rare earths (RE) were shown, but the ideal material for a permanent magnet with no critical raw materials would be a totally RE-free one. In this chapter, we show the attempt to obtain a new RE-free phase based on the theoretical work done by some partners of the H2020 European project NOVAMAG.

As commented before, the project has used a "bottom-up" theoretical approach has been used to look for new uniaxial ferromagnetic phases, predict their magnetic properties and their potential for developing advanced permanent magnets.

The first step of the theoretical work was the calculation of the crystal structure of many possible compounds, for what an Adaptive Genetic Algorithm (AGA) [1,2] is used with the software Universal Structure Predictor: Evolutionary Xtallography (USPEX) [3] combined with the Vienna Ab initio simulation package (VASP) [4–6]. With this procedure, the crystal phase space of Fe-rich binary and ternary phases was explored searching for new non-cubic structures with high stability and high saturation magnetisation.

Several Fe-rich binary phases were theoretically predicted within the project and experimental efforts were made to actually produce them. For instance Fe_3Sn was synthesised but did not presented uniaxial anisotropy as predicted. Diluting it with Mn and Sb, should produce uniaxial anisotropy, but it generated the segregation of other phases or remained having a planar anisotropy. The predicted hexagonal structure of Fe_5Sn was not possible to achieve by different non-equilibrium techniques as melt-spinning, mechanical alloying or solid state reaction. Another two theoretically predicted phases, Fe_2Ge and Fe_5Ge, were not possible to obtain by any of the three techniques mentioned before.

As part of the project, the Co-Fe-Ta system was assigned to BCMaterials and the University of Delaware, and part of the research was designated to be part of this work. This system was theoretically predicted to exhibit an increased magnetic anisotropy with a Curie temperature much larger than other Fe-Co-M (M = Hf, Zr) [7,8]. The systematic crystal structure

calculation of this system yielded around 40 metastable non-cubic structures with interest for their use as permanent magnets. Among these crystal structures, some of them stand out for being very close to the ground state and have a rhombohedral structure (space group 160), with a stoichiometry $CoFe_4Ta$, $CoFe_6Ta$ and $CoFe_8Ta$. Another interesting phase was the $CoFe_6Ta$ with tetragonal (space group 115) structure, which had the lowest enthalpy of formation of all the Co-Fe-Ta systems predicted by AGA.

The second step is the study of the magnetic properties of the newly predicted phases by first-principles methods using spin-polarised density functional theory (DFT). The full calculation comprises the determination of the saturation magnetisation, the magnetocrystalline anisotropy energy (MAE), and temperature dependent properties such as the Curie temperature T_C as well as the magnetisation M(T). In addition, CALPHAD simulations have been carried out to study metastable phases. To get insight into the temperature dependent properties (M(T), T_C) the exchange coupling parameters J_{ij} had to be calculated. These coupling parameters J_{ij} have been derived from the Liechtenstein approach [9], which allows one to calculate magnetic interactions for an arbitrary arrangement of magnetic moments. This approach is implemented in several DFT codes and lately, it also became part of the RSPt code maintained in the University of Uppsala [10]. These calculations showed that the two phases with the lowest energy of formation for $CoFe_6Ta$ fulfilled the minimum criterion for the hardness factor $\kappa > 0.5$.

As these theoretical methods give many possible phases with potential properties for permanent magnet application, a first experimental approach to check their existence is the use of high-throughput synthesis

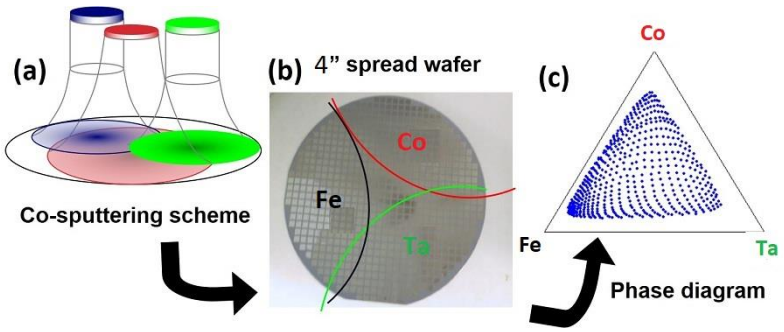

Figure 5.1. - Schematic representation of combinatorial thin film deposition.

(HTS). The working principle of the high-throughput methods is the complete compositional mapping of the multiple material systems [11].

One of the most common HTS techniques is the combinatorial thin film deposition using sputtering, shown in Figure 5.1. It was used to look for phases in the Fe-Co-Ta system by NCSR Demokritos. The sputter sources are tilted, thus resulting in a graded deposition: areas of the wafer closer to the source receive more deposited materials, whereas areas farther from the source receive less deposited material. With this technique, a high coercivity Co-rich phase was found but the anisotropy was determined to be planar which is not useful for permanent magnet applications.

A second technique is the reactive crucible melting (RCM), used by the Technische Universität Darmstadt (TUDA) to study the FeCoTa system within NOVAMAG. RCM was first introduced in 2001 by Lüdtke who used the method in order to search for new hard magnetic phases [12]. In the RCM technique, represented in Figure 5.2, the crucibles are made from one of the elements in the system under investigation. The other elements in the examined system are added into the crucibles in the form of crushed pieces or powders with high purity. The filled crucibles are then closed under argon atmosphere, wrapped in metal foils, sealed in an evacuated quartz tube and then heat treated at a desirable temperature. During the annealing, added elements in the crucible should be melted and diffused into the solid-state crucible element and therefore the intermediate phases between the liquid and the crucible element form. By the formation of the concentration gradient and depending on the composition range between the melt and crucible element, the intermetallic phases according to thermodynamically guided diffusion processes

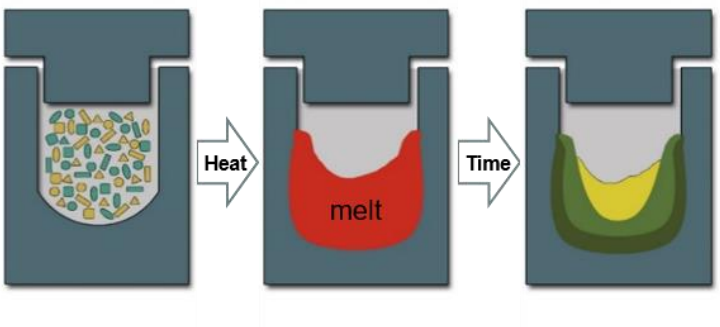

Figure 5.2- Schematic representation of production procedure for reactive crucible melting

would form. The existence of liquid phases in this method enhances the diffusion speed. With this technique, three new phases were found in the Fe-Co-Ta system, $TaFe_3$, $Ta(Fe,Co)_3$, and $Co(TaFe)_6$ by researchers of TUDA. However, to the best of our knowledge, no data on the structure and magnetic properties of these phases have been disclosed.

With all these results in mind, a first attempt of synthesising some of these new phases was done by melt-spinning at the University of Delaware by Aleksandar Gabay. After preparing ribbons in several compositions on the Co-rich region of the Fe-Co-Ta system, some coercivity was found at room temperature, but XRD showed that the only non-cubic phase present in the ribbons had the C14 Laves structure. This led to the systematic study of the region near the reporting C14 Laves phase existence for this alloy.

* All results presented in this introduction are private communications and produced by the following partners of the NOVAMAG project: Universidad de Burgos / ICCRAM, Uppsala University, National Centre of Scientific Research "Demokritos", Technische Universität Darmstadt and the University of Delaware.

5.2 C14 Laves non-cubic phases in Fe-Co-Ta system

There are few reports on the magnetic properties of the $(Fe,Co)_2Ta$ laves phase [13–17], and all of them report a paramagnetic behaviour above room temperature. In order to see the evolution of the properties on this

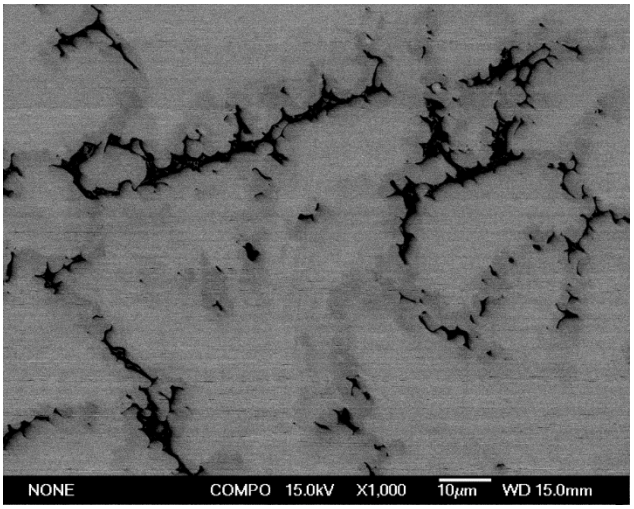

Figure 5.3- SEM image of $Fe_{50}Co_{20}Ta_{30}$ before annealing showing the presence of at least two phases.

system, a number of different compositions were synthesised by arc-melting of the pure constituents and later annealed at 1175 ºC for 15 hours in order to homogenise the sample: $Fe_{70}Ta_{30}$, $Fe_{60}Co_{10}Ta_{30}$, $Fe_{50}Co_{20}Ta_{30}$, $Fe_{40}Co_{30}Ta_{30}$, $Fe_{30}Co_{40}Ta_{30}$, $Fe_{20}Co_{50}Ta_{30}$, $Fe_{10}Co_{60}Ta_{30}$, $Fe_{54}Co_{21}Ta_{25}$ and $Fe_{57}Co_{23}Ta_{20}$. These compositions were selected to see the evolution on the composition of the samples of the C14 Laves phase from the lowest amount of Ta to crystallise in this structure at low temperature (30 at.%), as reported in the phase diagram of Fe-Ta, Figure 5.4, as Fe was substituted by Co, and afterwards, to see the effect of the reduction of Ta in the alloy.

SEM image shown in Figure 5.3 indicates the presence of three phases, a dark phase corresponding with α-Fe(Co), a bright one, which corresponds with the Laves C14 phase, and an intermediate phase that was not identified. Due to the limitations of the electron microscope used (a JEOL JSM-6335F), the atomic percentage of the bright and intermediate region could not be accurately estimated.

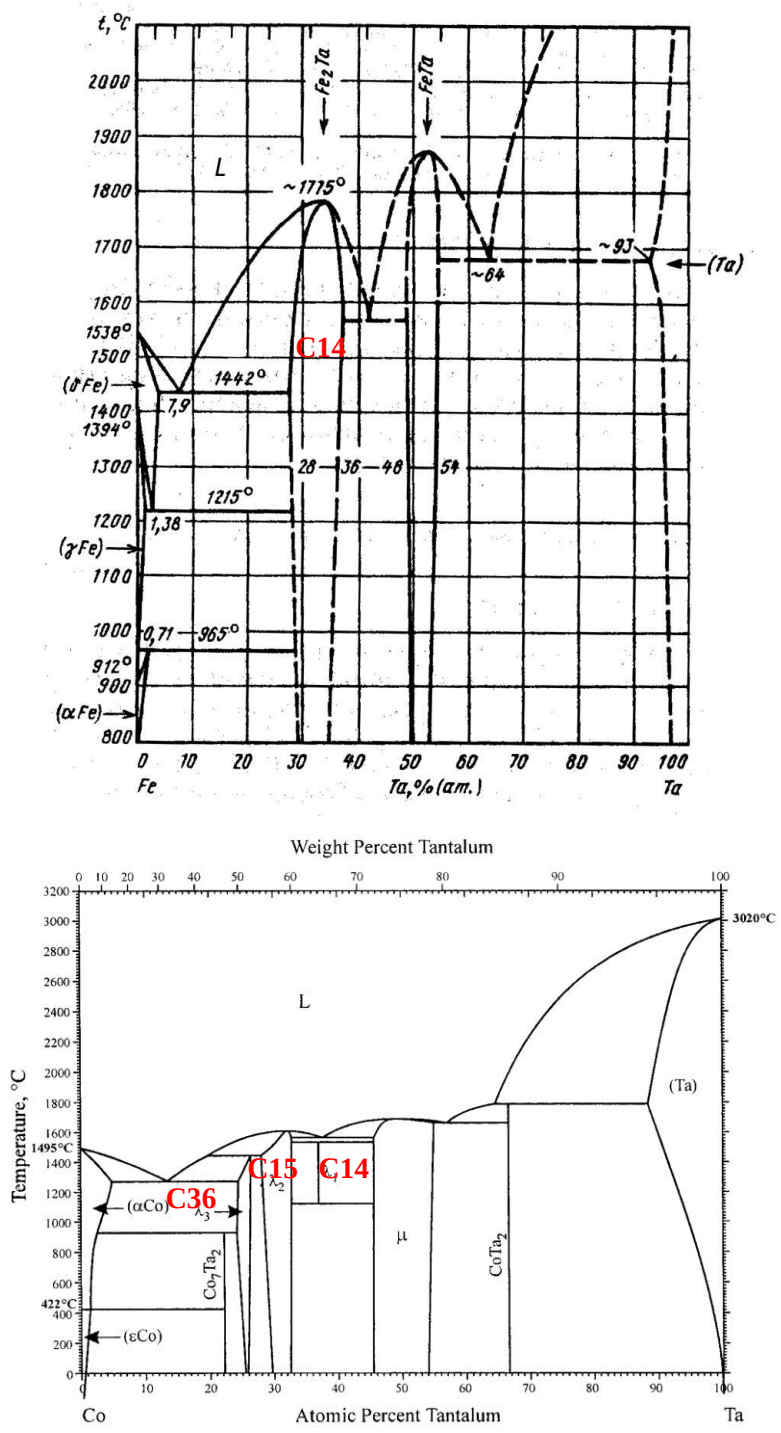

Figure 5.4- Phase diagram of the Fe-Ta system (top) and the Co-Ta system (bottom) [Okamoto, H. J Phs Eqil and Diff (2004) 25: 571.].

The evolution of the phases present at the samples with the content of Co can be appreciated from the XRD shown in Figure 5.5. There are several aspects worth mentioning about these results. First, the sample with the larger amount of Co shows a predominant component of the C15 Laves phase, which agrees with the expected phase from a pure Co_2Ta alloy according to the Co-Ta phase diagram. Secondly, the $Fe_{20}Co_{50}Ta_{30}$ sample shows a reflexion of an unknown phase at 36º after annealing, while the intensity of the reflexion at 41º decreases, suggesting the formation of another phase at the expense of the C14 Laves one. Regarding the other samples, all of them show the typical pattern of the C14 Laves phase, with a small reduction of the width of the peaks after annealing.

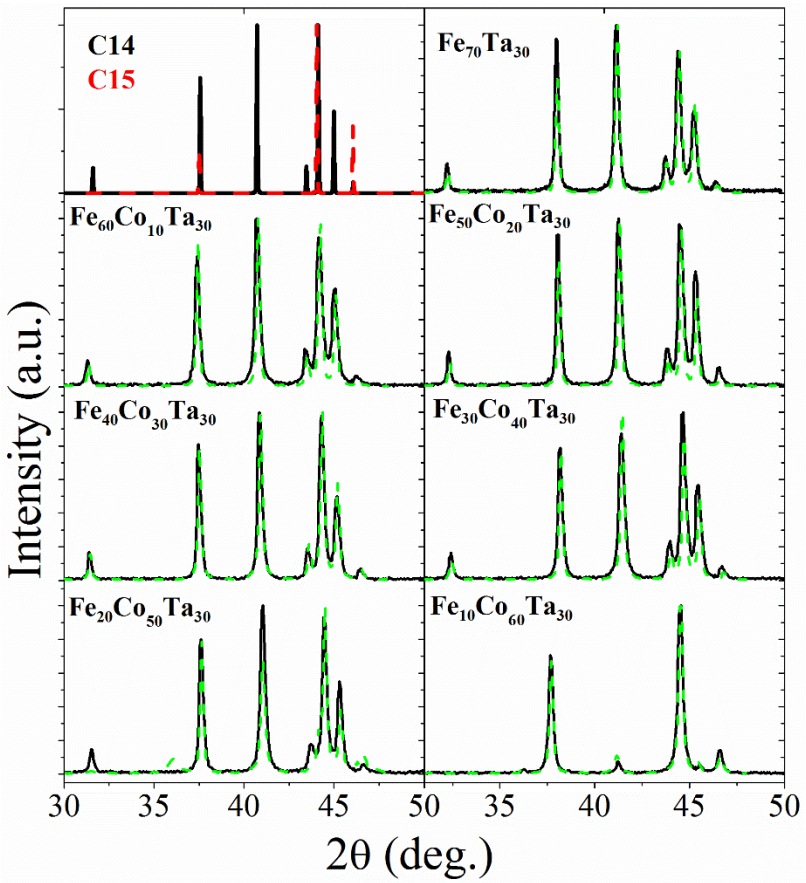

Figure 5.5- XRD patterns for the different samples with constant Ta amount. On the top left corner are the theoretically calculated patterns for the Laves phases C14 and C15. The black solid lines are the patterns for the as-cast samples and the green dashed lines are the annealed samples patterns

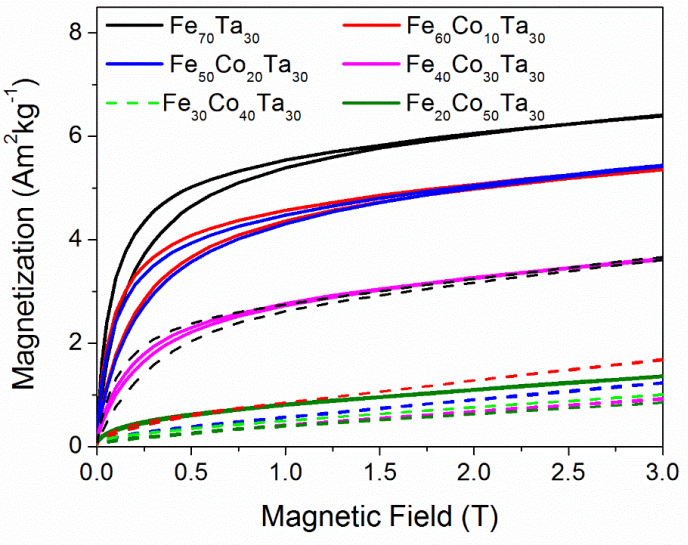

Figure 5.6- M(H) curves at RT for the different samples with the C14 Laves phase as-cast (solid lines) and after annealing (dashed lines).

The samples with 30% or less content of Co present a ferromagnetic behaviour that is lost after annealing, excluding the sample without Co as shown in Figure 5.6. It is worth noticing that the sample without Co has a room temperature magnetisation of 6 Am^2kg^{-1} at the most, which is a very low value for any practical application.

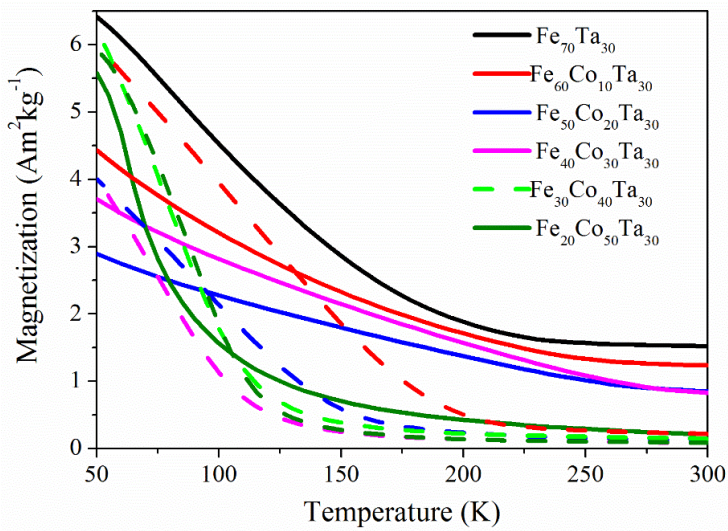

Figure 5.7- M(T) curves at 0.05 T for the different samples with the C14 Laves phase as-cast (solid lines) and after annealing (dashed lines).

Regarding the M(T) curves shown in Figure 5.7, the as-cast alloys present a nearly monotonous decrease of the magnetisation with the temperature, which, together with the wider peaks in XRD patterns, suggest the existence of a chemical inhomogeneity. After annealing, the transition from a ferromagnetic to a paramagnetic state is more abrupt. The Curie temperature for these alloys is around 100-150 K. At a higher temperature, a small magnetisation remains in the samples, indicating that a small amount of a ferromagnetic phase is present. The small incrustations of α-Fe(Co) shown on SEM images contribute to the magnetisation by less than 0.2 Am^2kg^{-1}.

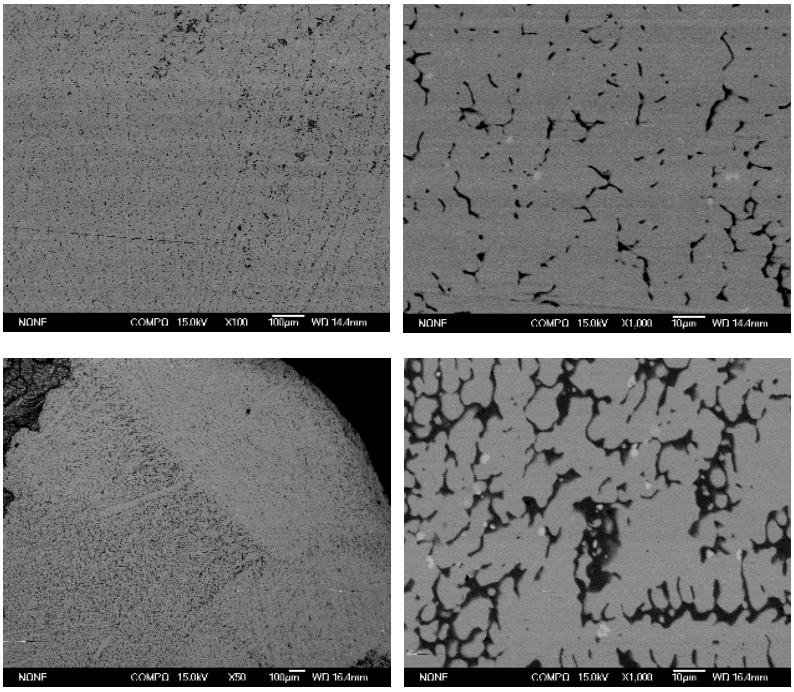

Figure 5.8- SEM images of Ta 25 at.% at 100x (top left) and 1000x (top right), and Ta 20 at.% at 50x (bottom left) and 1000x (bottom right). The black region corresponds with α-Fe(Co) while the grey regions could not be calculated the exact atomic percentage of the elements.

The SEM images of the non-stoichiometric samples with 25 at.% and 20 at.% of Ta after annealing are shown in Figure 5.8. The sample with the lowest amount of Ta presents a higher concentration of Fe than the one with higher Ta amount. As before, the atomic composition of the bright regions of the images could not be properly estimated due to the characteristics of the electron microscope used.

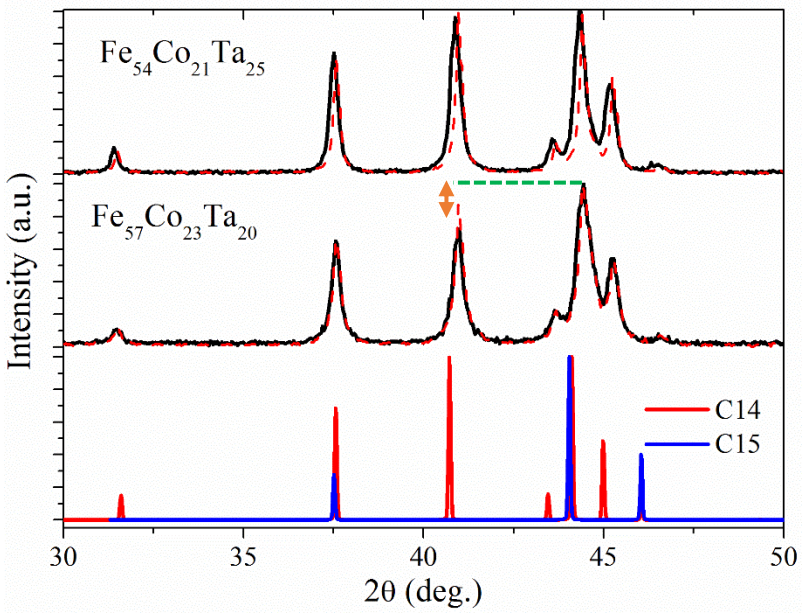

Figure 5.9- XRD patterns of the non-stoichiometric samples before (solid black lines) and after (red dashed lines) annealing and the theoretical patterns for the C14 and C15 Laves phases. The green line and orange arrow shows the difference on intensity between two of the reflexions.

From the XRD shown in Figure 5.9 is possible to see that both samples present the C14 Laves phase. It is also possible to see the excess of α-Fe(Co) on the sample with a lower amount of Ta by the difference of height between the peaks with higher intensity. As with the stoichiometric samples, after annealing, a reduced width on the reflexions of the XRD patterns can be appreciated.

The reduction of the amount of Ta in the alloy produces a huge increase in the magnetisation as can be seen in Figure 5.10. In the alloy with 20 at.% of Ta this increase is mostly due to the presence of Fe, but in the alloy with 25 at.%, the intrinsic saturation magnetisation reaches 15-20 Am^2kg^{-1}, which is actually still a very low value for applications. The behaviour of both samples before and after annealing is also interesting. The sample with lower Ta amount does not show any change, suggesting that the lower limit of Ta concentration in the C14 Laves phase has been reached. On the other hand, the sample with a higher amount of Ta presents a reduction of the magnetisation after annealing,

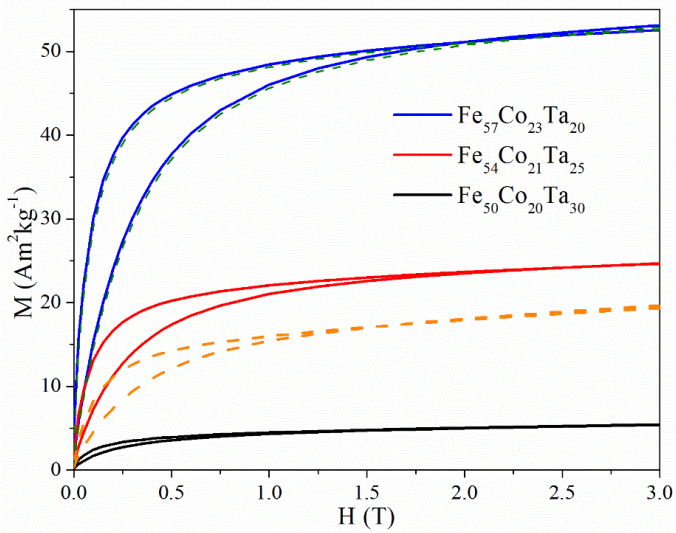

Figure 5.10- M(H) curves at RT of the non-stoichiometric samples before (solid lines) and after (dashed lines) annealing.

which suggests a homogenisation of the sample with the consequent reduction of the α-Fe(Co) content. In both cases, a ferromagnetic behaviour with some anisotropy is present before and after the annealing process.

The M(T) curves of Figure 5.11 show an increase of the Curie temperature reaching values of 220 K after annealing. In these samples we can see the same effect as before, the smooth transition of the magnetisation

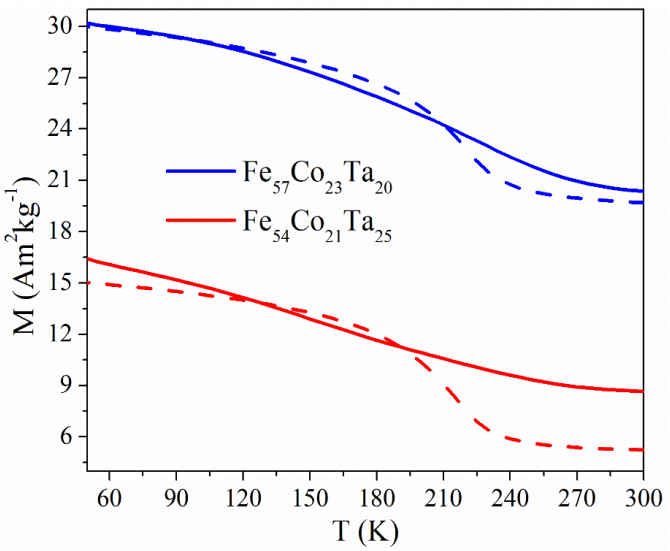

Figure 5.11- M(T) curves for the non-stoichiometric samples before (solid lines) and after (dashed lines) annealing.

before the annealing sharpens after the heat treatment. The residual magnetisation on both samples suggests that there is a ferromagnetic phase at room temperature. Some of the residual magnetisation can be associated with the presence of α-Fe(Co), especially in the sample with a lower amount of Ta, but, the great anisotropy found at room temperature in the M(H) curves gives some insight about the existence of a third phase, however unidentified.

5.3 Summary and conclusions

In this chapter, the attempt for finding a RE-free alloy with uniaxial anisotropy in the Fe-Co-Ta system has been shown. This study was motivated by the reports of other partners on the NOVAMAG project who suggested the existence of potential phases in the Fe-Co-Ta system by theoretical predictions and HTS methods like combinatorial synthesis in thin film and reactive crucible melting.

The alloys have been prepared by arc-melting and annealed at 1175 ºC for 15 hours. For different Fe/Co ratios in the $(Fe,Co)_{70}Ta_{30}$ system, there is no other ferromagnetic phase aside from the C14 Laves phase. This phase is stable at room temperature but shows a very low magnetisation of 6 Am^2kg^{-1} and no useful anisotropy. Reducing the amount of Ta on the alloys, and near the predicted composition: $Co_{0.25}Fe_{0.5}Ta_{0.25}$, the Curie temperature is increased by almost 100 K and we found a hint of a third phase aside from the C14 and α-Fe(Co) that is ferromagnetic at room temperature and has some anisotropy. Anyway, the low magnetisation shown by these samples discards them for permanent magnet applications. Multiple preparation approaches should be taken in order to try to get the theoretically predicted phases, which if really exist, will be highly metastable ones. The unsuccessful trial with melt spinning at the University of Delaware is, however, discouraging.

We can conclude that, in spite of the theoretical predictions of new magnetic phases in the (Fe,Co)Ta system, strong experimental efforts should be made to find a new compound suitable for permanent magnets applications. The same happens in other explored Fe rich binary and ternary phases.

5.4 References

[1] P. Nieves, S. Arapan, G.C. Hadjipanayis, D. Niarchos, J.M. Barandiaran, S. Cuesta-Lopez, Applying high-throughput computational techniques for discovering next-generation of permanent magnets, Phys. Status Solidi Curr. Top. Solid State Phys. 13 (2016) 942–950. doi:10.1002/pssc.201600103.

[2] S. Arapan, P. Nieves, S. Cuesta-López, A high-throughput exploration of magnetic materials by using structure predicting methods, J. Appl. Phys. 123 (2018) 083904. doi:10.1063/1.5004979.

[3] A.O. Lyakhov, A.R. Oganov, H.T. Stokes, Q. Zhu, New developments in evolutionary structure prediction algorithm USPEX, Comput. Phys. Commun. 184 (2013) 1172–1182. doi:10.1016/j.cpc.2012.12.009.

[4] H. Giefers, M. Nicol, Equations of state of several iron-tin intermetallic compounds, J. Phys. Chem. Solids. 67 (2006) 2027–2032. doi:10.1016/j.jpcs.2006.05.056.

[5] G. Trumpy, E. Both, C. Djéga-Mariadassou, P. Lecocq, Mössbauer-effect studies of iron-tin alloys, Phys. Rev. B. 2 (1970) 3477–3490. doi:10.1103/PhysRevB.2.3477.

[6] G. Kresse, J. Hafner, Ab initio molecular dynamics for liquid metals, Phys. Rev. B. 47 (1993) 558–561. doi:10.1103/PhysRevB.47.558.

[7] N.N. Phuoc, P. Chapon, O. Acher, C.K. Ong, Large magneto-elastic anisotropy enhancement with temperature in composition-graded FeCoTa thin films, J. Appl. Phys. 114 (2013) 153903. doi:10.1063/1.4825225.

[8] N.N. Phuoc, C.K. Ong, Gradient-Composition Sputtering: An Approach to Fabricate Magnetic Thin Films With Magnetic Anisotropy Increased With Temperature, IEEE Trans. Magn. 50 (2014) 1–6. doi:10.1109/TMAG.2013.2296936.

[9] A.I. Liechtenstein, M.I. Katsnelson, V.P. Antropov, V.A. Gubanov, Local spin density functional approach to the theory of exchange interactions in ferromagnetic metals and alloys, J.

Magn. Magn. Mater. 67 (1987) 65–74. doi:10.1016/0304-8853(87)90721-9.

[10] J.M. Wills, O. Eriksson, P. Andersson, A. Delin, O. Grechnyev, M. Alouani, Full-Potential Electronic Structure Method, Springer Berlin Heidelberg, Berlin, Heidelberg, 2010. doi:10.1007/978-3-642-15144-6.

[11] J.J. Hanak, The "multiple-sample concept" in materials research: Synthesis, compositional analysis and testing of entire multicomponent systems, J. Mater. Sci. 5 (1970) 964–971. doi:10.1007/BF00558177.

[12] A. Ludtke, Reaction crucible analysis and magnetic domain structures, (2001). https://ethos.bl.uk/OrderDetails.do;jsessionid=2B5740D1D4E38D221364E411C6785FB6?uin=uk.bl.ethos.399311 (accessed August 30, 2018).

[13] K. Kai, T. Nakamichi, M. Yamamoto, Magnetic Behavior of the Laves Phase Compound in Fe-Ta Binary System, J. Phys. Soc. Japan. 29 (1970) 1094–1095. doi:10.1143/JPSJ.29.1094.

[14] K. Ikeda, T. Nakamichi, Electrical Resistivity of Laves Phase Compounds Containing Transition Elements I. Fe 2 A (A=Sc, Y, Ti, Zr, Hf, Nb, and Ta), J. Phys. Soc. Japan. 39 (1975) 963–968. doi:10.1143/JPSJ.39.963.

[15] L.J. Swartzendruber, E. Paul, The Fe-Ta (Iron-Tantalum) system, Bull. Alloy Phase Diagrams. 7 (1986) 254–259. doi:10.1007/BF02869001.

[16] Y. Nishihara, Magnetic properties of Laves phase compounds with iron, J. Magn. Magn. Mater. 70 (1987) 75–80. doi:10.1016/0304-8853(87)90367-2.

[17] Y. Horie, S. Kawashima, Y. Yamada, G. Obara, T. Nakamura, Magnetic properties of Ta($Fe_{1-x}T_x$)$_2$ with T =V, Cr, Mn, Co and Ni, J. Phys. Conf. Ser. 200 (2010) 032078. doi:10.1088/1742-6596/200/3/032078.

6 General conclusions and open perspectives

6.1 General conclusions

This thesis proposes three different lines of work, to overcome the criticality of rare earths in the area of permanent magnets: From the reduction of heavy rare earths in the widely known Nd-Fe-B type of magnets (Chapter 3), passing through the search of rare earth reduction with promising ferromagnetic phases in the $ThMn_{12}$-type structure (Chapter 4), to the complete removal of rare earth by searching ferromagnetic alloys with uniaxial anisotropy in the Fe-Co-Ta system (Chapter 5).

The main conclusions obtained for each line of work are as follow:

Chapter 3:

- Magnetic properties of Nd-Fe-B based magnets can be improved without heavy rare earths as Dy or Tb, by using Nb and Cu to control the crystallisation process on melt-spun ribbons of Nd-lean alloys.

- Nb increase the crystallisation temperature of the 2:14:1 phase, by inhibition of the grain growth

- Cu reduces the crystallisation temperature of the 2:14:1 phase, by promoting early nucleation, as well as helps the crystallisation of the secondary α-Fe phase. The latter is detrimental to the exchange coupling.

- Infiltration of a eutectic alloy (Pr_3(Co,Cu)) in Nd-Fe-B alloys by Grain Boundary Diffusion Process (GBDP) enhances the coercivity five-fold, reaching a value of 2.5 T, comparable to commercial magnets used in motors and wind generators applications containing Dy.

- α-Fe was greatly reduced after the GBDP, and a core-shell structure was formed, with pure $Nd_2Fe_{14}B$ in the core and a $(Pr,Nd)_2Fe_{14}B$ gradient layer at the surface with an anisotropy field slightly higher.

- The core-shell hard grains are decoupled by the non-magnetic Pr(Nd)-Fe phase allocated in the boundaries.

- The intergranular phase Pr(Nd)-Fe might delay the domain wall motion. The single domain $Nd_2Fe_{14}B$ nanograins with few defects

have also high nucleation field. Together these two mechanisms help to increase the coercivity of the samples.

Chapter 4:

- The substitution of Ce by Sm in the system $Ce_{1-x}Sm_xFe_{10}Co_2Ti$ improves the anisotropy field, from 2.6 T up to 8.7 T, and the Curie temperature, from 382 ºC up to 489 ºC, with a step when the concentration of Sm in the alloy is greater than 25%

- A parallel evolution is found in the hyperfine field of the Fe 8*j* site, probably due to the redistribution of Co atoms in the structure.

- The optimally heat treated melt-spun ribbons of $SmFe_{10}Co_2Ti$ reach a coercivity of 0.44 T. The coercivity of these samples is a promising value for the development of medium-grade permanent magnets.

- Nitrogenation of bulk $Nd_{0.5}Y_{0.5}Fe_{11}Ti$ greatly improves its intrinsic magnetic properties. The anisotropy was increased from 1.75 T to over 5 T and the Curie temperature from 270 ºC up to 390 ºC.

- Nitrogenation of melt-spun ribbons of $Nd_{0.5}Y_{0.5}Fe_{11}Ti$ improves the coercivity from 0.055 T up to 0.1 T. These nitrogenated ribbons, however, present a big amount of α-Fe, which is unfavourable to the coercivity.

- The system $Zr_{1-x}Ce_xFe_{10}Si_2$ increase the anisotropy field when Zr was substituted by Ce, from 2.0 T up to 2.5 T for x = 0.6.

- This improvement of the anisotropy is correlated with the increase of the cell volume and the tetragonal distortion (*a/c*) of the lattice.

- Mössbauer spectroscopy reveals a displacement of Fe atoms from the 8*i* to the 8*j* site in the 1:12 structure, reaching a saturation at x = 0.6, which explain the instability of the 1:12 phase and the formation of 2:17 phase for higher Ce concentration.

- These alloys present a giant magnetostriction of about 1500 ppm at room temperature.

- $Zr_{0.4}Nd_{0.6}Fe_{10}Si_2$ was successfully nitrogenated for the first time under a N_2 pressure of 20 bar at 550 ºC for 24 hours.

- A sample with 63% of the nitride phase presented an enhancement of the anisotropy field from 2.8 T up to 5.3 T, while the Curie temperature increased from 295 ºC up to 380 ºC.

- In the partially nitride sample, it is possible that some grains were fully nitrogenated while others were not nitrogenated at all. This can be due to a superficial anomaly of some of these grains.

- These samples show no signs of degradation below 550 ºC, which opens a door to the development of sintered magnets based on nitrogenated 1:12 alloys by means of alternative sintering processes as the spark plasma sintering.

Chapter 5:

- The attempt to find a RE-free alloy with uniaxial anisotropy in the Fe-Co-Ta system has been unsuccessful.

- No new ferromagnetic phase was found in the system and the known C14 Laves phase is unsuitable for its use in permanent magnets applications.

6.2 Open perspectives

Some of the materials shown in this work have good enough properties to be candidates as permanent magnets, but the main issue to overcome in the near future is the process to make a dense magnet out of them:

- The Nd-lean Nd-Fe-B alloys infiltrated with a eutectic alloy showed very good properties compared with the actual commercial magnets, but in order to compete with them, it is needed to make a sintered anisotropic magnet. The main problem in this process is the lack of a low melting alloy (which in common Nd-Fe-B magnets is present) that helps on the orientation of the grains during the sintering process.
  In a more elemental approach, two main questions remain to be answered; the effect of the Nd excess in the infiltration process, and the role of the $(Pr,Nd)_2Fe_{14}B$ layer at the grain surface
- The Sm-based 1:12 alloy presents the same problem as mentioned before when a sintered magnet is wanted. In order to get an anisotropic magnet, a molten phase is needed during the process. This topic is already being studied at the University of Delaware by partners of the NOVAMAG project.

- In the case of Nd-base 1:12 alloys, they need to be nitrogenated to get good properties, but these nitride phases are not stable at high temperatures, making them unviable for sintered magnets. They are, however, a good promise for bonded magnets, once a good coercivity is reached.
- In the special case of Si-stabilised nitride alloys, some experiments using SPS has already been done within the group, obtaining promising results, but on samples which coercivity was not optimised. In order to get a better understanding of this newly nitride alloys an in-situ neutron diffraction experiment has been done, with the results yet to be analysed. This experiment can give an insight of the nature of the nitrogenation process and the degradation process at high temperature in order to tune the parameters of the nitrogenation process and to know the limits that can be reached during the processing of these alloys to get a permanent magnet.

Apedix A. List of publications

List of publications arisen from this work:

- D. Salazar, A. Martín-Cid, R. Madugundo, J.M. Barandiaran, G.C. Hadjipanayis, "Coercivity enhancement in heavy rare earth-free NdFeB magnets by grain boundary diffusion process", *Appl. Phys. Lett,* 113 (15) 152402 DOI: 10.1063/1.5043389.

- D. Salazar, A. Martín-Cid, J.S. Garitaonandia, T.C. Hansen, J.M. Barandiaran, G.C. Hadjipanayis, "Role of Ce substitution in the magneto-crystalline anisotropy of tetragonal $ZrFe_{10}Si_2$", *J. Alloys Compd*. 766, 291-296 (2018) DOI: 10.1016/j.jallcom.2018.06.225

- A. Martín-Cid, D. Salazar, A.M. Schönhöbel, J.S. Garitaonandia, J.M. Barandiaran, G.C. Hadjipanayis, "Magnetic properties and phase stability of tetragonal $Ce_{1-x}Sm_xFe_9Co_2Ti_1$ 1:12 phase for permanent magnets", *J. Alloys Compd*. 749, 640-644 (2018) DOI: 10.1016/j.jallcom.2018.03.325

- D. Salazar, A. Martín-Cid, R. Madugundo, J.S. Garitaonandia, J.M. Barandiaran, G.C. Hadjipanayis, "Effect of Nb and Cu on the crystallization behaviour of understoichiometric Nd-Fe-B alloys", *J. Phys. D: Appl. Phys*. 50, 015305 (2017) DOI: 10.1088/1361-6463/50/1/015305.

- A. Martín-Cid, A. Gabay, D. Salazar, J.M. Barandiaran, G.C. Hadjipanayis, "Tetraonal Ce-based Ce-Sm(Fe, Co, Ti)$_{12}$ alloys for permanent magnets", *Phys. Status Solidi C* 13(10-12), 962-964 (2016) DOI: 10.1002/pssc.201600102

- A. Gabay, A. Martín-Cid, J.M. Barandiaran, D. Salazar, G.C. Hadjipanayis, "Low-cost $Ce_{1-x}Sm_x(Fe,Co,Ti)_{12}$ alloys for permanent magnets," *AIP Advances* 6, 056015 (2016) DOI: 10.1063/1.4944066